Real-time Observations of Quasicrystal Formation

by

Insung Han

A dissertation submitted in partial fulfillment
of the requirements for the degree of
Doctor of Philosophy
(Materials Science and Engineering)
in the University of Michigan
2020

Doctoral Committee:

Assistant Professor Ashwin J. Shahani, Chair
Professor Sharon C. Glotzer
Professor Emeritus John W. Halloran
Professor Emmanuelle Marquis

Insung Han

insungh@umich.edu

ORCID iD: 0000-0002-9831-8505

Acknowledgements

I am very thankful to my PhD advisor, Prof. Ashwin J. Shahani, for his consistent guidance, patience and support since I joined the Shahani Research Group as a graduate student in 2017. Prior to joining the group, I only had little background knowledge about quasicrystals, synchrotron-based characterization and computational techniques, so it took me quite a lot of time to get started and learn everything from scratch. Without his advice and encouragement over the past years, I would not have learned and grown so much as a student, a scientist, and a colleague.

I would like to thank Prof. John W. Halloran, Prof. Sharon C. Glotzer, and Prof. Emmanuelle Marquis for their valuable service on my doctoral committee. The discussions and feedback during my preliminary exam and data meeting guided me to think more deeply about the fundamental backgrounds, experimental techniques and my research results. Consequently, I could broaden my perspective and have more confidence when I completed each step of the requirements toward the PhD degree.

I appreciate the fun times and trips spent together with my fellow colleagues, Dr. Nancy Senabulya, Dr. Ning Lu, Dr. Hadi Parsamehr, Dr. Saman Moniri, Caleb Reese, Jiwoong Kang, Geordie Lindemann, Paul Chao, Yeqing Wang, Matt Higgins, Zhucong Xi, Mushfequr Rahman, Ron Keinan and Megan Wiltse, and their very helpful feedback on my research. They have always been supportive with their brilliant ideas.

Special thanks to the dedicated staffs at the Michigan Center for Materials Characterization, especially to Dr. Haiping Sun and Dr. Kai Sun for teaching me how to operate the instruments following safety protocols and sharing their time to discuss research projects. In addition, I would like to thank to the staffs at the Lurie Nanofabrication Facility, especially David Sebastian and Katharine Beach for helping me find optimized sample condition, which was extremely sensitive.

I am very grateful to my research collaborators, Dr. Xianghui Xiao (Brookhaven National Laboratory), Dr. Joseph T. Mckeown (Lawrence Livermore National Laboratory), Dr. Matt J. Kramer and Dr. Cai-Zhuang Wang (Ames Laboratory), Dr. Vincent de Andrade (Argonne national Laboratory) and Kelly Wang (University of Michigan) for their experimental assistance and devoted help. Without their support, I could not have such valuable research opportunities.

I am also grateful that the University of Michigan has provided resources and facilities and my funding source, the U.S. Department of Energy (contract no. DE-SC0019118) has supported my PhD study.

Last but certainly not least, I would like to express my gratitude to my parents, Youngha Han and Hyunju Kong, brother, Hee-sung Han and girlfriend, Ain Hwang for their support throughout the years.

Table of Contents

List of Tables

List of Figures

Abstract

Since the discovery of quasicrystals, there have been continued efforts to explain their growth mechanisms given that their unique structures violate the rules of conventional crystallography. Despite decades of research on the topic, the growth mechanisms of quasicrystals remain one of the fundamental puzzles in the field of crystal growth. To elucidate the growth of quasicrystals, many theories have been proposed. However, there have been very few experimental investigations with which to test the various theories, and quasicrystal growth often accompanies complicated interactions and unexpected growth pathways beyond the scope of these theories. Therefore, to corroborate these theories, it is essential to utilize the benefits of advanced *in situ* characterization techniques, such as X-ray tomography (XRT) and dynamic transmission electron microscopy (DTEM). The results obtained through these advanced techniques provide direct evidence to support the theories, with high spatial and temporal resolutions. Especially, such *in situ* approaches allow extracting the information regarding the growth kinetics, growth shapes, and growth interactions which cannot be retrieved from *ex situ* characterization techniques.

In the first and primary part of this thesis, the growth of a single quasicrystal will be discussed. We demonstrate how growth and dissolution pathways of a decagonal quasicrystal are different from each other with respect to the underlying mechanism (interfacial attachment in the former case and bulk transport in the latter). In addition, we compare the growth kinetics of a decagonal quasicrystal with its crystalline approximant, which shares a similar structural motif. Furthermore, we investigate the kinetic and equilibrium shapes of icosahedral quasicrystals. These observations are only possible when we incorporate 4D (*i.e.*, 3D space + time) approaches.

The second part of this thesis concerns the growth interactions between multiple quasicrystals. We examine the interfacial phenomena when quasicrystals impinge on each other using 4D XRT and describe the preconditions required for forming a single quasicrystal from multiple quasicrystalline nuclei or ‘seeds’ with the aid of molecular dynamics (MD) simulations. From the XRT results, we can directly observe the formation of a single quasicrystal based on the gradual disappearance of grain boundary grooves. In typical solidification experiments, it is often

unavoidable to produce polycrystalline materials, which often deteriorates materials' properties. Therefore, our joint experiment-computational discovery paves the way toward fabrication of single, large-scale quasicrystals to solve engineering problems.

The last part of this thesis covers the solid-state phase transformation from approximant to quasicrystalline phases induced by a short-pulsed laser irradiation. To the best of our knowledge, the real-time investigation of quasicrystal growth far-from-equilibrium has not been reported in a time-resolved manner. Additionally, the solid-state dendritic growth is extremely rare in Nature and several preconditions have to be satisfied for this growth form to manifest. Interestingly, this study demonstrates how quasicrystals grow dendritically showing a huge deviation from their well-known polyhedral growth shapes and what contributes to this unique precipitation pathway. Through ab initio MD simulations, we identify common structural motifs that facilitate the phase transformation between the approximant and quasicrystalline phases.

Overall, the findings in this dissertation work are at the forefront of solidification science and have expanded our knowledge on the growth mechanisms of quasicrystals and their approximants using advanced characterization techniques and corresponding simulations.

Part I. Theoretical Background

Chapter 1. What Are Quasicrystals?

1.1. A short history of quasicrystals

The discovery of *quasicrystals* (QCs) by Shechtman *et al*. was a fascinating if somewhat controversial event in the field of crystallography due to their unique structures [1]. This is because QCs are characterized by their long-range translational order and unique rotational symmetries (*e.g*. five-, eight-, ten-, and twelve- fold) which cannot be found in ordinary crystals. In plane language, it was known that such unique rotational symmetries cannot be used to fill 2D plane or 3D space as depicted in **Fig. 1.1(a)**. However, diffraction patterns of QCs provide counter-examples, see **Fig. 1.1(b)**.

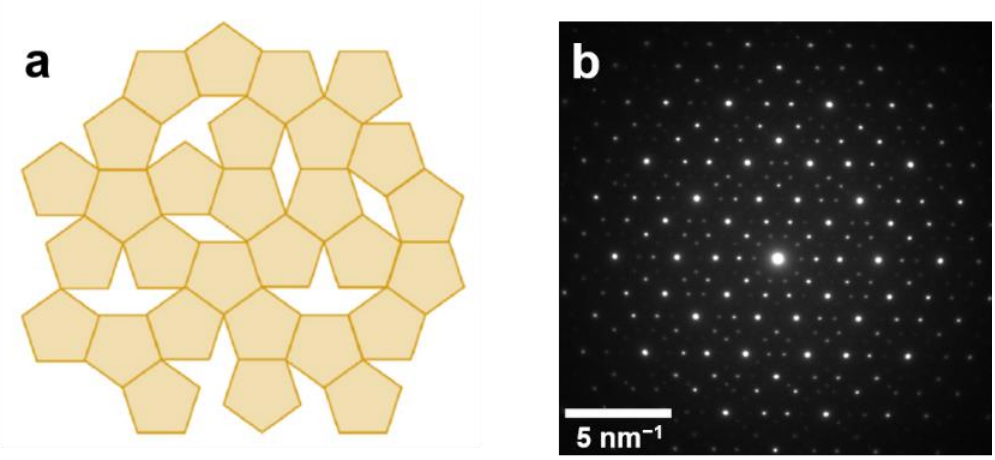

Fig. 1.1. (a) 2D space filling with pentagonal structural motifs. (b) Ten-fold diffraction pattern from an AlCoNi decagonal QC, along [00001] zone axis, reprinted from [2].

As such, the discovery of QCs led to a revision in the definition of a crystal by the International Union Crystallography (IUCr) to a material with discrete diffraction patterns regardless of its periodicity [3] and Shechtman was later awarded Nobel Prize in Chemistry in 2011 for his discovery.

The first QCs were found in Al – 14 at% Mn alloy upon rapid quenching. Shechtman reported the icosahedral point group symmetry ($m\bar{3}\bar{5}$) from this alloy and the specimen displayed clear twofold, threefold and fivefold diffraction patterns as the sample was rotated through the angle of this point group [1]. The discovery of QCs with icosahedral point group symmetry, so called icosahedral (i-) QCs was followed by the discovery of decagonal (d-) QCs where we can find both two-fold periodic and ten-fold aperiodic lattices simultaneously [4].

The unique structure and properties of QCs led more than 11,000 publications since their discovery and more than 200 articles have been reported annually in recent years [5]. However, in spite of a number of recent articles, there are still remaining open questions as Steurer mentioned in his seminal review paper [5], in the realm of the structure, stability and growth of QCs. Several of the open questions regarding the growth of QCs have been answered with the development of advanced *in situ* characterization techniques with high temporal and spatial resolutions.

1.2. Crystal structure and structural complexity of quasicrystals

Due to the absence of unit cells in QCs (lack of periodicity), we seek alternative ways to describe the complex crystal structure in QCs. For example, the Penrose tiling can be used to cover a plane in a nonperiodic fashion using two different types of rhombi [6-8] (which can be thought of as unit cells). The tiles are arranged in a way that they obey certain 'matching rules'. The Penrose tiles can be expanded to fill a 3D space, as well. In that case, the 3D space can be filled with rhombohedrons instead of rhombi [7]. If the quasicrystalline structure follows the Penrose tiling, it is considered that the quasicrystalline structures are *ideal* QCs, or devoid of defects. However, in practice, it is more widely acceptable that quasicrystalline structures are explained by randomly assembled tiles, incorporating microscopic disorder and Bragg peak scattering [9]. Since the ideal tiling model cannot explain the disordered structure, we alternately use a *random* tiling model [10, 11] in which a class of configurations corresponding to tiling of the plane with rhombi is assumed to occur with the same probability to explain this structure. In addition, quasicrystalline structures can be explained by the cluster-based model in which overlapping *clusters* or quasi-unit-cells fill the 2D plane or 3D space [12, 13]. All of these theories describe the basic building blocks of aperiodic structures. **Fig. 1.2** demonstrates the examples of the ideal tiling, random tiling and cluster-based models.

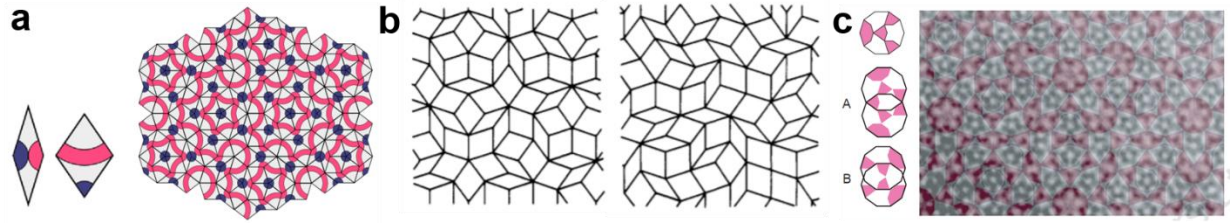

Fig. 1.2. Examples of (a) Ideal tiling, (b) random tiling, and (c) cluster-based models. Reprinted from [10, 13, 14], respectively.

Due to the aperiodicity in at least one dimension in QCs, it is not possible to describe the structure using three-integer Miller indices to label observable Bragg reflections. In order to assign integer indices on the diffraction patterns of QCs, we need five (for d-QC) or six (for i-QC) linearly independent vectors [15]. The necessary 'n' vectors span an n-dimensional reciprocal space and therefore there needs to be an n-dimensional direct space where a structure can be built. In this high-dimensional space, we can describe a QC as a periodic crystal [15]. In addition, the n-dimensional space can be separated into orthogonal subspaces, $V_{\parallel}$ and $V_{\perp}$, where $V_{\parallel}$ is the parallel or physical three-dimensional space and corresponds to atomic positions in real space. $V_{\perp}$ corresponds to the (n-3)-dimensional perpendicular space and can be represented by an extended polyhedral distribution function called an occupation domain or atomic surface [15]. This means that the kind of long range order of a quasiperiodic structure is not only coded in the n-dimensional Bravais lattice type but also in the position, size and shape of the atomic surfaces [5]. The actual quasicrystalline structure in the physical space can be obtained by an appropriate projection of high-dimensional space onto low-dimensional space (see **Fig. 1.3**). Hence, it is reasonable to state that there exists a unit cell in the n-dimensional structure. The contents of such n-dimensional unit cell consist of hyperatoms in analogy to the atoms in a normal unit cell. This allows us to describe the quasicrystalline structure with a finite set of parameters.

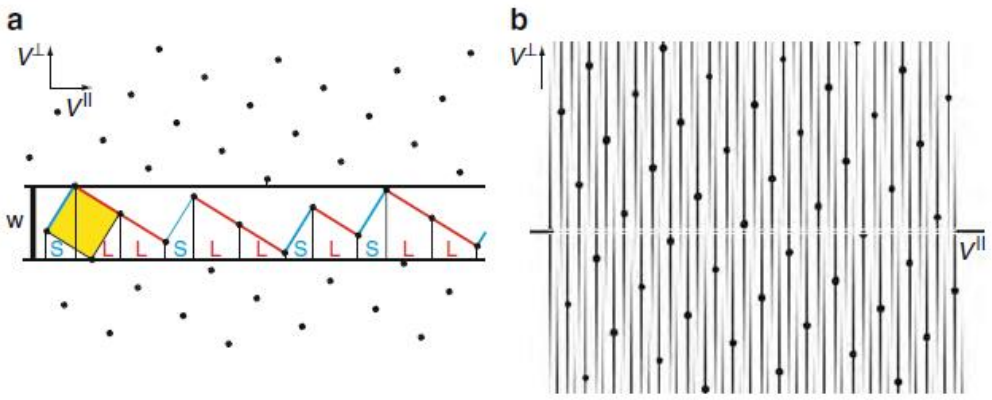

Fig. 1.3. 2D embedding of the 1D Fibonacci sequence. (a) A strip with an irrational slope of $1/\tau$ (τ: Golden ratio, $\frac{1+\sqrt{5}}{2}$) with height *w* acts as window for projection (*cf*. rational slope is achieved from periodic crystals). The lattice points inside the strip are projected onto its parallel space (*x*-axis, $V_{||}$). The resulting pattern in 1D is the Fibonacci sequence. (b) In reciprocal space, each lattice point is convoluted with the Fourier transform. The Fourier transform of the 1D Fibonacci sequence is obtained by 'cutting' the Fourier transform of the strip (white double lines). Reprinted from [16].

1.3. Phason mode, Phason flip, and Phason strain in quasicrystals

Phasons are a class of defect that is unique to QCs. It would be useful to define here the various terminologies frequently used in the QC community, such as phason mode, phason flip and phason strain. Even though these terminologies are sometimes used interchangeably, it is important to have an accurate understanding of their distinctions. For example, de Boissieu [17] suggested that we should keep the term 'phason' for phason modes only. The explanation of each term is below.

Phason modes in QCs can be introduced within the hydrodynamic theory, which is a phenomenological theory based on symmetry breaking arguments and group theory analysis [18]. Hydrodynamic equations predict a set of low frequency modes that are either propagating with a dispersion relation $w \sim cq$ (w: frequency, c: velocity, q: wavevector) or diffusive relation, which is described as $w \sim -iDq^2$, where D is a diffusion constant.

In QCs with n-dimensional quasiperiodicity, there are $2n$ broken symmetry hydrodynamic variables, which are twice as many as in conventional periodic crystals. The first n variables correspond with phonon modes, which represents elementary vibrational motion in which a lattice of atoms uniformly oscillates at a single frequency. On the other hand, the additional n variables represent phason modes which are associated with the relative displacement of incommensurate

density waves [19]. According to Landau theory [19, 20], uniform translation of phonon and phason variables do not change the free energy of the system. The phason modes are applicable to all aperiodic crystals and show diffusion-like, collective and non-propagative excitation. The dispersion relation of a phason mode with wavevector q consists of a purely imaginary part and decays exponentially, thus different with the propagative long wavelength, acoustic phonon modes [18].

Phason flip refers to the local rearrangement process at the atomic scale (or tile scale) between split positions in QCs [17] by the elementary process of a phason mode [21]. A phason flip transforms one local configuration into a similar, energetically nearly identical one by overcoming an energy barrier between them. Phason flips can be either single-particle jumps or correlated ring-like multi-particle move [21], see **Fig. 1.4**. The presence of phason flips plays a key role in explaining enhanced atomic diffusion [22], dislocation motion [19], and structural phase transitions in QCs [23]. The long-wavelength phason mode can be possibly related to a local phason flip. In other words, such a long wavelength phason fluctuation could consist of a combination of local phason flips; however, this has yet to be demonstrated [24].

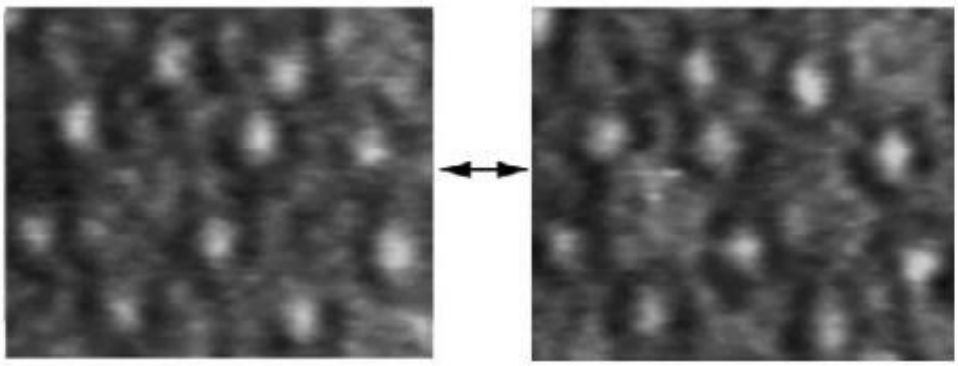

Fig. 1.4. Example of the structure change by a phason flip observed in the HRTEM image at 1123 K in AlCuCo d-QC. Reprinted from [25].

To characterize the presence of phason flips in QCs, various advanced characterization studies have been performed. For example, with the aid of in situ transmission electron microscopy, we can directly observe thermally activated phason flips, such as that shown in **Fig. 1.4** [25-27]. In addition to such direct imaging methods, researchers have reported phason

flips *via* indirect means, such as neutron scattering [28, 29], Mössbauer spectroscopy [30] and nuclear magnetic resonance [31, 32] techniques.

Phason strain refers to a perpendicular shear strain of the periodic space [17]. When phason strain is relaxed, phason flips take place and there is a change in the atomic surface. From the point of view of the tiling picture, phason strain is evidenced by violations of the matching rules, or local deviations from the ground state structure [33]. In particular, the presence of incommensurate length scales in QCs gives rise to a possible phason strain field which contributes to diffraction peak shift and broadening in a manner qualitatively different from strain in periodic crystals [34]. Also, the phason strain reveals systematic deviation from the diffraction pattern of ideal QCs [34]. A more qualitative way to study the presence of phason strain is to use the relation between scattering vector $G_{\parallel}$, ($G_{\parallel} = 4\pi \sin \theta/\lambda$) *vs.* half width half maximum (HWHM) and phason momentum ($G_{\perp}$,) *vs.* HWHM [35]. This approach is feasible because the peak broadening in X-ray diffraction is well accounted for by simple lattice strain with no measurable dependence of the peak widths on phason momentum. Specifically, the presence of phason strain can be estimated when HWHM and $G_{\perp}$ are linearly proportional and HWHM and $G_{\parallel}$ are not correlated [35].

1.4. Quasicrystals and their approximant phases

The term "approximant" was first introduced by Elser and Henley [36] to explain the crystalline structure generated from a hyper-cubic crystal using a rational ratio q/p (q and p are consecutive numbers in the Fibonacci sequence) to substitute for the irrational golden mean, $\tau = (1 + \sqrt{5})/2$. Described succinctly, *approximant phases* of QCs are defined as structures which share a similar structural motif or subunits of QCs and in many cases they exhibit definite orientation relationships with the QCs [37]. Additionally, the approximant phase should have periodically stacked atomic layers and specifically for the case of d-QCs, the periodicity length in the approximant phase should be almost identical to that of the d-QCs or at similar to that of the sublattice of d-QCs [38, 39].

In general, these approximants phases have a complex, large unit cell and play an important role in understanding quasicrystalline structures. As implied above, the approximant phases can be found in both 2D decagonal quasicrystals and 3D icosahedral quasicrystals and can include a number of compositional variants. For instance, binary aluminum-cobalt phases, which are

approximant phases of decagonal Al-Co-Ni QCs, form a large number of equilibrium phases with large unit cells (*e.g.* Al_5Co_2, Al_9Co_2, $Al_{13}Co_4$, *etc*.) [40, 41]. The approximant phases of d-QCs commonly contain pseudo-decagonal structural motifs (*e.g.* pentagonal bipyramid, see **Fig. 1.5**) and represent similar diffraction patterns with QCs. Similarly, θ-$Al_{13}Cr_2$ phase [42] is known as a Mackay-type approximant phase of 3D icosahedral QC [43, 44]. We can find a stacking or overlapping of Mackay-type clusters, and thus a local pseudo-fivefold symmetry, in the Al-rich region of θ-$Al_{13}Cr_2$ alloy and other Al-TM alloys [43-45]. The phase transformation between QCs and approximant phases is often observed during slow cooling [46] and sometimes we can obtain both phases simultaneously depending on quenching rate [44, 47]. Fast quenching rates generally induce the formation of metastable Al-TM QCs, whereas slow quenching rates lead the formation of thermodynamically stable approximant phases [47].

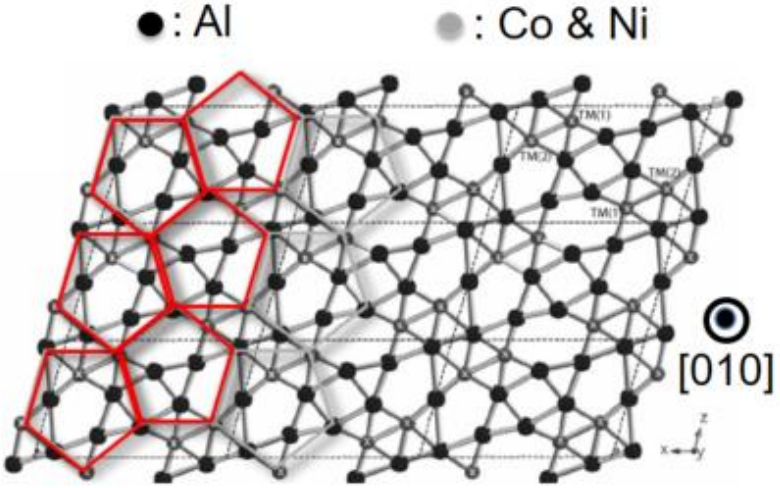

Fig. 1.5. One layer of the approximant X-phase ($Al_9(Co,Ni)_4$) of decagonal QCs with highlighted pentagonal structure motifs. Reprinted from [48].

Chapter 2. Nucleation and Growth Mechanisms

2.1. Nucleation

2.1.1. Classical nucleation theory

The transformation of one phase into another requires rearrangement of the atoms, which includes a short-range atomic rearrangement to form a nucleus of a new crystal structure. In discontinuous transformations [49], atoms of the parent phase migrate and grow into the new phase. However, a thermodynamic driving force is needed to induce the nucleation. This is why tiny clusters in liquid alloys above the melting point are metastable and do not evolve into stable nuclei. In this section, the driving force of nucleation will be discussed based on classical nucleation theory.

Nucleation begins at some degree of *undercooling* ΔT, defined as the temperature difference between the equilibrium (liquidus) temperature of an alloy and its actual temperature. Below the liquidus, the free energy change associated with the nucleation process will have the following three contributions: (i) a volume free energy reduction of $V\Delta G_v$ by the creation of a volume V of a stable solid phase and (ii) a free energy increase of $A\gamma$ by the creation of a surface area A assuming the liquid-solid interface energy γ is isotropic [49, 50]. Summing terms gives the total free energy change as

$$\Delta G = V\Delta G_v + A\gamma = -\frac{4\pi r^3}{3}\Delta G_v + \gamma 4\pi r^2 \quad (2.1)$$

where we have ignored the strain energy and assumed a spherical solid phase of radius r. For a unary (single component system), one can show that ΔG_v is represented as

$$\Delta G_v = \Delta s_f \Delta T \quad (2.2)$$

where Δs_f is the entropy of fusion per unit volume. Generalizations to **Eq. 2.2** for alloys are presented in **Sec. 2.2.5**. If we assume that ΔT is simply the undercooling of the liquid of the pure metal solidifying with a planar interface, then

$$\Delta T = T_e - T^* \tag{2.3}$$

where T_e is the equilibrium liquidus temperature and T^* is the interface temperature. The value of γ is always positive whereas ΔG_v depends upon ΔT and is negative if ΔT is positive. This behavior leads to the occurrence of a maximum in the value of ΔG when the melt is undercooled, *i.e.*, when ΔT is positive. The maximum can be regarded as being the activation energy which has to be overcome in order to form a crystal nucleus which will continue to grow. The criterion for the maximum is that

$$\frac{d\Delta G}{dr} = 0 \tag{2.4}$$

and can be regarded as being a condition for unstable equilibrium between a liquid and a solid with curvature such that the driving force for solidification is equal to that for melting [49]. Differentiation of **Eq 2.1** yields

$$r^0 = \frac{2\gamma}{\Delta G_v} \tag{2.5}$$

$$\Delta G^* = \frac{16\pi\gamma^3}{3\Delta G_v^2} \tag{2.6}$$

where r^0 and ΔG^* represent the critical radius for further crystal growth and the activation energy for nucleation. Before solidification can begin, at least one cluster which is as large as r^0 must be formed. For small r, the surface energy penalty exceeds the volumetric liberation of energy, whereas the volumetric contribution dominates at larger radii [51]. The time which elapses before this occurs will be different at different locations in the melt. In this case, fluctuations spontaneously create a small crystalline volume in an otherwise homogeneous melt (no solid phase). This is referred to as *homogeneous nucleation* because the occurrence of nucleation transforms an initially homogeneous system (consisting only of atoms in the liquid state) into a heterogeneous system (crystal + liquid). However, when the melt contains solid particles, or is in contact with a crystalline crucible or oxide layer (such as our work), nucleation may be facilitated, even with a few K of undercooling. This is known as *heterogeneous nucleation* [49, 51].

According to the negentropic model by Spaepen [52] and Thompson [53], γ is given as

$$\gamma(T) = \alpha \Delta S_f T (N_L V_m^2)^{-1/3} \quad (2.7)$$

where α, ΔS_f, N_L, and V_m denotes dimensionless interfacial energy, entropy of fusion, Avogadro number and molar volume, respectively. More specifically, the parameter α depends on the structure of the solid phase. It is found that i-QCs have comparatively low α value, approximately 0.3, compared with other FCC and BCC structures [52, 54-56] which have values in the range of 0.7-0.85. This can be attributed to the prevalence of icosahedral short range order in undercooled metallic melts, *i.e.*, the structural similarity between solid and liquid phases, which leads to a low interfacial energy by way of **Eq. 2.7** and also a low nucleation barrier by way of **Eq. 2.6**. The short-range order in metallic melts of pure metals [57, 58] and quasicrystal forming alloys [59] has been demonstrated by neutron scattering studies.

2.1.2. Nucleation in quasicrystal-forming systems

The above arguments suggest that it is possible to nucleate QCs with relative ease. The quasicrystalline nuclei could, in turn, provide a template for crystal growth for other periodic crystals and contribute to the formation of nanotwinned structures [60, 61], see **Fig. 2.1**. According to Kurtuldu *et al*. [61], a trace amount of Cr in Al-Zn-Cr alloy contributes to forming Al-Cr icosahedral solid clusters prior to solidification. The Al-Cr icosahedral clusters act as inoculants, nucleating heterogeneously the α-Al FCC phase with the same orientation of icosahedral cluster. During slow solidification with cooling rate of 0.2 K/s, the metastable icosahedral phase dissolves through a peritectic transformation and we can eventually observe twin structures of α-Al FCC phase. This study indicates that trace elements favoring the formation of an icosahedral phase could bring a significant contribution to nucleation of periodic metals [61]. In a similar sense, Hornfeck *et al*. [60] reported a decagonally shaped solidification front in an NiZr alloy with high undercooling (at most 300 K) with electrostatic levitation. Tenfold microtwinning in NiZr is correlated to a decagonal nucleus underneath. From these studies, we can understand the importance of pre-existing nuclei in supercooled liquids on final microstructure under near- [61] and far-from [60] equilibrium conditions.

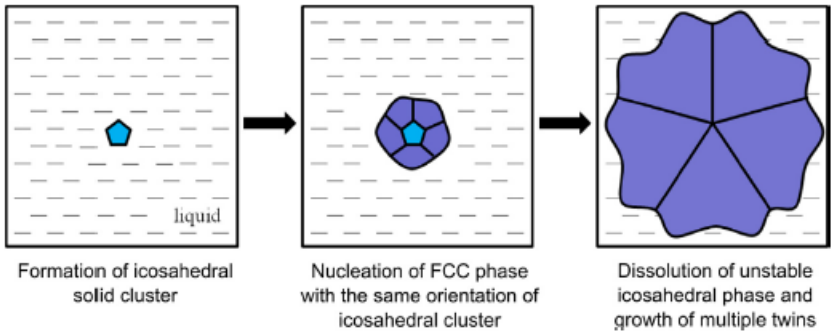

Fig. 2.1. Quasicrystal-enhanced nucleation. Schematic drawings of the possible mechanism leading to the formation of Al multiple twinned grains from an existing icosahedral phase in undercooled liquid. Reprinted from [61].

2.2. Growth

2.2.1. Diffusion limited growth

The attachment of atoms on a 'rough' interface between a stable nucleus and a supersaturated matrix (either a melt or a solid) is relatively easy, because there is no energy barrier to overcome to become a part of growing crystal. In other words, the growth rate of the particle is governed by the solute flux in the matrix phase, and not by the kinetics of atom attachment (discussed below). The diffusion current of solute across a surface *S* of a non-facetted particle should be equal to the rate of mass change of the crystal (the so-called Robin condition) [62]. Hence,

$$\oint_S I \cdot dA = 4\pi l^2 D\nabla C = 4\pi r^2 \frac{dr}{dt} \tag{2.8}$$

where I $(= -D\nabla C)$ is the diffusion current per unit area, dA is the differential area, D is the diffusion coefficient, ∇C is the solute concentration gradient in the liquid, l is the mean distance of an imaginary surface from the grain center, r is the radius of the crystal, and dr/dt is the growth rate. The growth rate (**Eq. 2.9**) can be found from **Eq. 2.8**,

$$\frac{dr}{dt} = D\,(c_a - c_r)/r \tag{2.9}$$

where c_a and c_r denote the solute concentration at a long distance away from the interface and at the interface, respectively. **Eq. 2.9** predicts that the growth rate should decay as crystals grow larger, assuming a constant supply of solute. That said, the supersaturation $(c_a - c_r)$ can vary due

to overlapping of diffusion fields, especially when the diffusion length (roughly, $\sqrt{Dt}$) is larger than the particle radius. It is also worth noting that in this simplified treatment, a crystal is always spherical, whereas in reality constitutional effects lead to instabilities and diverse growth forms (see **Sec. 2.2.3-2.2.4** and also Appendix A for a discussion on rapid solidification).

2.2.2. Interface limited growth

Here we consider the opposite extreme, that is, atoms have to overcome an energy barrier at the interface to become a part of the growing crystal. Assuming that the α crystal grows from the β matrix as shown in **Fig. 2.2**,

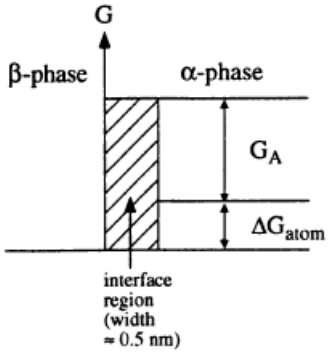

Fig. 2.2. Schematic drawing of the energetic situation at a smooth interface where an energy barrier impeding atom attachment exists. Reprinted from [63].

The thermally activated fluxes from the α crystal to the β matrix and *vice versa* are

$$I_{\alpha\rightarrow\beta} = n_a^{\alpha} \upsilon \exp\left(-\frac{G_A}{k_B T}\right) \tag{2.10}$$

$$I_{\beta\rightarrow\alpha} = n_a^{\beta} \upsilon \exp\left(-\frac{G_A + \Delta G_{atom}}{k_B T}\right) \tag{2.11}$$

where n_a is the number of atoms per area at the interface, υ is the number of jumps an atom performs per second, and G_A is the energy barrier. From the **Eqs (2.10 & 2.11)**, different fluxes arise due to the increase of the energy barrier by ΔG_{atom}. Assuming that (i) $n_a^{\alpha} = n_a^{\beta} = n_a$, (ii) the local interface velocity is a function of net flux, and (iii) $\Delta G_{atom}/k_B T \ll 1$, then

$$v = \Omega\left(I_{\alpha\rightarrow\beta} - I_{\beta\rightarrow\alpha}\right) = \Omega n_a \upsilon \exp\left(-\frac{G_A}{k_B T}\right)\frac{\Delta G_{atom}}{k_B T} \tag{2.12}$$

or $$v = \frac{dR}{dt} = M\Delta G_{atom} \quad (2.13)$$

where M denotes the interface mobility

$$M = \Omega n_a \upsilon \exp\left(-\frac{G_A}{k_B T}\right)\frac{1}{k_B T} \quad (2.14)$$

Eq. 2.13 suggests that the interface velocity is constant, provided the supersaturation is fixed (*cf.* **Eq. 2.9**). These equations also demonstrate that the growth rate depends not on diffusivities but rather on the energy of transferring an atom from the matrix to the crystal.

Eq 2.12 is often presented in a more general form [63, 64], as

$$v = \beta_s (x_a^{\beta} - x_a^{\beta,equil})^n \quad (2.15)$$

where β_s is a constant of proportionality known as the kinetic coefficient in a supersaturated matrix. For example, interface kinetics of first order ($n = 1$), otherwise known as the "normal" growth mechanism, signifies growth of interfaces decorated with terraces, ledges, and kinks, while interface kinetics of second order ($n = 2$) indicates spiral growth along a screw dislocation (**Fig. 2.3**). Descriptions of other growth laws ($n = 3$ and so on) can be found in [65].

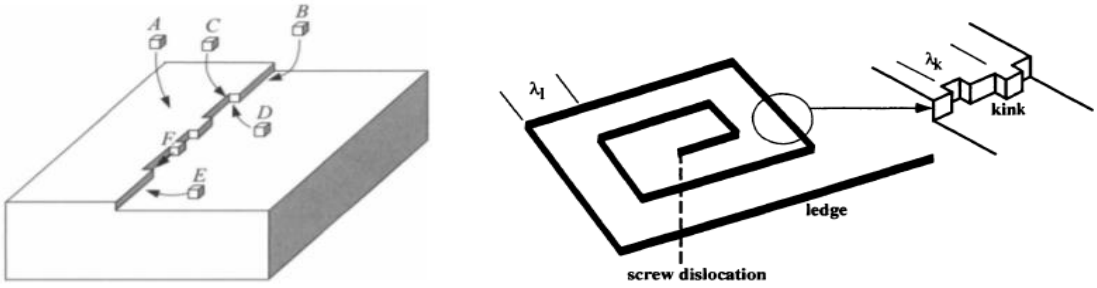

Fig. 2.3. Schematic drawing of terrace-ledge-kink model of interface, corresponding to n = 1, and a screw dislocation, corresponding to n = 2. The integer exponent determines the surface of growing phase. Reprinted from [63, 66].

2.2.3. Dendritic growth

Dendrites are tree-like structures which grow far from the limit of stability of the planar front (described below). The dendritic tips adopt an orientation that is in an opposite direction of heat flux and/or consistent with the crystallographically-preferred growth axes [67]. Dendritic

growth begins when small perturbations along the interface are amplified [49]. If the heat flow is opposite to the growth direction, *columnar dendrites* form. Such columnar growth can be only found in the solidification of alloys, not pure metals, owing to the partitioning of solute (discussed below). When the temperature gradient due to the heat flux is greater than the temperature gradient of liquidus temperature at the solid-liquid interface, the perturbations at the interface would be damped. However, when the temperature gradient of liquidus temperature is greater than the actual temperature gradient, the tip of a perturbation experiences an increase of undercooling (so-called *constitutional undercooling*) and thus a planar interface becomes unstable [49]. Numerically the constitutional undercooling at the interface is developed if

$$G < mG_c \tag{2.16}$$

where G is the temperature gradient, G_c is the concentration gradient and m is the slope of liquidus curve (such that mG_c is the liquidus temperature gradient). **Fig. 2.4** shows that the temperature gradients at the interface and expected final structures for a stable (left) and unstable front (right).

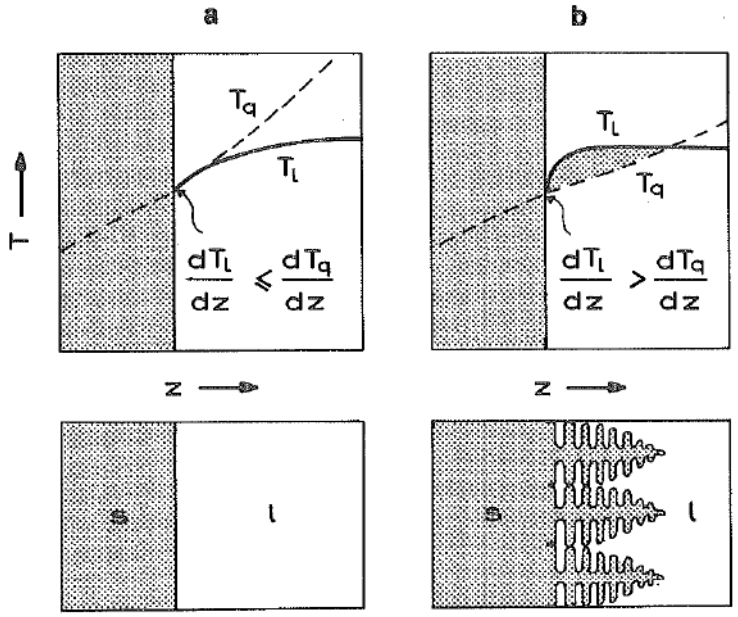

Fig. 2.4. Conditions for constitutional undercooling at the solid- liquid interface and resultant structures. Reprinted from [49].

On the other hand, when the heat flows from the crystal into the melt, equiaxed dendrites can grow freely in both pure metals and alloys. The dendrites grow radially until the growth is limited by *soft collisions* (overlapping diffusion fields) and *hard collisions* (impingements). For

pure metals, the latent heat creates negative temperature gradient in the liquid surrounding the crystals and perturbations on the growing crystals make this gradient steeper and allow the tip to reject more heat. Consequently, this leads faster local growth rate at the tip and a morphological instability. A similar phenomenon is observed in alloys, where both solute and heat are rejected during the solidification process. To fully understand the equiaxed dendritic growth of alloys, one needs to solve the problem of coupled heat and mass transport at the interface [68]. The resultant morphologies, concentration and temperature profiles of pure metal and alloy dendrites are represented in **Fig. 2.5**.

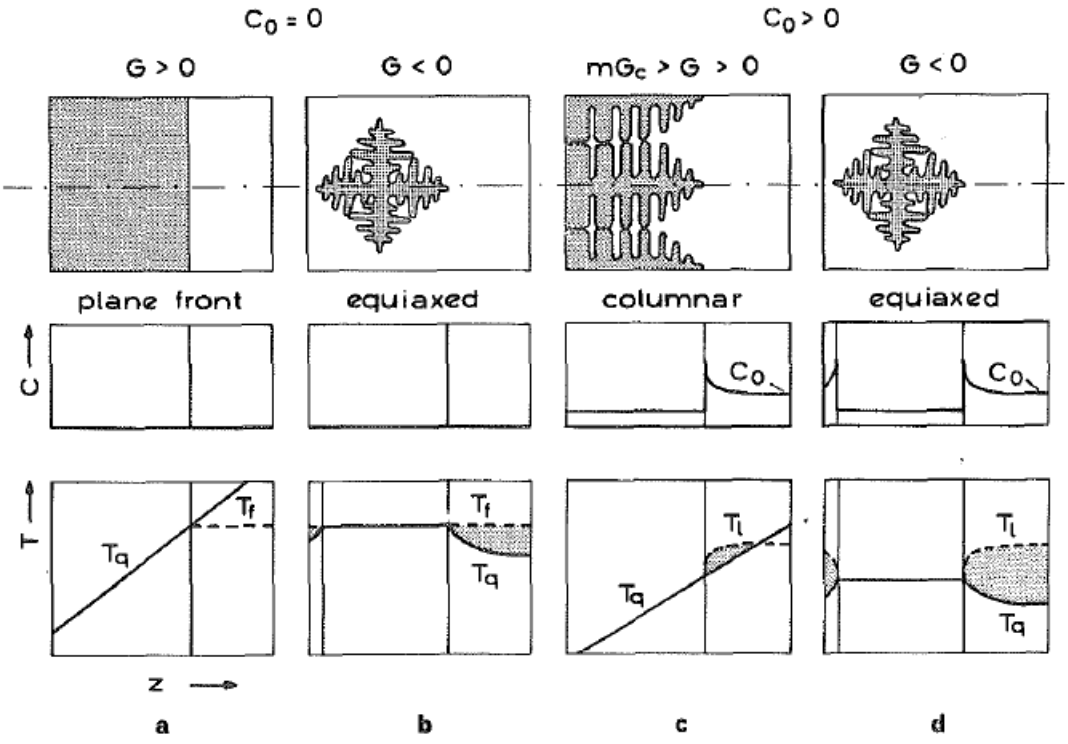

Fig. 2.5. Resultant morphologies (first low), concentration (second low) and temperature profiles (third low) of dendrites in pure metals (a,b) and alloys (c,d). Reprinted from [49].

2.2.4. Mullins-Sekerka instability

The above analysis takes into account the destabilizing influence of solute but does not account for the stabilizing influence of surface tension or capillarity. Mullins and Sekerka considered both of these effects, mathematically predicting the stability of the shape of an interphase boundary during a phase transformation where mass transport or heat flux regulate the

growth process [69]. This model contains the following approximations: (i) elastic stain energy and anisotropy of interface properties are neglected; (ii) thermal and diffusion fields are assumed to follow Laplace's equation; and (iii) local equilibrium holds at each element of interface [69]. The instability calculation determines whether perturbations at the interface will grow or decay.

First, we can introduce an infinitesimal distortion of shape caused by a single spherical harmonic Y_{lm}, with the amplitude δ. The equation of the distorted sphere can be represented as **Eq. 2.17** and the spherical coordinates depend on time.

$$r = \rho(\theta, \varphi) = R + \delta Y_{lm}(\theta, \varphi) \tag{2.17}$$

The first derivative of Eq. (2.17) is

$$v = \frac{dR}{dt} + \frac{d\delta}{dt} Y_{lm}$$

$$= \frac{D}{C - c_s}\left\{\frac{c_\infty - c_R}{R} + \left[(l-1)\frac{c_\infty - c_0}{R^2} - \frac{c_0 \Gamma_D}{R^3}[l(l+1)^2 - 4]\right]\delta Y_{lm}\right\} \tag{2.18}$$

where C is the concentration in the precipitate, c_s is the equilibrium concentration at a general curved interface, c_∞ is the concentration in the supersaturated solution, c_R is the concentration on the undistorted sphere, l is the order of spherical harmonic, and Γ_D is a capillary constant ($\Gamma_D = \frac{\gamma \Omega}{RT}$, where γ and Ω represent the interfacial free energy and molar volume of the precipitate. From **Eq. 2.18**, we obtain the rate of growth of the amplitude of the spherical harmonic ($\dot{\delta} = d\delta/dt$) as

$$\dot{\delta}_l = \frac{D(l-1)}{(C - c_R)R}\left[G - \frac{c_0 \Gamma_D}{R^2}(l+1)(l+2)\right]\delta_l \tag{2.19}$$

where $G = (c_\infty - c_R)/R$ is the normal concentration gradient at the surface of the undistorted sphere, and the subscript l indicates the corresponding harmonic. **Eq. 2.19** can be modified as **Eq. 2.17** to represent the relationship between a harmonic of l^{th} order and the radius of the sphere that determines whether perturbations will grow or decay. The interface is unstable when the radius of the sphere is greater than the critical radius $R_c(l)$, at given supersaturation,

$$R_c(l) = 2\Gamma_D[(1/2)(l+1)(l+2) + 1]/[(c_\infty - c_0)/c_0] \tag{2.20}$$

Here, supersaturation is given by the quantity $[(c_\infty - c_0)/c_0]$. This Mullins-Serkeka instabilitiy is applicable in both solidification [69] and solid-state transformations [69-71]. **Fig. 2.6** plots **Eq. 2.20** for a range of supersaturations. It can be seen that growing crystals are generally stable

when the crystal radii are small due to the influence of surface tension, suppressing perturbation. Also, we can see the decreasing effective supersaturation (trajectories 2 & 3 in **Fig 2.6**) which can be attributed to the overlapping diffusion fields between different crystals. Stated altogether, the growth of dendrites is an interplay between surface tension and bulk diffusion.

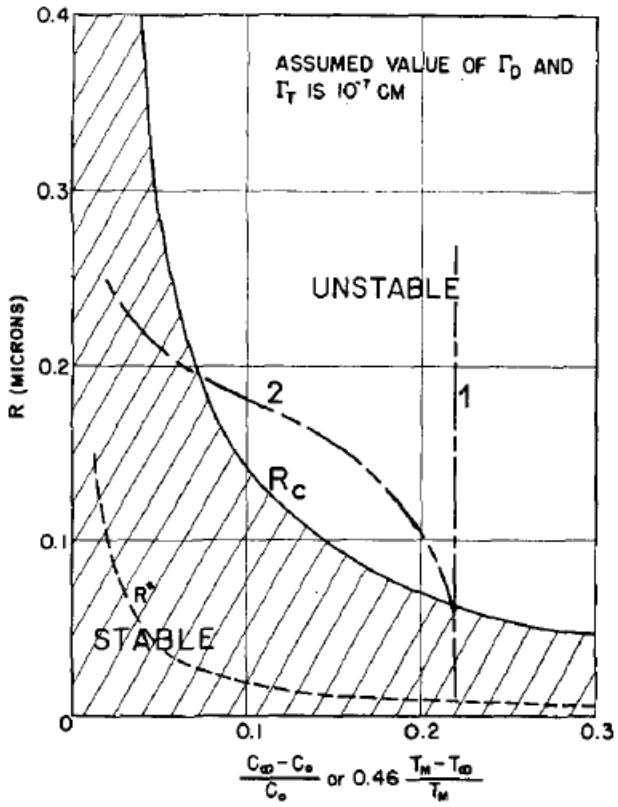

Fig. 2.6. R_c delineates stability of a sphere as a function of its radius (y axis) and supersaturation (x axis). Below this solid line, the interface is stable (hatched region); above, it is unstable. Dashed curve gives critical nucleation radius $R^*$and broken curves (1-2) represent possible growth pathways of particles. Reprinted from [69].

2.2.5. Growth of metastable phases

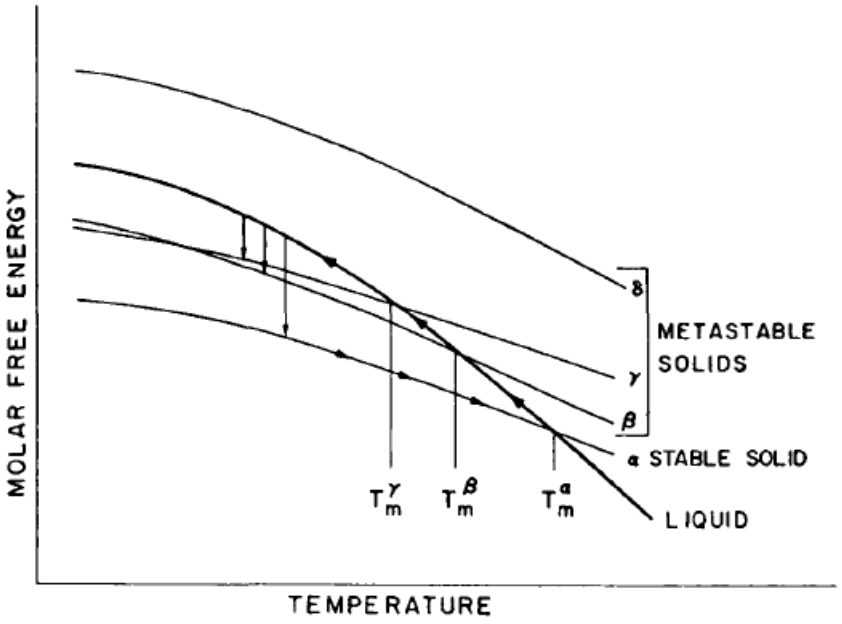

Fig 2.7. Free energy *vs*. temperature curves illustrating possible free energy change during heating and solidification cycles for a single component system. Reprinted from [72].

Fig. 2.7 shows examples of free energy curves of several phases as a function of temperature for a single component system. If we heat up α phase above its liquidus temperature and let it cool down (see arrows), we may able to observe the nucleation of the α phase. However, if nucleation of the α phase is suppressed upon cooling, possibly due to a high interfacial energy and hence, nucleation barrier (see **Sec. 2.2.2**), the liquid becomes undercooled. Under such conditions, we may expect to see the nucleation of either the metastable β or γ phase. That is, as the liquid is progressively cooled, other reactions are possible, although thermodynamics by itself is not able to predict which reaction will be preferred. The prediction of phase transformations should be based on other factors, such as the interfacial free energy and the presence of heterogeneous nucleation catalysts [72, 73].

As we work with alloys, it is of interest to predict metastable phase transformations in multi-component systems. Two- or three- component alloys have additional compositional degrees of freedom and thus the possibility of equilibria between multiple phases over a range of temperatures [72]. The formation of a given phase at a given temperature is thermodynamically valid if it satisfies the Baker-Cahn '*tangent-to-curve*' construction [72]. For example, in a binary alloy, when equilibrium may be disrupted by an additional amount of solute, we can predict the

formation of a metastable phase by first drawing a tangent line at the given composition. For example, in **Fig. 2.8**, initially the β phase is in equilibrium with the α phase. The equilibrium condition is confirmed by the existence of a common tangent at the composition $C_{\alpha}(eq)$. However, as the composition becomes B-rich due to a saturation of B atoms, the metastable γ phase has the larger driving force compared to the β phase and thus we would predict the formation of the metastable γ phase (considering again only driving forces and not interfacial energies, strain energies, etc.). According to Baker and Cahn [72], a phase transformation is thermodynamically possible so long as the line connecting the tangent to free energy curve points vertically downward. The length of this line (e.g., $\Delta G_{\alpha \rightarrow \beta}$) gives us the free energy change (per mole reacted) for reactions in a closed system that transfer small amounts of components of composition C_{β} from α phase at composition C_0 to the β phase at composition C_{β} [72]. Using the same approach, we can predict the phase decomposition of a metastable phase to a stable phase. In **Fig. 2.9**, we draw a tangent line from the free energy curve of the metastable γ phase at the initial composition of C_0, and thus we would predict the formation of α phase rather than the β phase since there is a driving force for phase transformation.

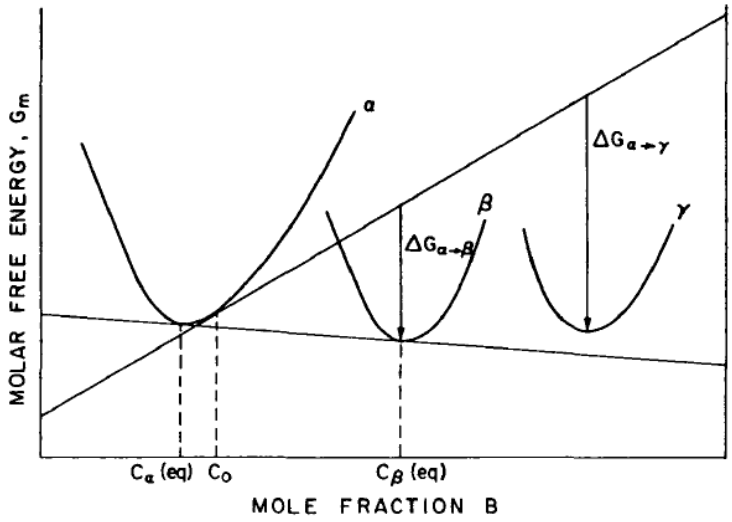

Fig. 2.8. Gibbs free energy curves of thermodynamically stable α and β phases at C_{α}(eq). A slight supersaturation changes the slope of the tangent line and provide a driving force to form the metastable γ phase. Reprinted from [72].

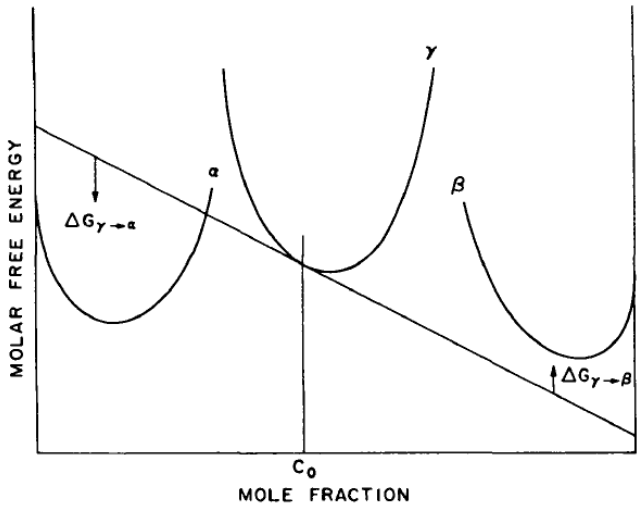

Fig. 2.9. Decomposition of thermodynamically metastable γ phase to thermodynamically stable α phase. Reprinted from [72].

2.2.6. Growth of complex intermetallics, including quasicrystals

While their structures have been extensively studied, the growth kinetics of the complex intermetallic phases from a liquid phase have been much less explored. To this end, Steurer has identified in his topical reviews [5, 74] the problem of QC growth as one of the still open questions facing the crystallographic community, as of 2018. He asks, `How does the 1000th atom find its site in a giant unit cell with thousands of atoms?' One physically plausible explanation is that the growth (of both QCs and their approximants) occurs not by the attachments of single atoms but rather energetically favourable clusters of atoms that pre-exist in the liquid phase (see also **Sec. 1.2**). If this cluster-based argument is to be believed, then one might suppose that the rate of crystal growth slows with increasing cluster size. This is because large clusters require more time to rotate towards the correct orientation [75-77] in this way, clusters should overcome a configurational entropy-type barrier in order to incorporate into the solid phase.

Refs. [78-80] have analyzed the growth of icosahedral QCs *via in situ* X-ray radiography (*i.e.*, projection videomicroscopy). They studied the interfacial velocity of the facets and edges in the icosahedral QC during directional solidification. Based on the results obtained, the researchers suggested that QC growth is in some ways analogous to the kinetics of ledge growth in semiconductors [81-83]. While one can extract some qualitative information from the 2D images, X-ray radiography is prohibitive since most growth models, such as those listed above, make

predictions based upon a 3D structure. In a similar sense, Nagao *et al*. have studied grain growth in a decagonal QC specimen using *in situ* high resolution transmission electron microscopy (HRTEM) [27]. This study, too, is limited to the ten-fold {00001} plane, *i.e*., there is no mention of the interfacial dynamics along the period direction. *In situ* and 3D experimental studies on the growth and dissolution of QCs from a parent liquid phase have not been demonstrated yet, to the best of our knowledge.

Part II. Experimental Methods

Chapter 3. Experimental Methods

In this chapter, we will discuss the two main imaging techniques used to investigate real-time formation of QCs. Among many characterization techniques (**Fig. 3.1**), we chose two *in situ* techniques, (i) synchrotron-based X-ray absorption tomography and (ii) dynamic transmission electron microscopy. The former provides a sufficient temporal resolution to observe the microstructure evolution under near-equilibrium (*e.g.* slow cooling), while the latter is optimized to capture the QC growth dynamics far-from-equilibrium during rapid quenching. Utilizing the benefits of these two techniques, we can obtain a better understanding of transient growth behaviors of QCs, such as local growth velocity, facet orientation and interface instabilities; these insights can be used to compare the growth kinetics between thermodynamically stable and metastable QCs as well as their approximants.

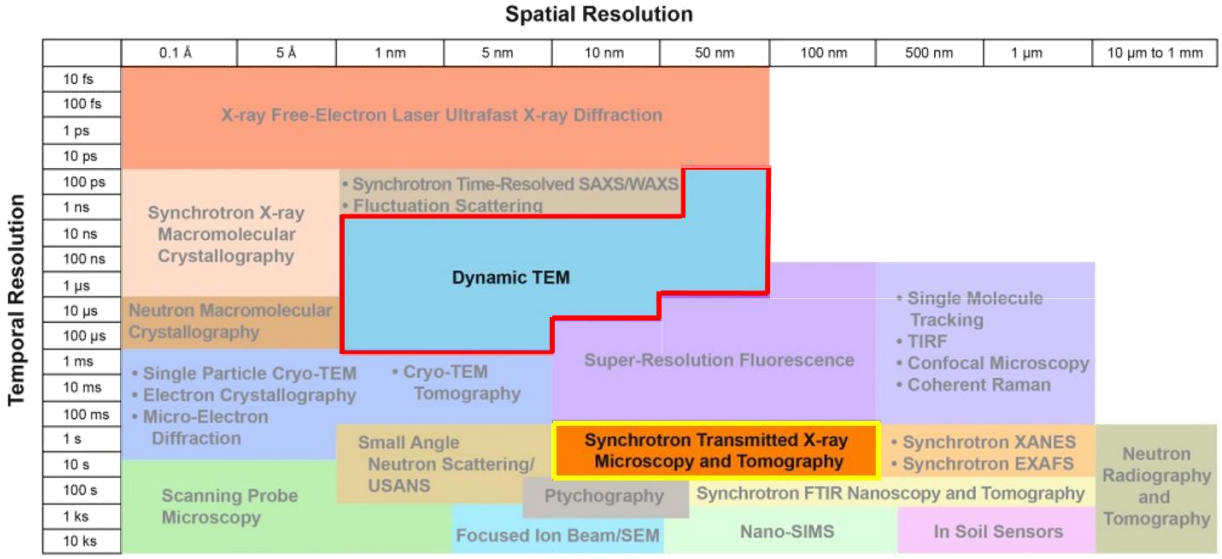

Fig. 3.1. Spatial and temporal resolutions of various characterization techniques. Reprinted from [84].

3.1. Synchrotron-based X-ray absorption tomography

3.1.1. Basic principles

X-ray tomography (XRT) is a nondestructive approach that enables us to investigate the evolution of 3D microstructure in real-time. In principle, the XRT is based on different attenuation of elements and phases inside the sample, for instance, a higher intensity is typically associated with low atomic number elements in the microstructure due to less attenuation of the incident beam [85]. The intensity of a transmitted X-ray also depends on other factors, including sample thickness and beam hardening. After X-rays penetrate the sample, the transmitted X-ray is absorbed by the scintillator, which emits the absorbed energy in the form of visible light. The light is detected by the CCD camera. To render 3D volume, we need to record on the CCD camera a consecutive set of X-ray projections spanning 180° of sample rotation. The experimental setups are illustrated in **Fig. 3.2** and more details regarding the sample preparation, experiment and data processing methods will be further explained in this chapter.

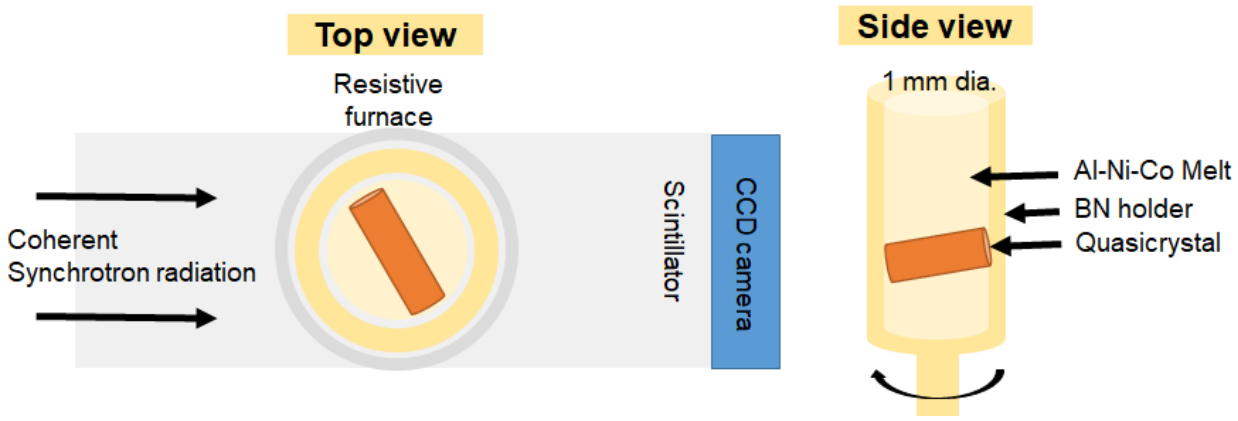

Fig. 3.2. Schematic drawings of experimental setups for X-ray microtomography experiment on QC solidification.

3.1.2. Sample preparation

For the X-ray microtomography experiment, high purity alloy samples (*e.g.*, $Al_{81}Co_{9.5}Ni_{9.5}$ (**Ch. 4** & **Ch. 5**), $Al_{79}Co_6Ni_{15}$ (**Ch. 7**), and $Al_{74}Pd_{20}Mn_6$ (**Ch.6**)) were prepared with the vacuum arc remelting (VAR) technique at the Materials Preparation Center (MPC) at Ames Laboratory in Ames, Iowa, USA. Past work [2, 86] has demonstrated that these systems will produce

thermodynamically-stable decagonal and icosahedral phases, respectively, within a narrow compositional window, see **Fig. 3.3**.

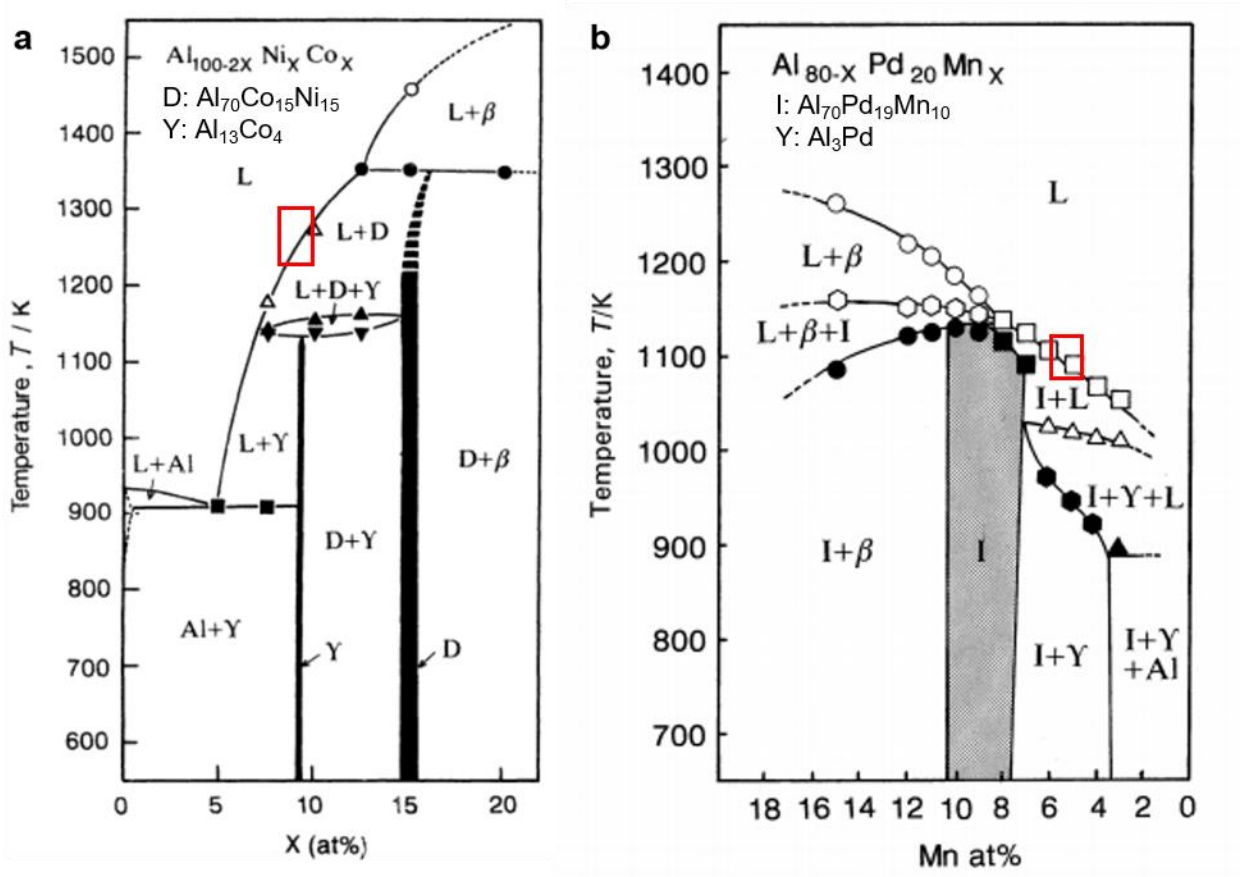

Fig. 3.3. Equilibrium phase diagrams of (a) a pseudo-binary $Al_{100-2x}Ni_xCo_x$ [46] and (b) $Al_{80-x}Pd_{20}Mn_x$ [87]. Note 'D' and 'I' represent d-QC and i-QC, respectively. The regions of interest for **Ch.4**, **Ch.5** and **Ch.6** are highlighted on the phase diagrams.

The cast alloy buttons were cut into a rod of 1 mm diameter by 5 mm height for the synchrotron experiment. The sample was placed in a boron nitride (BN) specimen holder with a 1.2 mm cylindrical hole (see **Fig. 3.2**). The BN specimen holder is X-ray transparent and stable at high temperature such that it does not influence the solidification experiments. The sample and holder were mounted on the Al_2O_3 rod and placed on the rotating stage with *in situ* resistance heater for the X-ray microtomography experiment. The X-ray microtomography experiment was performed at beamline 2-BM of the Advanced Photon Source (APS) at Argonne National Laboratory in Lemont, Illinois, USA.

3.1.3. Data collection and reconstruction

The projection images for microtomography experiment were collected at a rate of 50 Hz using a polychromatic 'pink' beam centered at 27 keV. The 'pink beam' is an alternative to monochromatic beams for dynamic studies (higher flux) where the X-ray beam is reflected from a grazing incidence mirror rather than a monochromator [88]. A PCO Edge 5.5 CMOS camera optically coupled with a 20 µm-thick LuAg:Ce scintillator was used for data collection. The field of view (FOV) measured 2560 by 800 pixels along the specimen x (horizontal) and z (vertical) directions, respectively, with a pixel size of $(0.65 \times 0.\ 65)\ \mu m^2$. One thousand projections were recorded for each 180° rotation of the sample with an exposure time of 14 ms, resulting in a temporal resolution of 20 s between successive 3D reconstructions. The *in situ* solidification experiment was conducted while projections were recorded continuously, or in other cases, discretely (*i.e.*, 'blocks' of 180° rotations were separated by a time interval). The size of a single 3D *tomogram* (or a set of projection images that span 180° of sample rotation) is approximately 4 GB.

The XRT data were reconstructed with TomoPy [89], a Python-based open-source framework for data processing and reconstruction. First, we normalized the X-ray projection images with white-field images after the dark-field image correction. Normalization helps to compensate differences in the sensitivities and responses of each detector pixel; however, normalization alone is not enough to remove 'ring' artefacts, which result from dead pixels in the detector and X-ray beam instabilities. For the removal of ring artefacts, we use a built-in combined Fourier-wavelet filter [90]. After normalization and ring artefact removal, the tomographic data were reconstructed via the Gridrec algorithm [91]. Gridrec is based on discrete Fourier transform; further details can be found in Gürsoy *et al*. [89]. In this way, a stack of 800 2D image slices along the specimen z direction (representing a 3D volume) was obtained for each time-step (with a temporal discretization of 20 s).

3.1.4. Segmentation of 2D reconstructed images and volume rendering

Image segmentation was conducted using the Image Processing Toolbox in MATLAB. We subtracted the image stack of the fully liquefied sample from all other image stacks in order to enhance the contrast between the solid and liquid phases and eliminate any remaining artefacts.

The subtracted images were then segmented into solid and liquid phases using a common threshold value for the reconstructed intensity and combined to reveal the 3D microstructures. For the subsequent analysis, the solid-liquid interfaces were meshed, or represented by a sequence of triangles and vertices [92]. To remove any staircasing artifacts, the triangular mesh (see **Fig. 3.4(a)**) was smoothed *via* mean curvature flow [93]. The following calculations make use of the mesh face and vertex positions. We denote the vertices of an arbitrary triangle face *i* as v_1^i, v_2^i, and v_3^i.

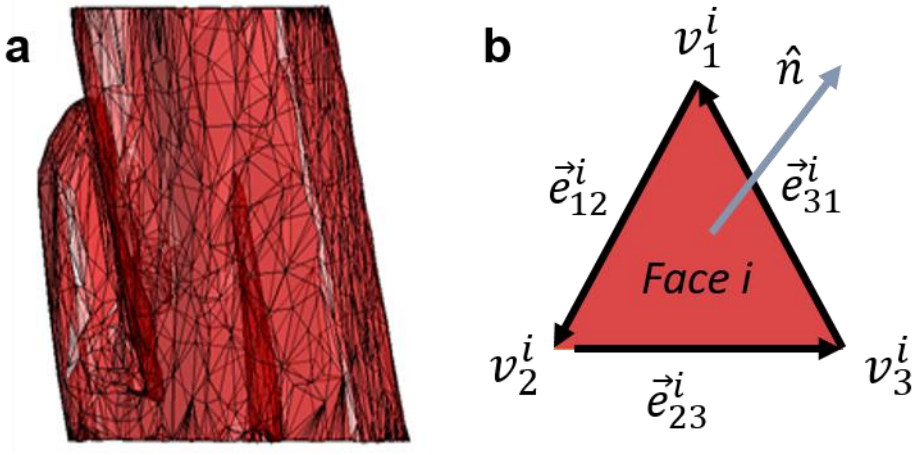

Fig. 3.4. (a) 3D microstructure consists of triangular mesh. (b) A triangle face that belongs to the triangular mesh. $v, \vec{e}$, and $\hat{n}$ denote the vertex, edge, and normal vector of the triangle face *i*.

3.1.5. Microstructure analysis

We track the growth dynamics by computing the local interfacial orientation and local velocity of each triangle in the mesh (**Fig. 3.4(b)**). Given that the edges of i^{th} triangle face are defined as $\vec{e}_{12}^{\,i} = v_2^i - v_1^i$, $\vec{e}_{23}^{\,i} = v_2^i - v_3^i$ and $\vec{e}_{31}^{\,i} = v_3^i - v_1^i$, and that the vertex order is consistent for all faces, the unit normal vector $\hat{n}$ of the i^{th} triangle in the mesh can be found as

$$\hat{n} = (\vec{e}_{12}^{\,i} \times \vec{e}_{23}^{\,i}) \,/\, |\vec{e}_{12}^{\,i} \times \vec{e}_{23}^{\,i}| \qquad (3.1)$$

Following thermodynamic convention, all normal vectors point from the crystal to the liquid. Geometrically, the denominator in **Eq. 3.1** represent the area of i^{th} triangle face in the mesh, $A^i = |\vec{e}_{12}^{\,i} \times \vec{e}_{23}^{\,i}|$. After computing all normal vectors, we next plotted the *interface normal distribution* (IND) [94], which indicates the degree of directionality in the microstructure. In practice, we

depicted the IND as a stereographic projection of the interface normal vectors, $\hat{n}$ adorning the mesh. Note the IND is computed in the specimen frame of reference and *not* the crystallographic frame. That is, the IND conveys the extrinsic directionality of the faceted solid-liquid interfaces while electron diffraction patterns convey the intrinsic lattice symmetry.

In addition to the local interfacial orientation, the local interfacial velocities were calculated according to a nearest neighbor (NN) algorithm [95]. In short, we found the NN vertex in the mesh corresponding to time-step $t + \Delta t$, for each face centroid at time t. The distance between these two points divided by the time interval Δt gives the face velocity of each triangle face A^i. In a similar manner, the collective facet velocity can be found as

$$V^{facet} = \sum_{i \in facet} A^i V^i \; / \; \sum_{i \in facet} A^i \qquad (3.2)$$

Thus, the facet velocity is a weighted average of the local triangle face velocities. The summations in **Eq. 3.2** are carried out only for those triangle faces that belong to the facet.

3.1.6. Compositional analysis

The intensity I of a transmitted X-ray beam depends on many factors, including sample thickness, chemical composition, and beam hardening, as mentioned previously. For example, $I \propto e^{-d}$ according to the Beer-Lambert law, where d is sample thickness. Thus, to ensure that differences in intensity reflect only the differences in chemical composition — such that the composition mapping strategy described later in **Sec. 4.3** can be applied — the following precautions were taken: First, we selected the same thicknesses of liquid and QC (approx. 1110 μm, in regions 1 and 2 respectively (**Fig. 4.4**)). In addition, we subtracted a projection image of the fully liquefied sample above the liquidus temperature from every projection that followed. This was done to mitigate the effect of beam hardening, which arises when a polychromatic X-ray beam becomes "harder" due to the ease of absorption of soft X-rays.

After these processing steps, we measured the average transmitted X-ray intensities from the QC and liquid at equilibrium. Correspondingly, the composition of the QC and liquid at equilibrium are read from the phase diagram [46]. With these two reference points, we can simply solve the simultaneous equations that give the contributions of Al and heavy elements (Ni and Co) to X-ray intensity. In this manner, the composition of the liquid phase, in terms of Al and the heavy

elements, is attained for all time-steps. Additionally, to determine the total alloy composition $< x_{Co,Ni}^{total} > (t)$ in the FOV, as plotted in **Fig. 4.1(c)**, we need to know the QC volume fraction, f^{QC}, which is simply found from the segmented 3D reconstructions as the sum of all voxels belonging to the QC phase divided by the sum of all voxels contained in the rod sample within the FOV. Then, $< x_{Co,Ni}^{total} > (t)$ can be found from the lever rule as

$$< x_{Co,Ni}^{total} > (t) = f^{QC} x_{Co,Ni}^{QC} + (1 - f^{QC}) < x_{Co,Ni}^{L} > (t) \qquad (3.3)$$

where the term $(1 - f^{QC})$ represents the volume fraction of the liquid phase.

3.2. Dynamic transmission electron microscopy

3.2.1. Basic principle

Dynamic transmission electron microscopy (DTEM) at Lawrence Livermore National Laboratory, Livermore, California, USA, enables the imaging of transient behaviors (*e.g.* phase transformation, structural deformation and chemical reaction) with an unparalleled combination of temporal (~10 ns) and spatial resolutions (~10 nm) [96]. In the DTEM experiment, a short pulse of laser melts the alloy sample and the transient phase transformation dynamics are recorded by the electron probe after a user-set delay time in the DTEM either in the single shot [96] or nine-shot "movie-mode" [97] configuration. In this manner, we can capture the transient growth behaviors of crystals (and QCs) with relative ease.

The technology uses two synchronized laser beams with ns pulses, one of which will be used to optically trigger the melting of a solid film of QC composition, and second of which will generate the electrons bunches (10^9 electrons) for subsequent TEM imaging. That is, each pulse captures an image of the sample at a specific time. A fast-switching electron deflector located below the sample directs each image to a separate patch of a large high-resolution CCD camera, thereby overcoming the slow refresh rate of camera [96]. This is a key feature that allows DTEM to achieve a frame rate which is six ordered of magnitudes faster than conventional video-rate TEM. **Fig. 3.5** demonstrates a schematic of DTEM movie mode.

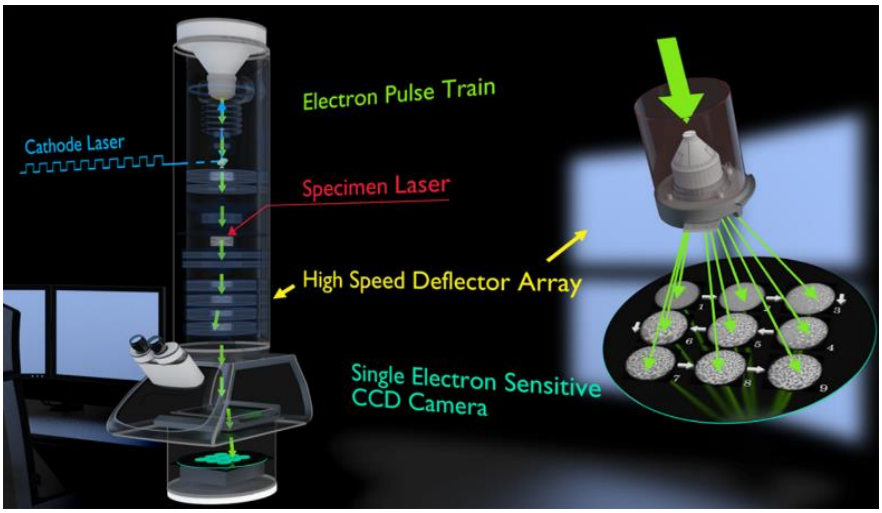

Fig. 3.5. Schematic of movie-mode DTEM. Reprinted from [97].

3.2.2. Sample preparation

Metastable quasicrystals are most often encountered under high driving forces in Al-TM alloys (TM: Cr, Mn, among others) [1, 13– 16]. Thus, we prepare thin Al-Cr films sample at the Lurie Nanofabrication Facility, Ann Arbor, Michigan, USA. The PVD 75 has the capability to co- or tri- deposited Al and other transition metals (V, Mn, Cr, Fe, Co, Ni, *etc*), which demonstrated the formation of metastable i-QCs upon rapid quenching [98]. SiN TEM grids and targets were mounted into the PVD 75 and the chamber was evacuated below 10^{-7} Torr to prevent contamination. We co-deposited Al and Cr with thickness of 150 nm, which is ideally adjusted for the DTEM experiment in terms of sample stability at elevated temperature [99] and image quality. The sample composition was calibrated to $Al_{90}Cr_{10}$.

3.2.3. X-ray absorption spectroscopy measurement

The local structure of the film before laser irradiation was confirmed by X-ray absorption spectroscopy (XAS) at the National Synchrotron Radiation Research Center (NSRRC), Hsinchu, Taiwan. Samples for XAS were prepared in the same manner as for DTEM and annealed for 5 minutes at 340 °C, but with a thickness of 450 nm to satisfy the detection limit of XAS. The X-ray energy was set above the Cr K-edge (5989 eV). The IFEFFIT software package [100] was used to

analyze the raw XAS spectra in *k*-space and R-space. The data was fit to simulated $Al_{13}Cr_2$ structure [42].

3.2.4. DTEM experiment

The $Al_{90}Cr_{10}$ samples were placed on an *in situ* heating stage in the DTEM and annealed at 340 °C for five minutes to induce a phase transformation to the $Al_{13}Cr_2$ phase (C2/m) (plus Al) [101]. Then, the samples were irradiated by a short pulsed laser with 1064 nm wavelength for 15 ns of exposure time. The laser intensity was tuned to 15.2 μJ to prevent film dewetting and rupture. The microstructural evolution within the thermally affected zone was recorded in DTEM using 50 ns electron probe pulses after a preset delay time, approximately 180 μs. Two different time lapses, 2.5 μs and 5 μs (between the nine consecutive frames) were used to investigate the growth behaviors of QCs. To calculate the growth velocity of QCs, we computed equivalent radii based on the number of pixels that belongs to the growing QC phase after image segmentation using the Image processing toolbox in MATLAB. The data processing steps are somewhat similar to that described in **Sec. 3.1.4**, albeit for a set of 2D images.

3.2.5. Finite element analysis (FEA) simulation

FEA was conducted by using COMSOL Multiphysics software (version 5.4, COMSOL, Inc) to determine the temperature evolution of our sample. The laser flux, ϕ_{laser}, is determined as

$$\phi_{laser} = P_{laser}\frac{\sqrt{sin\theta}}{2\pi\sigma}\exp\left(-\frac{x^2+y^2sin^2\theta}{2\sigma^2}\right) \quad (3.4)$$

where P_{laser} is the power of the laser; θ is the angle of incidence; σ is the radius of the laser; and x and y represent the coordinates on the sample surface along the minor and major axes, respectively. All parameters used to determine ϕ_{laser} are shown in **Table 1**.

Property	Value	Unit
Power of the laser (P_{laser})	1012	W
Angle of incidence θ	45	°
Radius of the laser σ	67.5	μm
Thermal conductivity Al	235	W $m^{-1}K^{-1}$
Thermal conductivity Cr	94	W $m^{-1}K^{-1}$
Thermal conductivity Si_3N_4	30	W $m^{-1}K^{-1}$
Thermal conductivity quasicrystals	2	W $m^{-1}K^{-1}$
Density Al	2700	kg m^{-3}
Density Cr	7190	kg m^{-3}
Density $Al_{13}Cr_2$	3290	kg m^{-3}
Heat capacity Al	904	J $kg^{-1}K^{-1}$
Heat capacity Cr	448	J $kg^{-1}K^{-1}$
Heat capacity $Al_{13}Cr_2$	700	J $kg^{-1}K^{-1}$
Reflectivity at wavelength of 1064 nm Al	0.94	
Reflectivity at wavelength of 1064 nm Cr	0.63	
Emissivity of Si_3N_4	0.7	

Table 3.1. Physical properties used in FEA simulation.

The focus of laser is defined as the origin of the x and y coordinates. We assumed that there is no surface heat conduction and convection, and only accounted for heat radiation at the surface and heat conduction within the solid. These assumptions are similar to those used by Zweiacker *et al.* [102]. The reflectivity of the $Al_{90}Cr_{10}$ film was determined by linear interpolation between the reflectivities of the constituent elements, Al and Cr [103].

Part III. Results and Discussion

Part III presents the results of our experimental efforts, the corresponding analyses, and discussion of the results. The chapters in Part III include the growth of a single d-QC and its approximant phase; the growth and equilibrium shapes of a single i-QC; physical interaction between multiple QCs; and solid-state i-QC growth under far-from equilibrium conditions. This chapter contains the works published over the course of my doctoral research, which are listed in Refs. [2, 86, 104] with Refs. [105] in revision and [106] to be submitted.

Chapter 4. Growth and Dissolution of a Decagonal Quasicrystal

The growth mechanism of QCs remains one of the fundamental puzzles in the field of crystal growth since there have been very few experimental investigations to test various hypotheses (*e.g.*, ideal tiling model, random tiling model, and cluster-based model) explaining the QC growth (see also **Sec 1.2**). In particular, direct evidence of the *in situ* and 3D growth of a QC from a parent liquid is lacking. To fill-in-the-gaps in our understanding of the solidification and dissolution pathways of QCs, we performed synchrotron-based XRT experiments on a decagonal QC-forming system, as will be described below.

4.1. Experimental background

Our foundational work started with probing the growth and dissolution pathways of a single d-QC using synchrotron-based 4D (3D + time) XRT. We focus our investigation on the Al-Co-Ni system, which contains a thermodynamically stable decagonal QC phase, as mentioned previously [107, 108]. The synchrotron experiment was performed on an alloy of nominal composition Al-9.55at%Ni-9.55at%Co. As a first step and to prove the existence of decagonal QCs in this system, we recorded the electron diffraction pattern of the stable decagonal QC phase at ambient temperature from the cast alloy (**Fig. 4.1(a)**). As expected, the diffraction pattern shows sharp reflections and the requisite 10-fold symmetry. Our XRT results were obtained by continuously cooling an Al-9.55at%Ni-9.55at%Co rod sample from above its liquidus temperature into the two-phase, decagonal QC plus liquid regime. A partial section of the pseudo-binary $Al_{100-2x}Ni_xCo_x$ phase diagram is shown in **Fig. 4.1(b)**. The solidification of the Al-15at%Ni-15at%Co QC is non-congruent, with rejection of Al as growth proceeds. This means that we were able to achieve absorption contrast between the QC and the surrounding liquid phase owing to differences in X-ray absorption [85].

Although the entire rod sample is cooled during the tomography experiment (see **Sec. 3.1.2**), only a portion of the sample is imaged (hereafter referred to as the tomographic field-of-view or FOV). This FOV behaves as an open system, exchanging solute (Al, Ni, and Co) with other parts of the rod sample. We observed **Fig. 4.1(c)** that the alloy composition within the FOV becomes Al-rich as time proceeds. Here, the time-dependent alloy composition was found quantitatively by mapping the variation of intensity in the X-ray projection images to composition (see **Sec. 4.3**). The "pile up" of the Al constituent is likely due to a combination of gravity-induced segregation and Al rejection from regions outside the FOV. Eventually, the accumulation of Al in the liquid initiates dissolution of the QC. A similar phenomenon of dendrite arm remelting was reported by several investigators [109]. Thus, we were able to measure *both* growth and melting in the same experiment, as the sample enters and exits the two-phase decagonal QC plus liquid regime in **Fig. 4.1(c)**, respectively.

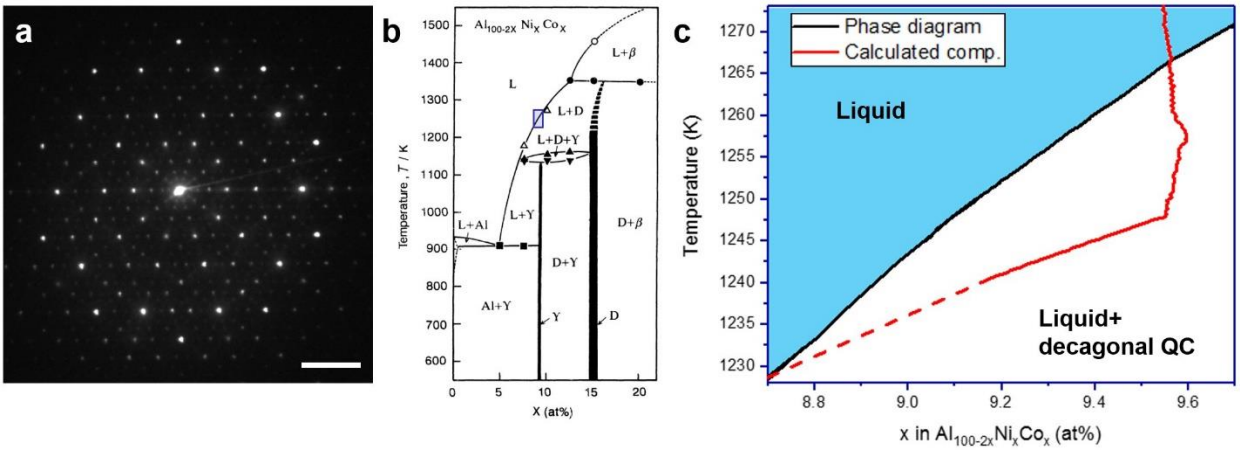

Fig. 4.1. *System-of-interest*. (a) Electron diffraction pattern of the solid QC phase, which proves unambiguously the decagonal symmetry of the QC phase in the Al-Ni-Co system. The scale bar measures 2 nm^{-1}. (b) Partial section of the $Al_{100-2x}Ni_xCo_x$ pseudo-binary, equilibrium phase diagram as measured by Yokoyama *et al.*[46]. *L* and *D* indicate the liquid and decagonal QC phases, respectively. (c) Calculated, alloy composition within the FOV during the XRT experiment (red) superimposed on the same phase diagram (black). The region plotted in (c) corresponds to the blue boxed region in (b). The solid QC grows and then melts due to the "pile up" of Al in the liquid phase. The dotted line indicates extrapolated compositions.

4.2. Microstructure evolution

4.2.1. 3D full volume reconstructions

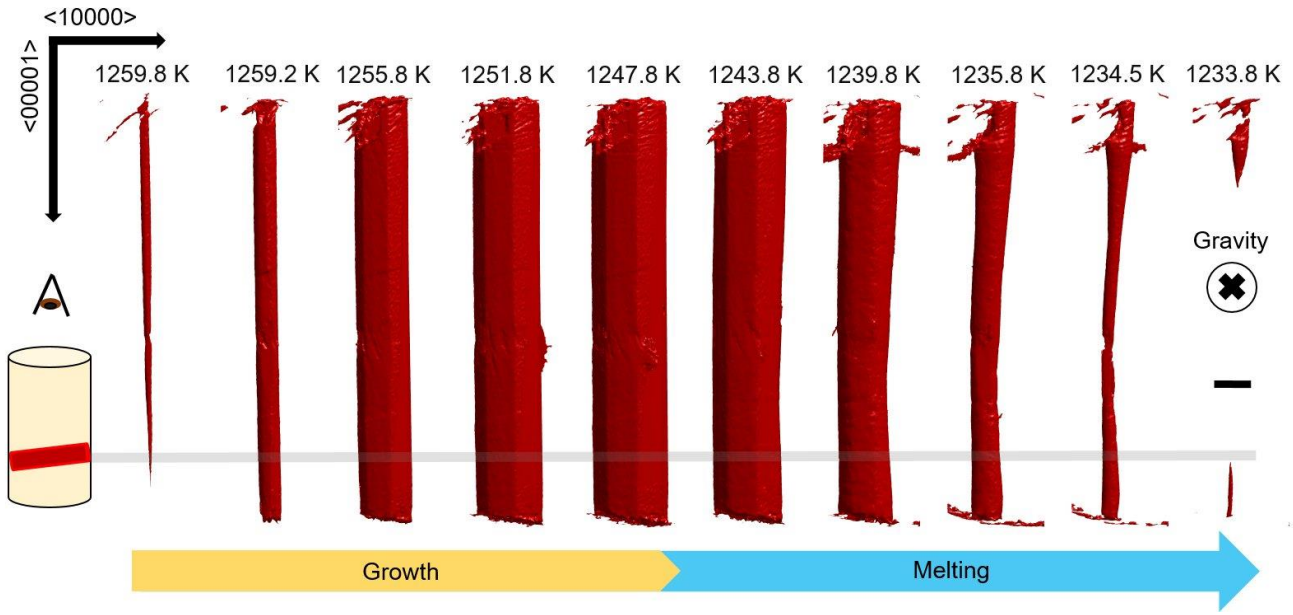

Fig. 4.2. *Three dimensional reconstructions* (bird's eye view, see inset) of d-QC growth and melting during continuous cooling. The temperature decreases from left to right as a function of reaction time. Temperatures and times are as follows: 1259.8 K (800 sec), 1259.2 K (840 sec), 1255.8 K (1040 sec), 1251.8 K (1280 sec), 1247.8 K (1520 sec), 1243.8 K (1760 sec), 1239.8 K (2000 sec), 1235.8 K (2240 sec), 1234.5 K (2320 sec) and 1233.8 K (2360 sec) respectively. The start of the clock (0 sec) corresponds to the start of the XRT experiment. Scale bar measures 100 μm.

We detected one single QC within the tomographic FOV during continuous cooling. Its evolution at ten representative time intervals is depicted in **Fig. 4.2**. The QC grows from the one side to the other side of the Al_2O_3 skin that contains the molten alloy (not pictured). The QC is anchored to this oxide skin on both sides and therefore the QC does not sediment to the bottom of the melt. The growth velocity along the periodic direction is approximately over two orders of magnitude greater than the velocity along the aperiodic direction, which corroborates the *ex situ* observations of Gille *et al*. [110] and Meisterernst *et al*. [111]. The "long axis" parallel to <00001> represents the fast-growing, periodic direction and <10000> represents the set of ten slow-growing, aperiodic directions. When the QC melts, it does not mirror the growth pathway, which is fully faceted and nearly isotropic in the aperiodic <10000> directions. Rather, we observe marked curvature of the solid-liquid interface upon melting. Therefore, the growth and dissolution processes do not have time-reversal symmetry and hence different physical principles must be invoked in order to explain these different behaviors. Furthermore, we investigated a cross-section

of the 3D reconstructed volume to better understand the growth and dissolution processes within the aperiodic plane. The region selected for our analysis is highlighted with a grey line in **Fig. 4.2** and includes a thickness of 20 μm along the periodic direction.

4.2.2. Analysis of ten-fold plane

Isochrones of the solid-liquid interface in the ten-fold, {00001} plane (corresponding to the grey line in **Fig. 4.2**) are shown in **Fig. 4.3** with 80 sec increments. The interfaces are colored according to their local, interfacial velocity, which was calculated using the nearest-neighbor approach given by Shahani *et al.* [112] (see **Sec. 3.1.5**). We follow the thermodynamic convention, wherein positive velocity indicates growth, and negative velocity indicates melting. In the initial stage of growth, facets are not readily distinguishable at the resolution of XRT. Nevertheless, the facets become more apparent as the QC grows: The fourth isochrone (1040 sec) from the center in Fig. **4.3(a)** visibly displays the ten facets (numbered). After the QC is fully faceted, its growth is nearly isotropic, i.e., the growth velocity is almost uniform across all ten facets. Any differences in the facet velocities during growth are most likely due to thermosolutal convection. During dissolution (**Fig. 4.3(b)**), however, the interfacial velocity is faster at the bottom of the QC (near facet 10) than the top (near facet 5). Due to the anisotropic nature of melting, the QC surface loses its facets and becomes increasingly rounded as a function of time. **Fig. 4.3(c)** depicts the average velocity of each QC facet in time. Consistent with **Fig. 4.3(a)**, the velocities are almost the same for all ten facets during growth. However, during melting (i.e., after 1520 sec) there is a marked deviation in the facet velocities, which in turn depends on the facet orientations. The facets at the bottom melt faster than the facets at the top (*cf.* **Fig. 4.3(b)**).

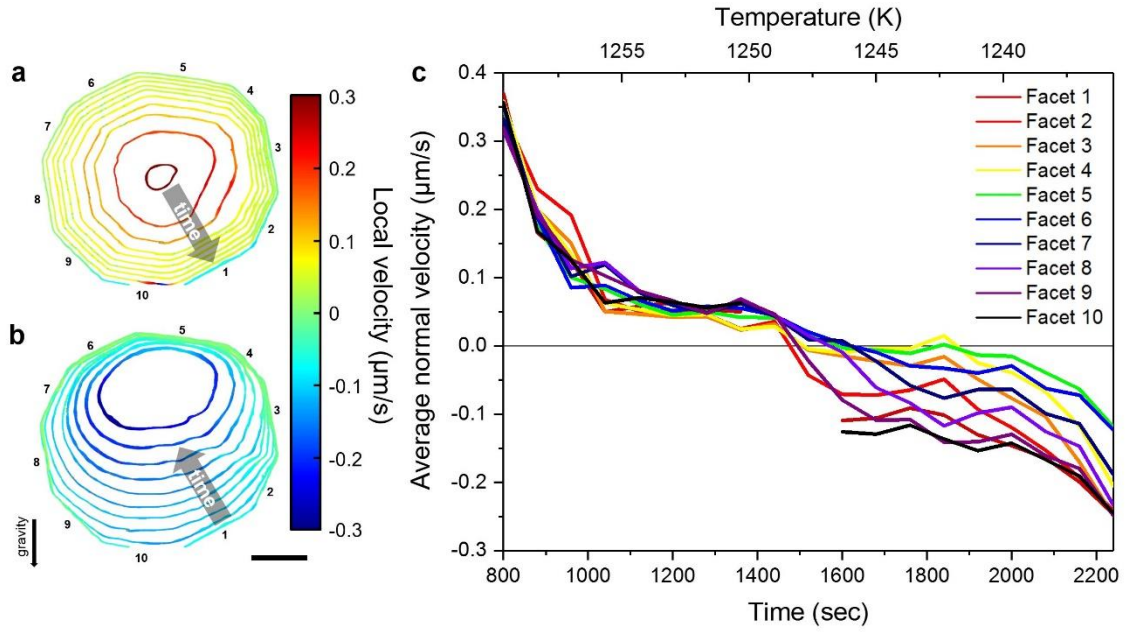

Fig. 4.3. *Evolution of the ten-fold plane* as a function of time for QC (a) growth and (b) dissolution. Isochrones of the solid-liquid interface are colored according to their interfacial velocity, which is positive for growth and negative for melting. During growth, the QC develops ten distinct facets (numbered from 1 to 10), while during dissolution, the QC loses these facets and becomes increasingly rounded. Discontinuities in the calculation of interfacial velocity for facet 1 and 10 are due to the fact that the QC grows out of the tomographic FOV when it is largest. Scale bar measures 50 μm. (c) Average normal velocity of each facet.

4.3. Analysis of liquid phase compositions

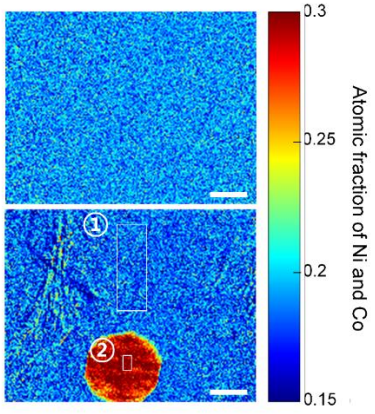

Fig. 4.4. *Analysis of time-dependent driving force*. (a) X-ray projection images collected at 1272.5 K (40 sec, top image) and 1247.8 K (1520 sec, bottom image) during continuous cooling, respectively. The region contained in the first white box ("1") was used to calibrate the average intensity from the liquid, $< x^{L}_{Co,Ni} > (t)$, and the second white box ("2") was used to calibrate the average intensity from the QC. The wrinkles in the bottom image are due to the thin oxide skin. Scale bars measure 100 μm.

In addition to the morphology and dynamics of the QC, we measured the time-dependent composition of the liquid phase during solidification. This analysis is possible because the composition of the liquid that is examined in the field of view changes due to solute rejection and convection. This was done by analyzing the variation of the intensity in the X-ray projection images. In an absorption contrast X-ray imaging experiment, a higher intensity is typically associated with low atomic number elements in the microstructure due to less attenuation of the incident beam [85]. Recall that in our experiment, non-congruent growth (*i.e*., rejection of Al) gave rise to X-ray absorption contrast and induced an intensity difference. Put more quantitatively, using a monochromatic source, Husseini *et al.* proved that the intensity should vary linearly across the X-ray projection image for small, linear changes in atomic fraction [113]. Thus, the observed intensity can be directly mapped to composition, provided that the projection intensity has been calibrated against some features in the microstructure of known composition [114]. As demonstrated by Becker *et al.* [115], this approach is viable for *both* monochromatic and polychromatic sources. For instance, Becker *et al*. calculated the composition of an Al-Ge alloy using a laboratory-based polychromatic X-ray source by calibrating the projection intensity against two liquid alloys of different compositions [115]. Here, we used the following two features in the microstructure to correlate projection intensity (a.u.) to composition (at. %):

1. The solid QC phase. Note the proportion of Al atoms to the heavy atoms (Ni and Co) in the QC is 7:3 at any temperature according to the phase diagram (**Fig. 4.1(b)**) [46]. The projection intensity of the QC along <00001> is denoted "2" in **Fig. 4.4**. The average projection intensity is measured when the QC is viewed "end-on," i.e., there are no pockets of liquid in the path of the beam within region "2".
2. The liquid phase at equilibrium. At the instance that the QC stops growing, the supersaturation (*i.e*., a driving force for crystal growth) in the liquid phase must be equal to zero and hence the liquid phase is at equilibrium. In this case, the composition of the liquid phase can be read directly from the phase diagram (**Fig. 4.1(b)**) [46], since the alloy temperature is known. The projection intensity of the liquid phase at equilibrium is denoted "1" in **Fig. 4.4**. For comparison, we also show the highly supersaturated liquid phase prior to QC nucleation, directly above it.

In this manner, we calculated the average, time-dependent composition of the liquid phase, which we write as $< x^{L}_{Ni,Co} > (t)$, during the growth process. Note that it is impossible to decouple the contributions of Ni and Co within $< x^{L}_{Ni,Co} > (t)$ using only the above two conditions; to do so would require a third such condition. Thus, $< x^{L}_{Ni,Co} > (t)$ represents only the total atomic fraction of the heavy elements Ni and Co in the liquid phase at a particular instance in time. Our calculation of $< x^{L}_{Ni,Co} > (t)$ is still valuable as it permits us to measure the time-dependent supersaturation during QC growth: For instance, when $< x^{L}_{Ni,Co} > (t)$ is much greater than the equilibrium liquidus composition given by $x^{L,equil.}_{Ni,Co}(t)$, the liquid phase is highly supersaturated in the heavy elements Ni and Co. This situation occurs immediately following QC nucleation. The relationship between supersaturation and QC velocity will be dealt with below.

4.4. Growth

4.4.1. Growth in aperiodic directions

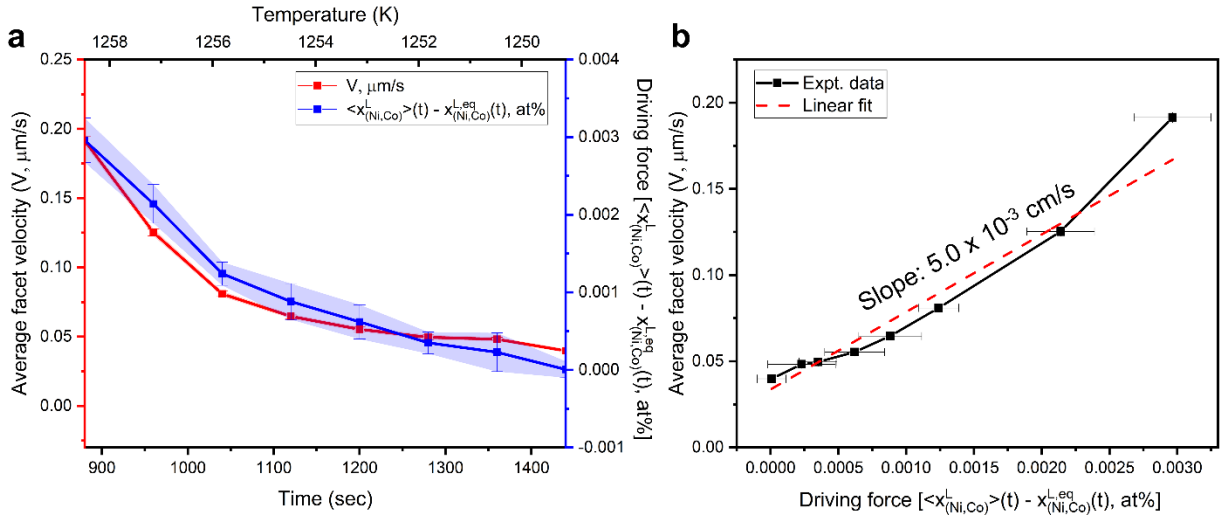

Fig. 4.5. (a) Average facet velocity of the ten quasicrystalline facets of the decagonal QC (red) and kinetic driving force (blue), during the growth process. The driving force of supersaturation was calculated by subtracting the equilibrium liquid composition from the instantaneous liquid composition, see text and **Eq. 4.1** for details. Errors in the measurement of average facet velocity are due to small errors in segmentation while those in the calculation of driving force are attributed to errors in the calibration of the phase compositions at equilibrium. (b) Average facet velocity *vs.* driving force. The slope gives the kinetic coefficient β_s associated with the growth process.

In general, the morphology of a growing faceted crystal results from an interplay of interfacial kinetics and bulk transport. The fact that the interfacial velocity is approximately the same for the ten <10000> aperiodic directions at each time interval during growth (see **Fig. 4.3(a)**) — irrespective of the physical location of these facets in the laboratory frame — suggests that facet motion is largely governed by *interfacial mobility* rather than *bulk transport*. To lend quantitative support for this claim, we applied transition-state theory as follows: During interface-limited growth, the growth rate is limited by clusters incorporating into the QC at the solid-liquid interface, wherein the clusters must overcome an activation energy barrier [63, 64, 116]. In this case, the growth rate V is proportional to the difference in a forward flux as described in **Sec. 2.2.2**.

For QC growth to occur, $I_{\mathrm{L}\to\mathrm{QC}} > I_{\mathrm{QC}\to\mathrm{L}}$, whereas at equilibrium $I_{\mathrm{L}\to\mathrm{QC}} = I_{\mathrm{QC}\to\mathrm{L}}$ and hence $\mathrm{V} = 0$. If the growth occurs under weak supersaturation, one can use **Eq. 2.15** [63, 64] to describe QC growth from the Al-Ni-Co melt

$$\mathrm{V(t)} = \beta_s \left[< \mathrm{x}^{\mathrm{L}}_{\mathrm{Co,Ni}} > (\mathrm{t}) - \mathrm{x}^{\mathrm{L,equil}}_{\mathrm{Co,Ni}}(\mathrm{t}) \right]^n \qquad (4.1)$$

where $< \mathrm{x}^{\mathrm{L}}_{\mathrm{Co,Ni}} > (\mathrm{t})$ and $\mathrm{x}^{\mathrm{L,equil}}_{\mathrm{Co,Ni}}(\mathrm{t})$ are the *instantaneous* and *equilibrium* compositions of the liquid phase, respectively; the square-bracketed term represents the supersaturation (*i.e.*, driving force) that is required for QC growth to occur. More details can be found in **Sec. 2.2.2**.

In practice, we measured $< \mathrm{x}^{\mathrm{L}}_{\mathrm{Co,Ni}} > (\mathrm{t})$ directly from the X-ray projection images as a function of time (see **Sec. 4.3**) and $< \mathrm{x}^{\mathrm{L,equil}}_{\mathrm{Co,Ni}}(\mathrm{t}) >$ from the as-calculated phase diagram [46]. Hence, our *in situ* imaging experiment provides a unique window into the time-dependent driving force associated with QC growth. To simplify the analysis, we assumed that the variation of the kinetic coefficient β_s is negligible within the temperature range of 1259.8 K to 1247.8 K at which growth occurs, and so β_s is considered to be a constant value. If the assumption presented in **Eq. 4.1** is satisfied, the QC growth process is dominated by the kinetics of interface attachment in the regime of weak supersaturation. As shown in Fig. **4.5(a)**, the trends in interfacial velocity and driving force are comparable to each other during the growth process. By fitting the time-dependent growth velocity *vs.* driving force data (**Fig. 4.5(b)**) to a function of the form given in **Eq. 4.1**, we calculated the kinetic coefficient β_s and the temporal exponent n as 5.0 x 10^{-3} cm s^{-1} and 1.0021, respectively. An R^2 value of 0.963 was obtained, indicating a good fit of the linear model to the experimental data. Thus, the growth of the QC in the <10000> aperiodic directions

follows first-order kinetics. In a similar sense, Refs. [79, 80] suggest that the Al-Pd-Mn icosahedral QCs grow from an undercooled liquid phase *via* an interface-limited, first-order growth mechanism. In addition, we can convert our value of $\beta_s = 5.0 \times 10^{-3}$ cm s^{-1} to the more widespread $\beta_m = 2.5 \times 10^{-6}$ cm s^{-1} K^{-1}, which represents the kinetic coefficient in an undercooled melt (m). In converting from one form of the coefficient to the other, we have made use of the slope of the liquidus curve in **Figs. 4.1(b,c)**.

The magnitude of the kinetic coefficient also merits further discussion. According to Chernov [76], Markov [77], and Land *et al.* [75], the kinetic coefficient has a "steric" character: It is inversely proportional to the size of the attaching species because a larger species moves more slowly than a smaller one. Moreover, it takes more time for the larger species to rotate to the correct orientation [75]. In this way, the QC clusters should overcome a configurational entropy-type barrier [76] in order to incorporate into the solid QC phase. Using this logic, one might expect that the kinetic coefficient of an aperiodic crystal — that is thought to be built from the attachments of large clusters — to be smaller than that of other simple substances, such as pure metals [117-120] and intermetallics [121, 122]. In this way, the kinetic coefficient could serve as a measure of structural complexity. Indeed, the kinetic coefficients β_m of QCs — including Al-Cu-Fe [123], Al-Pd-Mn [79, 123], and Al-Ni-Co (this work) — are all significantly smaller than those of periodic, elemental metallic crystals by approximately six to nine orders of magnitude, and those of periodic, intermetallic crystals by two to eight orders of magnitude (**Table 2**).

Material	**Kinetic coefficient, β_m (cm s^{-1} K^{-1})**	**Reference**
Au	36.3 {100}	Hoyt *et al*. [117]
	20.7 {110}	
	10.1 {111}	
Ni	52 {100}	Hoyt *et al*. [118]
	40 {110}	
Fe	30.5 {100}	Watanabe *et al*. [119]
	25.7 {110}	
Cu	46 {100}	Hoyt *et al*. [120]
	27 {110}	
	19 {111}	Herlach [121]
FeSi	1.4	Herlach [121]
CoSi	2.1	Nagashio & Kuribayashi [122]
$Y_3Al_5O_{12}$ (YAG)	$3.5\text{x}10^{-3}$	Nagashio & Kuribayashi [122]
Al_2O_3	~$3.5\text{x}10^{-2}$	
Al-Ni-Co d-phase	$2.5\text{x}10^{-6}$ {10000}	This work
Al-Pd-Mn i-phase	$9.0\text{x}10^{-5}$	Thi *et al*.[79]
	$9.4\text{x}10^{-7}$	Dong *et al*.[123]
Al-Cu-Fe i-phase	$3.0\text{x}10^{-8}$	Dong *et al*.[123]

Table 4.1. *Kinetic coefficients of undercooling in a liquid phase, β_m,* of various crystals, as determined from both experiments and simulations. The values of β_m of aperiodic crystals are all significantly smaller than those of periodic, elemental metallic crystals by approximately six to nine orders of magnitude, and those of periodic, intermetallic crystals by two to eight orders of magnitude, indicating a slower growth rate. The kinetic coefficient derived here for the d-QC phase is consistent with other studies on the i-QC phase.

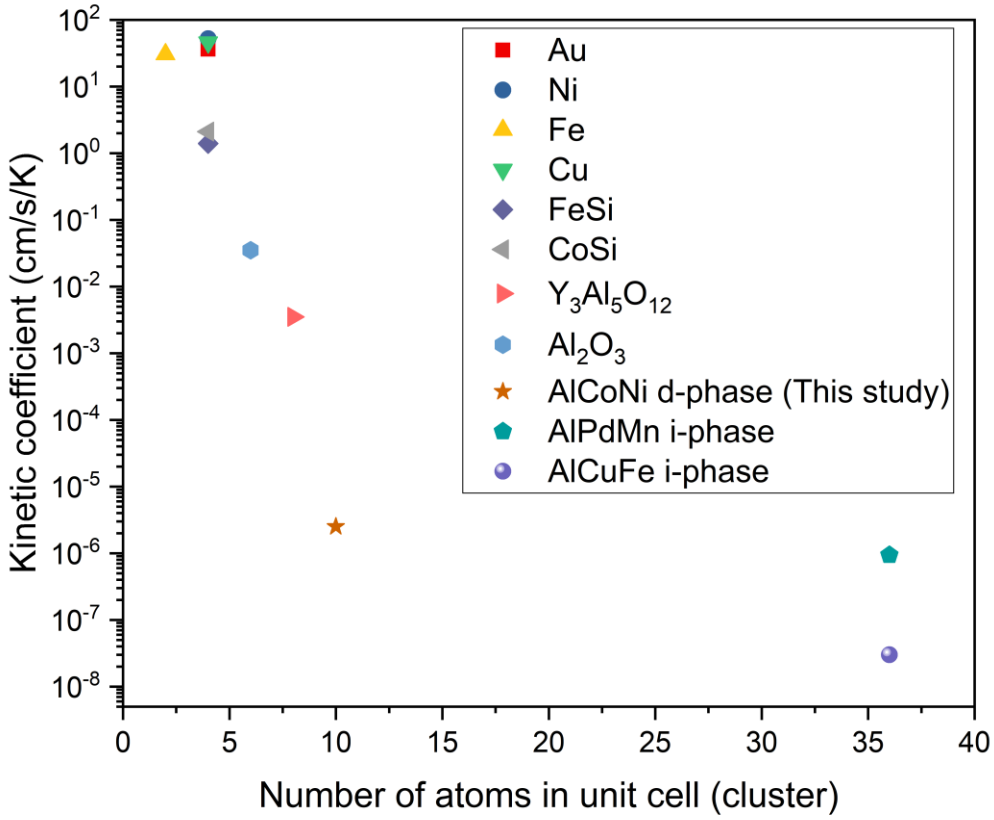

Fig. 4.6. Number of atoms in unit cell (cluster) *vs.* kinetic coefficient β_m plot showing the larger unit cell (cluster), the more sluggish growth rate (smaller β_m). The source of the kinetic coefficients β_m are **Table 4.1**.

See also **Fig. 4.6** which summarizes these trends. The kinetic coefficients listed for aperiodic crystals were determined from X-ray radiographs [79] and a combination of the Avrami approach and differential thermal analysis [123]. We assumed that the cluster in d-QC is composed of two layers of pentagons and the cluster in i-QC is the icosahedral second shell of the Tsai-type cluster [124]. Thus, it is entirely plausible that a higher configurational entropy-type barrier contributes to a more sluggish growth rate.

4.4.2. Growth in periodic directions

Our results indicate a stark contrast in the growth of the QC along the periodic and aperiodic directions. The growth rate along the periodic <00001> direction is about two orders of magnitude greater than the growth rate in the aperiodic <10000> directions, and this anisotropy in the

interfacial velocities results in an elongated shape of a decagonal prism, see **Fig. 4.2**. To explain these trends, higher-order kinetics deserves consideration since the degree of supersaturation is nearly uniform around the QC. According to a study [125] of an Al-Cu-Co single decagonal quasicrystal by X-ray topography, contrast associated with a screw dislocation appears in the {00001} plane. This suggests that growth along <00001> occurs *via* second-order kinetics wherein the interfacial velocity is related to the square of the driving force (*i.e.*, **Eq. 4.1** with $n = 2$). The spiral ledges provide sites for crystal growth and thus there is no need for ledge nucleation. Consequently, the growth rate of crystal along the periodic direction is likely to be faster than in the aperiodic directions, even with a small amount of supersaturation [63, 64, 116]. Future improvements in higher resolution dynamic imaging would provide more conclusive support of this mechanism.

4.5. Dissolution

During dissolution, the QC loses its faceted solid-liquid interfaces, achieving a more rounded morphology (*cf*. **Fig. 4.3(b)**). Mechanistically, this may occur if the weakly bound, corner clusters leave the solid as soon as melting is initiated, further exposing new corners and perpetuating the melting process. The resulting, smooth curvature of the solid-liquid interface upon dissolution suggests that the removal of clusters occurs in a continuous way instead of in abrupt jumps. That is, dissolution is not an activated process, in contrast to growth. As a result, the dissolution process does not follow the geometric models mentioned above because dissolution is dominated by non-local, transport processes, as will be further explained below. If QC dissolution occurred via a local mechanism, the corners should evolve into facets, as has been observed by Wettlaufer and coworkers for a twelve-sided snowflake [126]. However, this behavior is not seen here (**Fig. 4.3(b)**).

Importantly, the rate of dissolution is not the same for each of the ten corners, otherwise the isochrones of the solid-liquid interface would be perfectly circular. Rather, the melting velocities depend strongly on the *physical* orientation, and not the *crystallographic* orientation. As a result, the melting process is asymmetric. For instance, after 1520 sec, facets 1, 9, and 10 show greater velocities than other facets, see **Figs. 4.3(b,c)**. Due to the influence of gravity, which points downward in **Fig. 4.3**, the heavy-atom Ni and Co-rich clusters at the bottom of the QC are removed

more easily than at the top of the QC. The detached clusters tend to sink in the Al-rich liquid. Hence, the composition of heavy elements, *i.e*., Ni and Co, near the bottom interface of the QC decreases, while the composition of heavy elements near the top interface accumulates during the melting process. In other words, there exists a density difference between the top and bottom facets of the QC that gives rise to buoyancy-driven convection. Consequently, the bottom facet is brought into contact with an Al-rich liquid that, in turn, causes it to dissolve at a faster rate. Thus, transport kinetics are responsible for the unusual "egg-like" morphology of the QC at late times.

The increase in the interfacial velocity of the bottom-most QC facets as dissolution progresses suggests an unstable distribution of heavy elements adjacent to these facets in the liquid phase, see **Figs. 4.3(b-c)**. A similar behavior was recently observed *via in situ* X-ray radiography for Sn-Bi dendrites [127] that were solidified parallel to gravity, in which the heavy elements formed large plumes ahead of the growth front. These plumes disturbed the stability of the growing dendrites, such that their growth velocity was highly inconsistent over time. Taken altogether, interfacial kinetics brings about crystalline order while gravity-induced convection leads to microstructural heterogeneity, in both periodic crystals and QCs alike.

Chapter 5. Growth of Approximant X phase and Comparison with d-QC

Our work in **Ch. 4** supports the idea that *the kinetic coefficient decreases as the complexity of the growth unit or cluster increases*. It is worth mentioning that an alternate viewpoint that does not rely on the cluster description is offered by Herlach [121]. He suggested that short-range diffusion is necessary for the atoms to sort themselves out to find the proper sublattice position in a given intermetallic solid. In contrast, the attachment kinetics at the solid–liquid interface of a simple crystal (such as a pure metal) are only collision limited [128]. Consequently, for diffusion-limited atomic attachment driven growth of intermetallics, the kinetic coefficient should be orders of magnitude smaller as compared with collision-limited growth of simple crystals, since the relaxation frequency for atomic diffusion (former case) is much less than the Debye frequency (latter case).

Based on the steric argument given by Land & De Yoreo [75] and Chernov [76], one might assume that the kinetic coefficients of QCs and their approximants are the same, owing to their similar structural motifs. To test this hypothesis, we captured in real time and at elevated temperature the solidification dynamics of the X phase during `fast' X-ray imaging and compared the results against the d-QC reported in **Ch. 4**.

5.1. Microstructure evolution

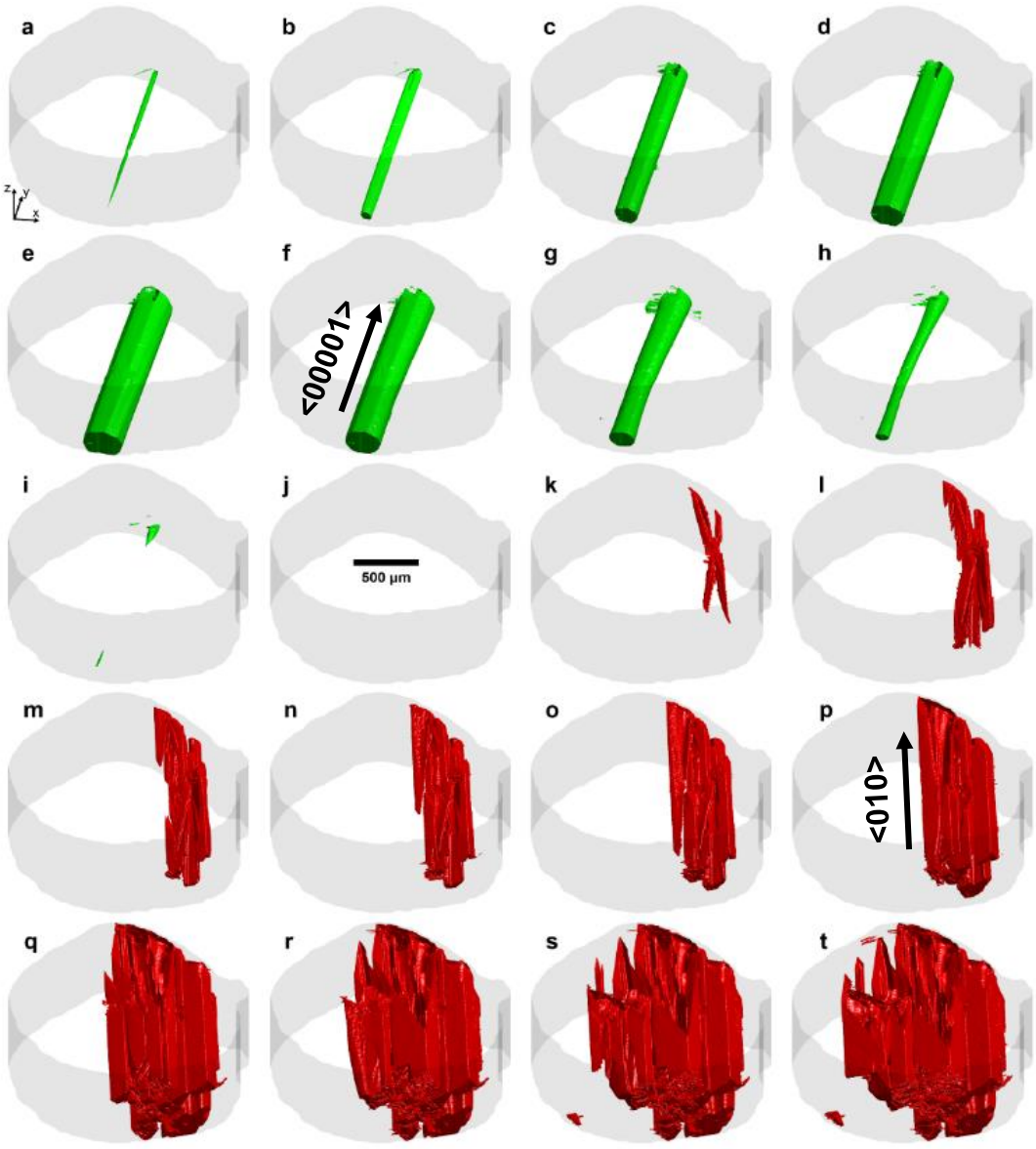

Fig. 5.1. Three dimensional reconstructions of (a-e) Al-Co-Ni *d*-QC growth, and (f-j) its dissolution (in green), followed by (k-t) *X* phase crystallization (in red) during continuous cooling (1 K min^{-1}). The *z* axis in the specimen frame points along the rotation axis of our cylinder sample. Temperatures and times are as follows: (a) 1259.8 K (800 s), (b) 1259.2 K (840 s), (c) 1257.2 K (960 s), (d) 1253.2 K (1200 s), (e) 1247.8 K (1520 s), (f) 1243.5 K (1780 s), (g) 1238.5 K (2080 s), (h) 1235.2 K (2280 s), (i) 1233.8 K (2360 s), (j) 1233.8 to 1227.2 K (2360 to 2760 s), (k) 1227.2 K (2760 s), (l) 1226.8 K (2780 s), (m) 1226.5 K (2800 s), (n) 1226.2 K (2820 s), (o) 1225.8 K (2840 s), (p) 1224.5 K (2920 s), (q) 1220.8 K (3140 s), (r) 1218. 8 K (3260 s), (s) 1217. 8 K (3320 s), and (t) 1215.5 K (3460 s), respectively. The times given in the parentheses are with respect to the start of the XRT experiment at 1273.2 K (0 s). A thin grey layer indicates the Al_2O_3 protective skin of the molten alloy sample that was grown naturally by thermal oxidation. We observe the nucleation and growth of a *single* d-QC at high temperatures and *multiple* X phase crystals.

We show in **Fig. 5.1** three-dimensional reconstructions of one single d-QC (coloured in green) and multiple X phase crystals (coloured in red). Note that this is the same d-QC from **Ch. 4**, reprinted here for ease of comparison. The surrounding liquid phase is rendered transparent. The d-QC nucleates at 1259.8 K (**Fig. 5.1(a)**) and grows from one side of the protective Al_2O_3 skin to the other, along the periodic <00001> direction [2]. Only one QC nucleation was detected within the tomographic field-of-view (FOV), for the duration of the *in situ* experiment. Nucleation of the X phase crystals takes place later, at 1227.2 K (**Fig. 5.1(k)**). Quantitative analysis of their nucleation and growth behaviors will be given in the subsequent sections.

5.2. Nucleation dynamics: d-QC *vs.* X phase

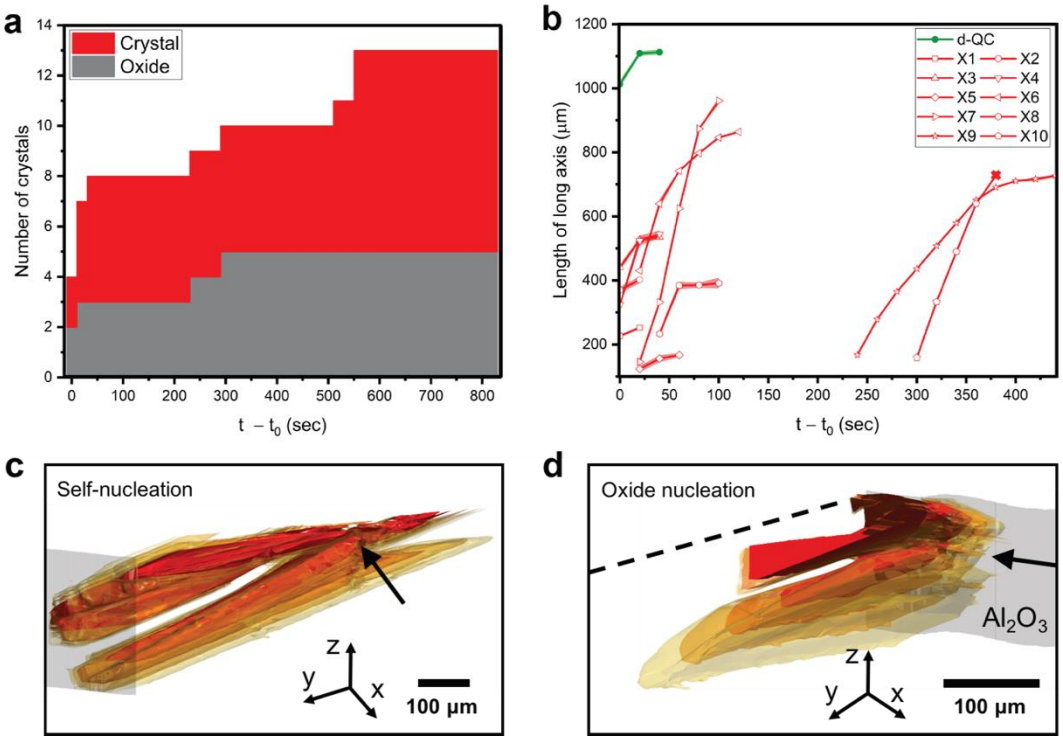

Fig. 5.2. (a) Number of nucleated X phase crystals as a function of time t following the first nucleation event at time $t = t_0$. Only those nucleation and growth events that occurred within the tomographic FOV are recorded. Nucleation is heterogeneous and takes place on either existing crystal surfaces or the protective Al_2O_3 oxide skin of the sample, with nearly equal probability. (b) Length of the "long axis" (parallel to the crystallographic b direction) of X phase crystals versus time (red curves). Shown for comparison is the growth trajectory of d-QC along its long axis <00001> (green curve). All lengths were measured when the crystals were fully contained within the tomographic FOV except crystal #10; the cross mark at $t - t_0 = 380\ s$ for crystal #10 indicates that it grew out of the tomographic FOV during the *in situ* experiment. Measurement errors for crystal (a) numbers and (b) lengths are minimal

and arise from counting statistics. Superimposed 3D reconstructions of X phase crystals that nucleated heterogeneously from (c) the existing crystal surface and (d) protective Al_2O_3 oxide skin of the sample. Both (c) and (d) contain four different time-steps with a temporal discretization of 20 s, rendered with decreasing opacity (from opaque red to translucent yellow). The thick arrows in (c, d) indicate where the nucleation first occurred and the dashed line in (d) indicates where the reconstructed data were cropped for ease of visualization. The grey region represents the Al_2O_3 oxide skin.

During the tomographic scan, a total of 13 crystals of the X phase were captured in the FOV (**Fig. 5.2**). By tracking their formations in 4D, we identify two distinct heterogeneous nucleation mechanisms: (i) *self-nucleation*, wherein intermetallics themselves act as potent nucleation sites for new X phase intermetallic crystals, at large distances away from the specimen surface. The second mechanism is (ii) *Surface oxide nucleation*, wherein the specimen surface (Al_2O_3) acts as a nucleant for the X phase. A similar behaviour was reported by [129-131] who considered the nucleation of another Al-based intermetallic, β-Al_5FeSi. We did not detect homogeneous nucleation. The 4D data was thoroughly analysed to classify every X phase crystal according to these two categories, see Fig. **5.2(a)**. It can be seen that the total number of nucleation events increases continuously during continuous cooling. This might be because of the strongly anisotropic growth mechanism of the X phase, which grows along sharp crystallographic <010> directions (see **Fig. 5.1(p)**). Thus, the X phase cannot grow into the supersaturated liquid regions that are not in the path of its "long axis." Constitutional undercooling builds up in these liquid regions until it exceeds the necessary nucleation undercooling. At this point, nucleation events are triggered around the existing crystals based on the above-mentioned two mechanisms (i, ii). Similar arguments were made by [132] to justify their *in situ* observations of repeated nucleation events of faceted Cu_6Sn_5 crystals. **Fig. 5.2(a)** indicates that at early times, such heterogeneous nucleation events occur on the surface oxide and the existing crystals with near-equal probability; at long times, there is more surface area on the exposed X phase facets, resulting in a slight bias towards self-nucleation. We expect that these 13 nucleation and growth events are representative of nucleation and growth throughout the entire sample; this is because the alloy melt had been homogenized for around 400 s (**Fig. 5.1(j)**) before the first X phase crystals were observed. Three-dimensional examples of two different growth mechanisms are illustrated in Figs. **5.2(c, d)**.

Fig. **5.2(b)** shows the length of the "long axis" for each of the nucleated X phase crystals as a function of time. To interpret this plot, we must consider the interactions between the nucleated crystals: Their growth may be physically blocked by each other or the oxide skin (hard collisions); further elongation along the b-axis may also be suspended due to a depletion of the available solute

in the melt (soft collisions) [133, 134]. The latter occurs when the crystal separation is smaller than the solute diffusion length (see **Sec. 2.2.1**). Due to a combination of both hard and soft collisions, the length of the X phase rods tends to be shorter (on average) than that of the single d-QC, which grows quickly and without any interruption. In contrast, only four X phase crystals are able to extend from one side of the oxide skin to the other. Altogether, by combining **Figs. 5.2(a, b)**, it is clear that the X phase rods are *shorter and more numerous* that the d-QC.

At first glance, the comparatively low nucleation rate (# nuclei per unit volume per unit time) of the d-QC may seem incongruous with its low solid-liquid interfacial energy γ^{SL} [55] and higher nucleation temperature T^*. According to classical nucleation theory [135, 136], both of these factors tend to increase the nucleation rate over that of the approximant phases. Yet this rudimentary analysis does not consider the influence of solute, otherwise known as *constitutional undercooling*. The development of constitutional undercooling — at the interface of the first crystals to nucleate — starts a "wave" of nucleation events throughout the bulk liquid [137]. Some understanding of these constitutional effects can be gained by considering the predicted solidification paths of both d-QC and X phases, see **Fig. 5.3**. Both curves were calculated with the aid of Thermo-Calc [138], using a recent thermodynamic assessment of the Al-Co-Ni system as input [108]. The *growth restriction factor* (GRF) is defined as the initial rate of development of the constitutional undercooling at the solid-liquid interface [137], and can be found directly from **Fig. 5.3** as

$$GRF = -\left(\frac{dT}{df_s}\right)_{f_s \to 0} \tag{5.1}$$

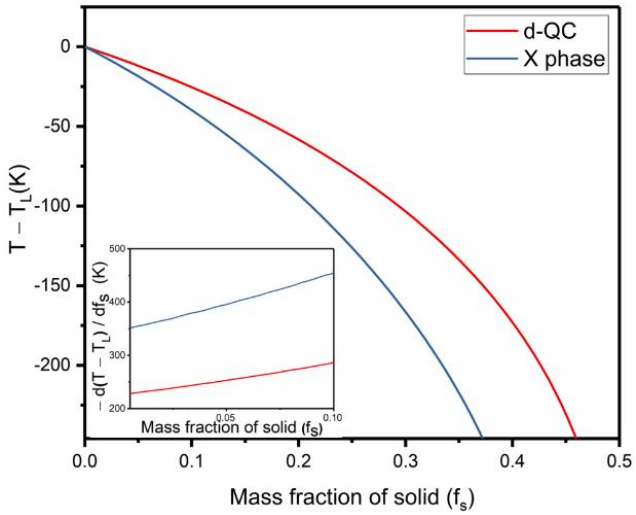

Fig. 5.3. Mass fractions f_s of the solid d-QC (red) and X phase (blue) *vs*. relative temperature $T - T_L$, where T_L represents the liquidus temperature of either phase. Both curves were calculated using the recent CALPHAD-based assessment of the Al-Co-Ni system from [108]. The first derivative dT/df_s of these two curves in the limit of $f_s \to 0$ represents the growth restriction factors (GRF) of the d-QC and X phase (see inset). The X phase has a higher GRF by a factor of around 1.5.

In calculating the GRF, we assume two-phase coexistence only (*e.g.*, liquid and X phase). Furthermore, we have considered the exact same master alloy composition as that of our XRT experiment (Al-9.55at%Ni-9.55at%Co). The inset derivatives in **Fig. 5.3** indicate that the GRF of the X phase is approximately 1.5 times greater than that of the d-QC in the limit of vanishingly small solid fraction, f_s. Consequently, a large constitutional undercooling develops in a relatively short growth distance [132] for the X phase, enabling nucleation events to occur closer together (as experimentally observed in **Figs. 5.1 and 5.2**). Thus, due to the growth anisotropy of the faceted X phase and its high GRF, it is easier for new crystals to nucleate from the liquid than it is for a single crystal to branch during growth (like for a metal dendrite). In spite of this relatively high nucleation rate, only a few X phase rods can connect to both sides of the oxide skin, due to a high frequency of both hard and soft collisions, as mentioned previously.

5.3. Growth dynamics: d-QC *vs.* X phase

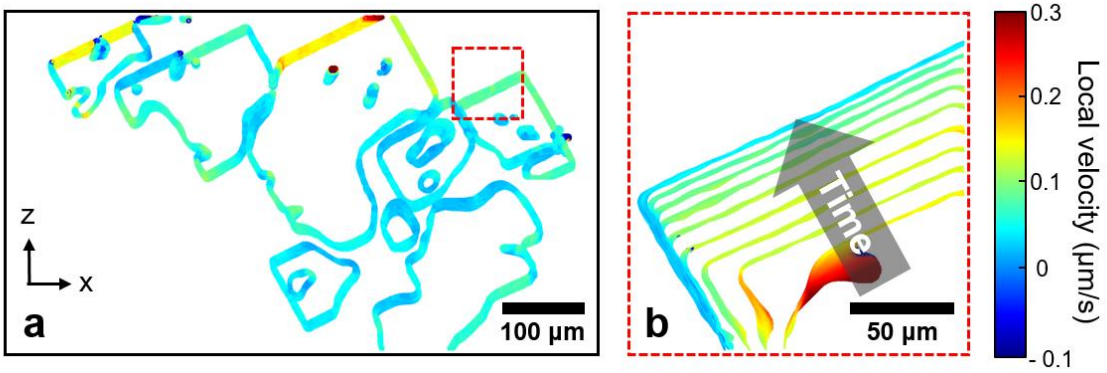

Fig. 5.4. (a) Solid-liquid interfaces coloured by the local interfacial velocity at 1216.8 K. Positive interface velocity represents growth and negative velocity represents dissolution. The shown viewpoint is parallel to the specimen y-axis and the crystallographic <010> direction. The red dashed box was used to calculate the growth velocity V of a single X phase crystal, see text for details. (b) Interfacial isochrones with 80 s time increments within the dashed boxed region. The grey arrow indicates the motion of the facet in time. The represented temperatures and times are as follows: 1226.2 K (2820 s), 1224.8 K (2900 s), 1223.5 K (2980 s), 1222.2 K (3060 s), 1220.8 K (3140 s), 1219.5 K (3220 s), 1218.2 K (3300 s), 1216.8 K (3380 s), and 1215.5 K (3460 s).

Once the constitutional undercooling has been relieved, the nucleated X phase crystals must grow to keep up with the cooling rate. To explain the growth kinetics of X phases we used the same approach as used in **Ch. 4**, see **Eq. 4.1**, which assumes implicitly that growth is governed by the kinetic contribution to the total driving force. This is a reasonable assumption to make due to the appearance of facets (**Figs. 5.1 and 5.4**), which inherently have few positions on the solid surface that are available for attachment [139, 140]. That is, not every atomic (or cluster) jump from the liquid to the solid will be successful, and thus the growth process will be limited by the kinetics of attachment at the solid-liquid interface. In other words, the kinetic coefficient β_s is much less than the "diffusive speed" given by $\beta_{diff} = \frac{\widetilde{D}^L}{R(c^S_{Co,Ni} - \langle c^L_{Co,Ni} \rangle)}$, where $\widetilde{D}^L$ is the interdiffusivity in the liquid phase, R is the crystal size, and $c^S_{Co,Ni}$ is the composition of Co and Ni in the solid X phase. We can compare the characteristic speeds β_s and β_{diff} using some realistic parameters. Assuming that $\widetilde{D}^L$ is equivalent to the self-diffusivity of Al in its melt ($8 \pm 0.7 \times 10^{-5}$ cm^2/s at 1020 K) [141], we let R be 1×10^{-3} cm; and we take $c^S_{Co,Ni} - \langle c^L_{Co,Ni} \rangle$ to be approximately 0.15, based on our compositional analysis. The calculated β_{diff} is 6×10^{-1} cm/s which is far greater than typical values seen for β_s (*e.g.*, 5×10^{-3} cm/s for d-QC). Thus, the β_{diff} is always

greater than β_s in the range of our crystal size. It follows that diffusion is relatively fast (for the crystal sizes so-investigated) and hence interfacial attachment is the rate determining step in crystallization. It can be noted that the same conclusion was drawn for the case of d-QCs in the aperiodic plane, see **Ch. 4**, on the basis that all bounding {10000} facets have the same velocity irrespective of their physical orientation and are therefore limited by their own intrinsic mobility (as represented by the quantity β_s).

To study the growth kinetics of X phase based on **Eq. 4.1**, we require the growth velocity and supersaturation. Both phases have *nearly* isotropic growth rates in the planes perpendicular to the `long axis'. In extracting parameters (i) and (ii) from our real-time X-ray imaging data, we must consider carefully the consequence of a relatively high nucleation rate: namely, crystals that grow in close proximity to one another must `compete' for the available solute and thus growth may stagnate as it becomes solute limited. That is, the neighboring crystals act as solute sinks and can dramatically lower the nearby supersaturation. As an example, low facet velocities [indicated by light-blue colors in **Fig. 5.4(a)** are found where the diffusional fields of neighboring crystals overlap. As the crystals grow, Al is rejected into the melt, accumulating in the open spaces between the crystals. Such solutal interactions have been seen to deactivate the growth of equiaxed grains in metal castings [142]. For this reason, and to determine the *unbiased* facet velocity, we isolate a freely growing crystal (red dashed box in **Figs. 5.4(a,b))** that has less of an interaction with other crystals and also enough space to grow further. In addition, we are able to retrieve the instantaneous composition of the bulk liquid $\langle c^{L}_{Co,Ni} \rangle$(t) directly from our X-ray projection images, and the equilibrium liquidus composition $c^{L,equil}_{Co,Ni}$(t) from recent thermodynamic assessments of the Al–Co–Ni system [108].

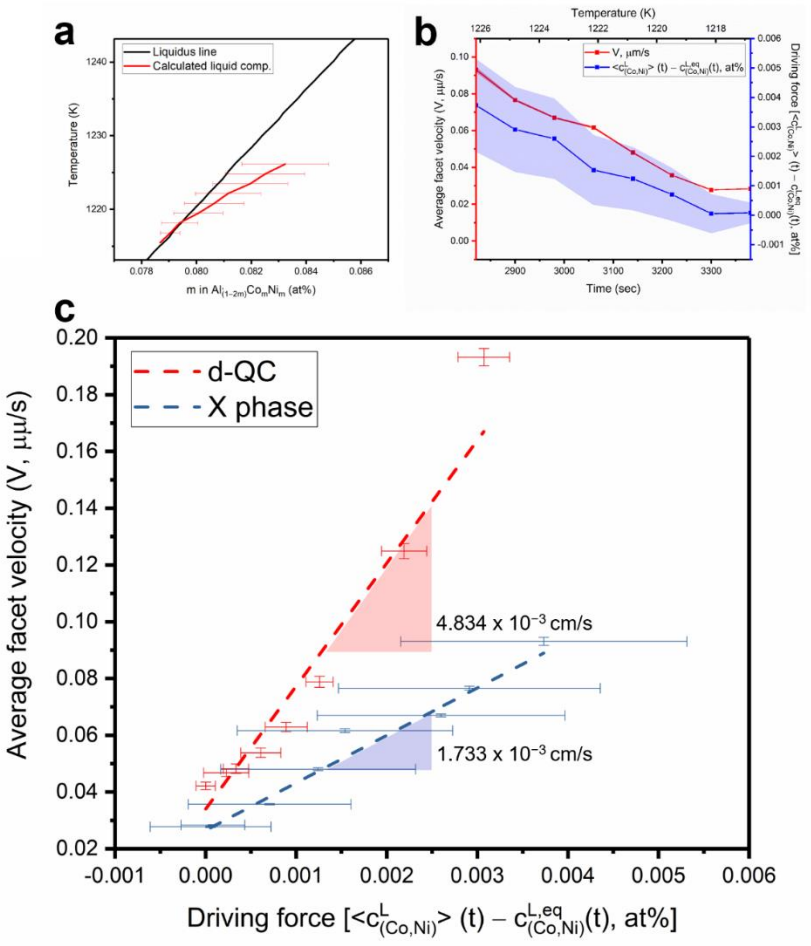

Fig. 5.5. (a) Calculated liquid composition ($< c^{L}_{Co,\,Ni} >$, in red) during XRT experiment, superimposed on a portion of the pseudobinary $Al_{1-2m}Co_mNi_m$ phase diagram ($0.074 \leq m \leq 0.088$) that shows the equilibrium liquidus curve ($c^{L,equil}_{Co,\,Ni}$, in black). Errors in the calculation of the former are due to slight differences in the sample thickness between independent measurements, which in turn may influence the intensity I of the forward attenuated beam (by the Beer-Lambert law, $I \propto e^{-d}$, where d is sample thickness). The horizontal spacing between the red and black curves represents the supersaturation driving force at a given time and temperature. (b) Average facet velocity of a freely-growing X phase crystal (in red, see also **Fig. 5.4(b)**) and supersaturation (in blue), during the growth process. (c) Average facet velocity *vs.* driving force of d-QC and X phase. The slopes give the kinetic coefficient β_s which is associated with the growth process (*i.e.*, **Eq. 4.1** with $n = 1$).

The two compositions are plotted as functions of temperature in Fig. **5.5(a)**. At short times (high temperatures) following crystal nucleation, the difference, $\langle c^{L}_{Co,Ni}\rangle(t) - c^{L,equil}_{Co,Ni}(t)$, is large, indicating that the liquid phase is highly supersaturated in the elements Co and Ni, whereas at long times (low temperatures) this supersaturation decays to near-zero and hence the two composition curves overlap. **Fig. 5.5(b)** indicates that the temporal variations in velocity and supersaturation are compatible with one another during the growth process. By fitting the time-dependent velocity

vs. supersaturation data to a function of the form given by **Eq. 4.1**, we find the kinetic coefficient β_s and the temporal exponent n to be 1.73×10^{-3} cm s^{-1} and 1.0347 for the X phase, respectively (**Fig. 5.5(c)**). An R^2 value of 0.974 was obtained, which indicates a good fit of the model to the experimental data. Therefore, the growth process of the X phase is dominated by the kinetics of interfacial attachment in the regime of weak supersaturation. More specifically, its growth follows *first-order kinetics* ($n \approx 1$) akin to the d-QC (in directions perpendicular to the "long" axis). In addition, we can convert the measured kinetic coefficient in a supersaturated (s) matrix, β_s, to the more widespread kinetic coefficient in an undercooled (m) melt, β_m, by making use of the liquidus slope. The latter parameter represents the interfacial velocity V under unit undercooling ($\Delta T = 1$ K). We find $\beta_m = 4.49 \times 10^{-7}$ cm s^{-1} K^{-1} for the X phase in the {010} plane, *which is five times smaller* than that of the d-QC in the aperiodic {00001} plane ($\beta_m = 2.41 \times 10^{-6}$ cm s^{-1} K^{-1}, see also **Fig. 5.5(c)**).

One might suppose that the difference in the two kinetic coefficients might be due to different growth temperatures (of approximately 32 K, see also **Fig. 5.1**), since β_m is known to have an Arrhenius-type dependence on temperature T,

$$\beta_m \propto \exp\left(-\frac{E_a}{k_B T}\right) \tag{5.2}$$

where E_a is the activation energy for interdiffusion in the melt, and k_B is the Boltzmann constant. For sake of simplicity, and due to the lack of data on multicomponent melts, we assume that the activation energy for interdiffusion in Al-Co-Ni melt is approximately the same as that of self-diffusion in liquid Al, given by 280 ± 70 meV (Kargl *et al.*, 2012). By invoking **Eq. 5.2**, we find that the experimentally determined kinetic coefficient β_m of the X phase (4.49×10^{-7} cm s^{-1} K^{-1}, at its nucleation temperature, 1227.2 K) becomes $4.81 \pm 0.08 \times 10^{-7}$ cm s^{-1} K^{-1} at the nucleation temperature of d-QC (1259.8 K). Thus, our crude calculation shows that the "temperature-corrected" β_m value is almost the same as at lower temperature. Ultimately, the origin of the different kinetic signatures β_m is not a *thermal* one but rather a *configurational* one, as will be explained further in the next section.

5.4 Connection between stability and solidification rate

In general, there are two routes of phase stabilization. One is *kinetic stabilization*, which occurs when crystals are quenched from high temperature to room temperature. During the quenching process, the system does not have sufficient time to overcome the energy barrier for phase transformation into other stable phases; thus kinetically stabilized states can be referred to as *metastable states* [24]. Another route is thermodynamic stabilization, which consists of two components, energy and entropy. If the former holds true, QCs exist as a ground state of matter, and their stability is determined by the heat of formation ΔH at 0 K. Instead, the stability of QCs can be determined by the entropy term $T\Delta S$ in the expression for the Gibbs energy change, ΔG. Topological, chemical and phasonic disorders may all contribute to the entropy of the system [24]. For instance, QCs which have a broad compositional stability range (*e.g.* the d-Al–Co–Ni phase, investigated in this work) can have large entropic contributions from site-occupancy disorder (either topological or chemical). This might explain why the Ni-rich d-Al–Co–Ni is only stable at high temperature (*e.g.* higher phononic and phasonic disorders) [143].

One way that entropy can be readily incorporated during solidification is if clusters attach to the QC growth front at random. As early as the 1990s, models (see, *e.g.*, [144]) have been proposed for the random packing of decagonal clusters with 10-fold symmetry. In this view, the clusters overlap with their neighbors, in the sense that they share atoms with the neighboring clusters (see also **Sec. 1.2**). That is, there are no rules that force clusters into unique arrangements, and hence many possible configurations appear due to the large degrees of freedom on how to join with neighboring clusters. “Errors” or phason strain are inevitably introduced during the growth process. Such defects increase the phason elastic energy, which in turn is reduced through phason flips, as directly observed *in situ via* HRTEM [27]. In contrast, *those same clusters cannot attach to the periodic approximant crystal at random*, requiring instead extensive cluster rearrangements to maintain the translational symmetry of the underlying lattice. For this process, at least short-range diffusion is necessary. In contrast to bulk diffusion (considered in **Sec. 2.2.1**), short-range diffusion occurs over only a few interplanar spacings *within* the solid-liquid interface (and thus the growth process is still interface-controlled). This explains why some metallic liquids have the ability to deeply undercool [145, 146] and, in our case, why the kinetic coefficient of the periodic approximant X phase is about one-fifth of that of the decagonal QC. Even if the different growth

temperatures T between the two phases are accounted for (see above), the kinetic coefficient $\beta_m(T)$ of the periodic approximant is still less than the QC. Further support of this idea comes from molecular simulations of QC growth by Ref. [147]. The team showed (in the case of a dodecagonal, one-component QC) that it "traps" icosahedral clusters in the liquid phase with minimal rearrangement; for this reason, the structurally more flexible QC can grow more rapidly than its periodic σ-phase approximant, whose formation would require more extensive local rearrangements (Keys & Glotzer, 2007). Thus, despite having similar structural motifs (**Sec. 1.4**), *the two phases can have very different kinetic signatures.*

That the QC more readily incorporates atomic clusters – pre-existing in the liquid phase – would imply a greater interface width than that of the X phase. Indeed, synchrotron-based X-ray diffraction studies on electrostatically levitated metal droplets point to a diffuse interface that effectively `blurs' the distinction between solid QC and liquid [148]. According to the simple model of Tang & Harrowell [149], the growth normal velocity V is related to this interface width W as $V = uW$, where u is the fixed rate at which order increases at any point in the interface. Given the same supersaturation driving force, and holding all else constant, our results would indicate that the interface width of the X phase is five times smaller than that of the QC, thus producing a slower growth rate.

Chapter 6. Kinetic and Equilibrium Shapes of an Icosahedral Quasicrystal

In the thirty years since Shechtman's discovery, there have been great strides in determining the shapes of QCs. For instance, Ho *et al.* [150] used a lattice model with short range atomic interactions to conclude that the *equilibrium shape* (ES), bounded by low energy planes, of i-QCs could not be the pentagonal dodecahedron, although they stated that this shape could exist as a non-equilibrium *growth shape* (GS), bounded by the slowest growing orientations. Ingersent [151] argued that by employing a generic lattice model based on both attractive and repulsive atomic interactions, several shapes including the pentagonal dodecahedron could indeed represent the ES of i-QCs. However, Ingersent's lattice model is likely unrealistic for QCs because the variability in their local atomic configurations renders any next nearest neighbor interactions unphysical [151]. On the experimental side, the vast majority of studies have inferred the ES from observations of faceted micro-voids, quenched specimens, and projection X-ray images. In particular, Beeli *et al.* [152, 153] investigated the morphology of micro-voids in i-QCs and suggested that their highly faceted shape could be a good indication of the ES in these systems. They found that voids tend to adopt the {4, 6, 10} Archimedean polyhedral shape, suggesting a nearly isotropic interfacial free energy [153]. These micro-voids are bounded by a liquid-gas interface, and thus the kinetic processes might not be representative of those occurring along the liquid-solid interfaces encountered in QC solidification. Another approach of determining the ES is through *post mortem* techniques, yet this too is somewhat unreliable due to the continued crystal growth that occurs during the quenching process. This sustained growth during quenching and the fact that the i-QC phase is sometimes only stable at higher temperatures, make it difficult to replicate the equilibrium structure of i-QCs at room temperature. To circumvent these issues, several groups [78-80] have analyzed the growth dynamics of i-QCs *via in situ* X-ray radiography. While X-ray radiography is a powerful tool for dynamic studies, growth models developed for i-QCs are based on 3D structures which may render such 2D techniques unreliable. Thus, the *in situ* and 3D observation of the GS and ES in i-QCs is lacking and warrants further investigation.

6.1. Growth shape and equilibrium shapes of an icosahedral quasicrystal

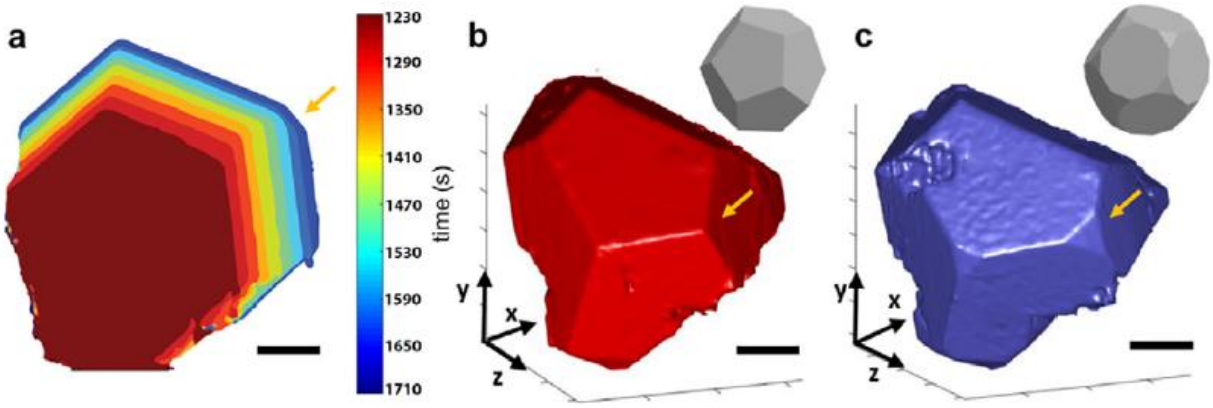

Fig. 6.1. (a) Two-dimensional isochrones of a solid Al-Pd-Mn i-QC in the x-z plane during solidification, where color indicates the passage of time. The corresponding temperatures are as follows from the red isochrone to blue isochrone: 894.5 °C, 893.5 °C, 892.5 °C, 891.5 °C, 890.5 °C, 889.5 °C, 888.5 °C, 887.5 °C, and 886.5 °C. (b) 3D renderings of the i-QC at an early stage of growth (approx. 420 s following nucleation); the growth shape corresponds to a pentagonal dodecahedron (see inset schematic). (c) 3D rendering after growth has nearly commenced (approx. 720 s following nucleation), wherein interfacial velocities are near-zero; the equilibrium shape corresponds to a truncated dodecahedron (inset). All scale bars are 100 μm.

The growth evolution of the i-QC as a function of time is shown by the reconstructed, 2D interfacial isochrones in **Fig. 6.1(a)**. The growth process occurs for ~ 600 s until the supersaturation is nearly relieved, *i.e.*, the composition of the liquid phase reaches that of the liquidus. During this growth regime – wherein the interfacial velocity is greater than zero, as indicated by the large spacing between the isochrones in **Fig. 6.1(a)** – we observe a highly facetted pentagonal dodecahedron. This is the growth shape of the AlPdMn i-QC as shown in **Fig. 6.1(b)** with six visible facets in the field of view. For comparison, an ideal pentagonal dodecahedral shape is shown inset. While the ideal shape has a total of 12 facets, only six are visible in our work since the QC grows outward from the oxide skin of the sample.

During the transition from growth to equilibrium, the pointed vertices in the pentagonal dodecahedron are gradually truncated (see arrows in **Fig. 6.1**) to form the truncated dodecahedron. Smaller, three-fold facets are now apparent at later stage of cooling. This shape is represented by the t{5, 3} Schläfli symbol and is a {10, 3} Archimedian polyhedron. The ideal truncated dodecahedron is shown inset. We note that the truncated dodecahedron shown in **Fig. 6.1(c)** is the near equilibrium shape of the i-QC phase due to the fact that the interface velocities are nearly zero (**Fig. 6.2(a)**), and also the facet area fractions are invariant in time (**Figs. 6.2(b,c)**). Both of these

trends are quantified explicitly and presented below. Porosity is responsible for the rough interface at the top-left of **Fig. 6.1(c)**, consistent with that observed in previous studies [154, 155].

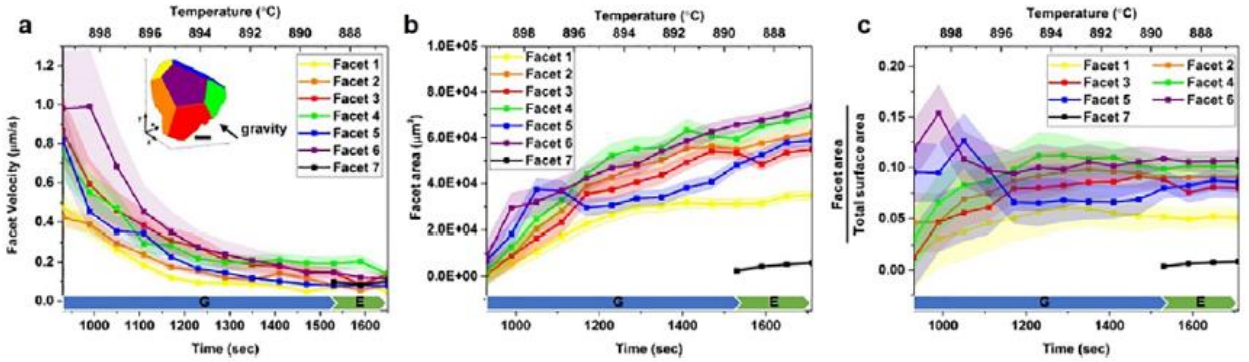

Fig. 6.2. Facet velocities (a), areas (b), and area fractions (c), as function of time. The time axis is divided into growth "G" and equilibrium "E" regimes, for reasons that are discussed in the text. The six facets visible are color-coded according to the dodecahedron inset in (a). "Facet 7" represents three-fold facets of the near-equilibrium shape. Gravity points into the page with the purple facet perpendicular to the gravitational field. Inset scale-bar in (a) measures 100 μm. Error bars represent standard deviations in the velocity and area of patches of solid-liquid interfaces.

Fig. **6.2(a)** shows the evolution of the six facet velocities as a function of time. The mesh triangle velocities do not vary considerably across the facet surfaces, and thus the *triangle* velocities are approximately equivalent to the *facet* velocities. Furthermore, interfacial velocities tend to be relatively small during slow cooling, and therefore we do not see any morphological instabilities at the growth front, *e.g.*, dendrites [156] (contrast this with what we report for icosahedral grains in **Ch. 8**). The plotted velocities tend to decay over time due to the depletion of solute in the liquid phase as the QC grows, varying from as high as ~1±0.25μm/s following nucleation (930s) to near-zero near-equilibrium (1600s). We define the onset of near-equilibrium as the time at which the three-fold facets appear, coinciding with the onset of near-zero growth rates. Errors in the measurement of interfacial velocities at the earliest two to three time-steps arise from the fact that QC growth occurs faster than the experimental resolution. However, as growth slows over time the image quality improves and hence errors are not as pronounced. Other sources of error include small segmentation errors and mesh smoothing.

We have also plotted the facet areas as a function of time in Fig. **6.2(b)**. While most facet areas increase during continuous cooling, a few facets (*e.g.*, blue) decrease in area to make way for the three-fold facet of the truncated dodecahedron that forms during the structural relaxation of the i-QC. Nevertheless, the general trend during growth is a gradual increase in surface area as

a function of time (and temperature). In the *ideal* scenario without any thermosolutal convection or geometric constraint (as will be explained below), one would expect equal facet areas, yet this is not the case here. **Fig 6.2(c)** shows the ratio of facet area to the total surface area as a function of time. The area fractions asymptotically tend to constant values at long annealing times (1500s and beyond).

The theory of the crystal GS is based on the fact that the largest facets are those with the lowest velocity. However, in **Fig. 6.2(a)**, we observe that the slowest growing facet (yellow) also has the smallest facet area (**Fig. 6.2(b)**). This discrepancy may be resolved by noting that this facet grows very close to the edge of the sample holder, and hence it quickly comes into contact with the sample edge (Al_2O_3 skin) that inhibits further expansion of the facet. This geometric effect keeps the facet velocity low despite the small facet area. The yellow facet can thus only increase in area if its neighboring facets (colored orange, blue, and purple) grow outward; however, growth rates at the orange and blue facets are also low due to limited transport of solute. Geometric confinements only affect the relative areas of the facets in contact with the oxide skin. Nevertheless, we still observe a few facets that grow freely into the melt (*e.g.*, purple facet, throughout the experiment), and it is these facets from which we extrapolate the crystal GS.

True ESs are notoriously difficult to measure experimentally, as their observation requires stable phase coexistence and time [157]. At equilibrium, the chemical potential of the solid phase is equal to that of the liquid phase, resulting in a net zero interfacial velocity. Importantly, we never reach absolute *zero* velocity because the near-equilibrium QC must keep up with the imposed cooling rate. Nevertheless, we report near-constant area fractions of each facet at long annealing times (**Fig. 6.2(c)**) indicating morphological self-similarity [95] and that near-ESs may have been achieved. A similar procedure was used in other studies [158] to deduce the ES of plate-shaped precipitates undergoing Ostwald ripening.

6.2. Comparison to theory

Ultimately, we observe a marked difference in the GS and near-ES of the i-QC. The transformation from GS to ES can be thought of as a relaxation mechanism upon which the crystallization driving force (*i.e.*, supersaturation) is removed, as mentioned above. On the atomic scale, this relaxation occurs because the clusters at the vertices of the pentagonal dodecahedron

are loosely bound to those in the bulk. Hence, the clusters are in a thermodynamically unstable configuration and dissolve readily, leaving a three-fold facet (*i.e.*, {011001}) behind. Based on these findings, we propose that that truncated dodecahedral shape is the near-equilibrium shape of the icosahedral $Al_{71}Pd_{19}Mn_{10}$ QC. Finally, our findings are in excellent agreement with the theoretical prediction made by Ho *et al*. [150], that the pentagonal dodecahedron cannot be the equilibrium shape of i-QCs, despite conflicting reports from other authors [151, 153]. However, such shapes can indeed be realized during growth [150]. The three-fold facets may have higher growth rates or lower roughening temperatures [150] as compared to the broad five-fold facets (*i.e.*, {000001}), thus prohibiting their appearance on the crystal GS. Should any smaller facets exist on the ES, they may be below the resolution of XRT.

Chapter 7. Growth Interaction of Quasicrystals

In the previous chapters we investigated the growth of a single QC, either decagonal or icosahedral. That said, high nucleation rates typical of casting lead to the mutual interference between crystals or grains and ultimately, the formation of grain boundaries. For the case of QCs, it is not straightforward to predict when grain boundaries will be formed due to the fact that QCs are incommensurate. In this chapter, we report the formation of a single decagonal QC arising from a hard collision between multiple quasicrystals in a liquid. Through corresponding molecular dynamics simulations, we explore the preconditions required for quasicrystal coalescence, with attention to the effects of initial misorientation between the growing quasicrystalline grains on the formation of grain boundaries. The experimental study and image processing-based analysis were conducted by myself while the molecular dynamic simulations and bond angle analysis were performed by Ms. Kelly Wang (University of Michigan).

7.1. Growth of single quasicrystals by solidification route

Despite their unique anti-corrosive, thermal, electric and frictional properties [159-161], the practical application of QCs is limited due to the difficulties in forming a defect-free, large-dimensional grain. Conventionally, researchers used the following techniques to grow a single crystal: Bridgman, Czochralski, floating zone and self-flux methods [162]. These methods will be briefly reviewed here. The *Czochralski method* uses a small piece of seed crystal and growth occurs atop the seed through incongruent solidification from the molten alloy (*i.e.* solid and melt have different compositions). The growth process requires careful control of the temperature gradient, rotation speed and crystal pulling speed (0.1 – 10 mm/h). In the *Bridgman method*, nucleation occurs spontaneously rather than on a pre-set seed. The sample is kept at high temperature (above the liquidus) for homogenization and then the sample is slowly pulled down across the temperature gradient zone, where crystallization proceeds. The *floating zone method* uses a polycrystalline feed

rod with the same composition as the target crystal. A floating zone (*i.e.* molten zone) is formed in the feed rod by selective heating. As the zone moves upward, crystallization occurs from the bottom to the top of the feed rod. The *self-flux method*, in which crystals are grown by cooling an off-stoichiometric melt below the liquidus temperature does not involve a temperature gradient nor selective heating. After obtaining crystals, the coexisting melt is decanted.

7.2 Growth of single quasicrystals by grain coalescence

In general, it is notoriously difficult to avoid forming a polycrystalline QC without the delicate control of the solidification parameters, as described above. Instead, we consider the possibility of producing single QCs *via* grain coalescence. Somewhat surprisingly, Schmiedeberg *et al*. [163] reported through phase field crystal simulations that coalescence occurs more readily in dodecagonal QCs than in periodic crystals, despite the fact that two QC grains are always incommensurate. They speculated that phason strain play a significant role in distributing stress around the non-fitting structures [163], wherein the resulting phason strain can be relaxed via phason flips [17, 21]. In spite of these insights offered by Schmiedeberg *et al*. [163], grain *coalescence* — or the formation of a single, dislocation free crystal from multiple, misoriented grains — has never been demonstrated experimentally, to the best of our knowledge. In addition, their work leaves several questions unanswered on the QC response to internal stresses, owing in part to the limited resolution of the phase field crystal calculations. In this chapter, we will investigate the dynamics of coalescence via joint experiment and simulation approaches, the latter being the work of Ms. Kelly Wang (University of Michigan). Due to the collaborative nature of the project, results from both experiment and simulation will be included here.

More specifically, we unveil the coalescence between thermodynamically-stable decagonal d-QCs [108] upon solidification of an Al-15at%Ni-6at%Co alloy. We harnessed synchrotron-based, four-dimensional XRT to capture the formation sequence of a single d-QC from multiple grains with negligibly small initial misorientation in the aperiodic plane. On the basis of our experimental results, we performed MD simulations to identify the mechanism of grain coalescence (or conversely, grain boundary formation) at the atomic scale. We examine relevant crystal rotation mechanisms [164-168] and discuss the role of phasons in facilitating the process. Our combined efforts provide the first direct evidence of the self-healing nature of incommensurate structures, such as QCs.

7.3. Experimental studies of grain coalescence

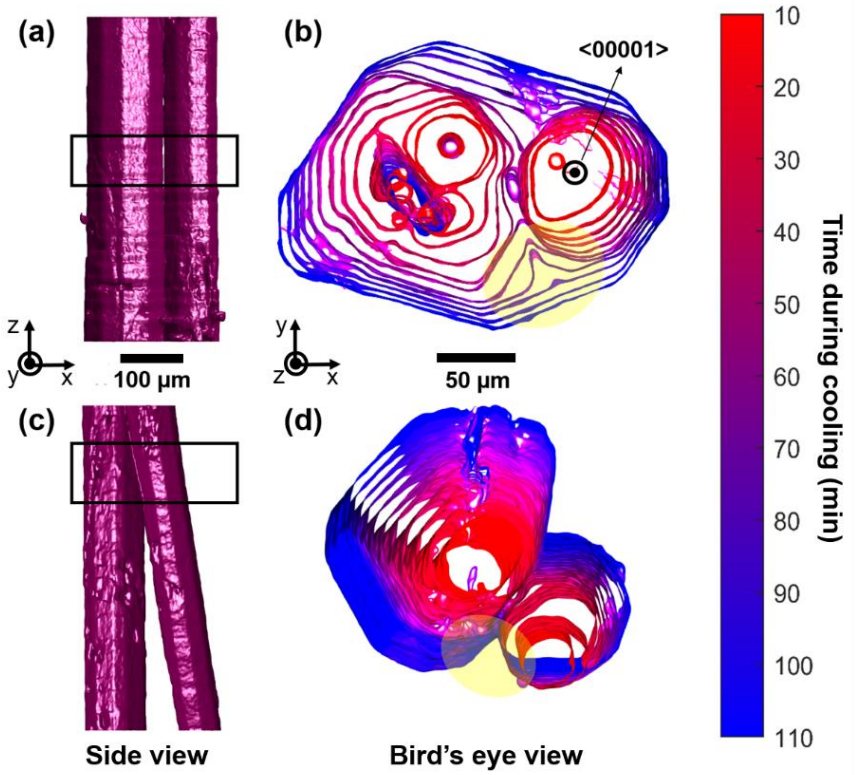

Fig. 7.1. Tracking grain impingements in real-time. (a) Side view (z − x in the specimen frame) of two d-QCs with parallel {00001} long axes, observed after 50 min of cooling (1 °C/min) from 1020 °C. (b) Birds-eye view (x − y) of quasiperiodic plane corresponding to boxed region shown in (a). (c) Side view of d-QCs with non-parallel {00001} long axes, observed at the same timestep as in (a). (d) Birds-eye view of the boxed region shown in (c). Isochrones of the solid-liquid interface in (b) and (d) are colored to illustrate the passage of time, with early times in red and late times in blue. Times taken after cooling and temperatures in (b) and (d) are as follows: 10 min (1010 °C), 20 min (1000 °C), 30 min (990 °C), 40 min (980 °C), 50 min (970 °C), 60 min (960 °C), 70 min (950 °C), 80 min (940 °C), 90 min (930 °C), 100 min (920 °C) and 110 min (910 °C). Yellow regions in (b) and (d) highlight the evolution of the grain boundary groove in time.

Fig. 7.1 depicts the time-evolution of multiple d-QCs before and after collisions in an alloy of composition Al-15at%Ni-6at%Co, upon slow cooling (1°C/min) from above the liquidus (~1026 °C) to below. The growth sequences of the d-QCs were recorded via XRT every 10 mins starting from 1020 °C (at which point the sample was in a fully liquid state) with 20 s of temporal resolution. The key advantage of using XRT is that we can unambiguously visualize the morphologies, misorientations, and growth dynamics of the QCs in real-time and in 3D, without needing to repeatedly quench our specimen. As mentioned previously, quenching is known to

distort the shapes and orientations of the solid-liquid interfaces [169]. Worth noting is that we confirmed the existence of d-QCs in our sample through X-ray diffraction (**Fig. 7.2**) together with a thermodynamic assessment of the Al-Co-Ni system [108].

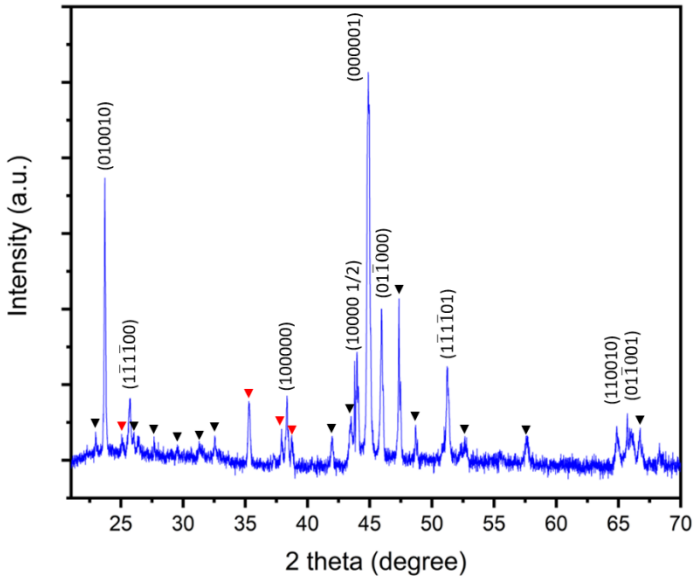

Fig. 7.2. X-ray diffraction pattern of water-quenched $Al_{79}Co_6Ni_{15}$ alloy from an initial temperature of 970 °C. Rapid quenching prevents peritectic decomposition of d-QCs (*i.e.*, $L + QC \rightarrow Al_3Ni_1$). Diffraction peaks from d-QCs are indexed accordingly. The peaks marked with black and red symbols correspond to the Al_3Ni_1 and aluminum oxide, respectively.

The d-QCs in **Fig. 7.1** show a decaprismatic morphology [2] with a `long axis' parallel to <00001>, representing the fast-growing periodic direction. Perpendicular to this direction is the aperiodic plane {00001}. Similar to our past experiments in **Ch. 4**, the d-QCs are `anchored' to the oxide skin of the sample (not pictured), which acts as a heterogeneous nucleant for the d-QCs. As they grow, the d-QCs interact with each other through soft and hard collisions.

We selectively focus on two different cases of hard collisions between d-QCs with (i) parallel long axes (**Figs. 7.1(a,b)**) and (ii) non-parallel long axes **(Figs. 7.1(c,d))**. **Figs. 7.1(a,c)** show these two cases after 50 min of continuous cooling from a viewpoint perpendicular to the long axes of the d-QCs. **Figs. 7.1(b,d)** display a bird's eye (or cross-sectional) view of the growth sequences from the quasiperiodic planes. When the long axes of d-QCs are parallel (**Fig. 7.1(b)**), we observe multiple coalescence events, the first between 20-30 min and the second between 50-60 min, the culmination of which is the formation of a single d-QC. The latter statement can be proved by the absence of a grain boundary groove (where the grain boundary intersects the solid-liquid

interfaces) [170, 171] as well as the presence of around ten facet planes on the coalesced structure at the final time-steps. If the grain boundary groove persists during solidification, it can be inferred that the grain boundary is stable and fixed to the groove [172]. However, the morphological transition from a V-shaped groove to a faceted interface (**Fig. 7.1(b)**), highlighted in yellow) suggests otherwise, *i.e.*, the annihilation of the grain boundary during grain coalescence. Interestingly, the facet orientations of the d-QCs prior to impingement were nearly the same as those d-QCs following coalescence. This observation is in line with the findings of Schmiedeberg *et al.* [163] who testify to the coalescence between two colloidal QCs with small initial misorientation in the aperiodic plane regardless of the initial distance between them. Our quantitative analysis of facet orientations can be found in **Fig. 7.3** which shows that the initial facets orientations of the two seeds and coalesced QC's facet orientation align well, approximately less than 1°. The irregular shape of the d-QC on the left-hand-side in **Fig. 7.1(b)** between 40-50 min of cooling (*i.e.*, prior to collision) can be attributed to a mutual interference of diffusion fields between the two grains (soft collisions, prior to impingement).

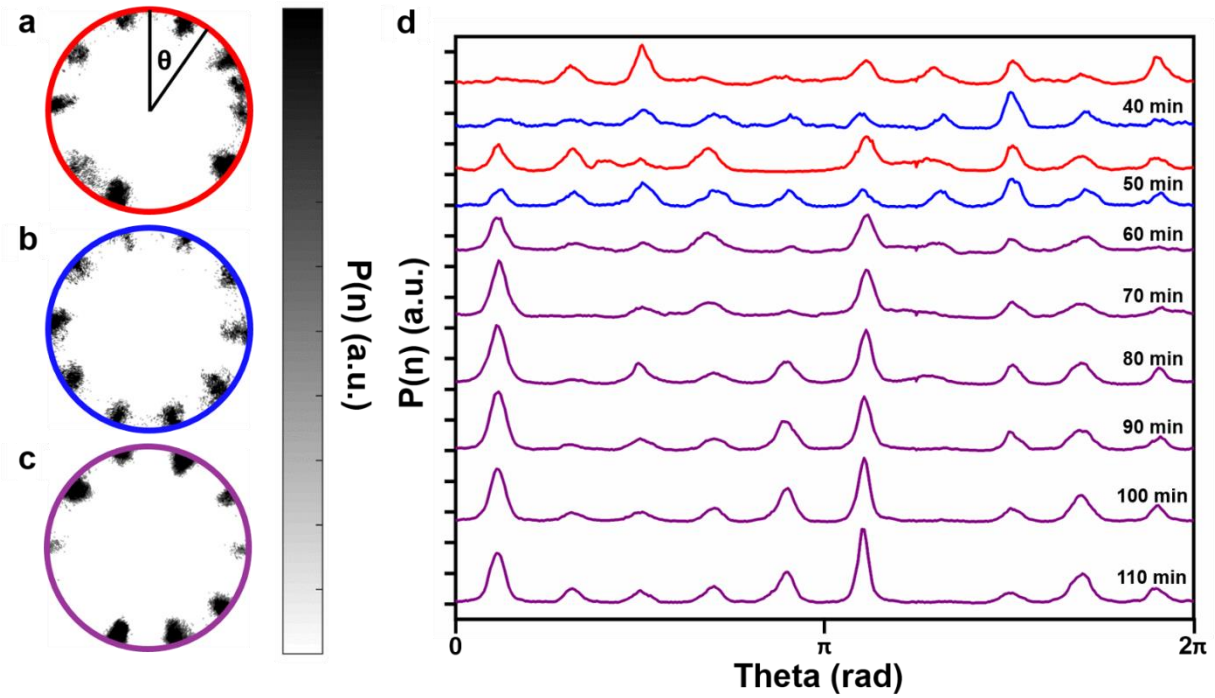

Fig. 7.3. Stereographic projections of interface (facet) normal distributions of d-QC seeds on the (a) left-hand-side, (b) right-hand-side in Fig.1(b) after 50 min of cooling and (c) the coalesced d-QC after 110 min of cooling. Zone axis of projections is <00001> in all cases. Consequently, the QCs in (a,b) possess parallel long axes and small (<1°) misorientation in the aperiodic plane. $P(n)$ represents the probability (weighted by area fraction) of finding an interfacial normal along a particular direction. Peaks in the distribution indicate a highly anisotropic or faceted structure. In principle, a facet should have a single (discrete) orientation, yet the peaks have finite width here. This is likely a result of mesh smoothing. (d) Radial distribution of facet orientations obtained from 40 min to 110 min. The red, blue, and purple colors represent the d-QC seeds on left- and right-hand-side (before impingement) and the coalesced d-QC, respectively. Angular measurements start at the 12 o'clock position of the stereographic projection (see (a)) and increase clockwise. Two facets (peaks) are separated by an angle of nearly 36 degrees, which is consistent with a decaprismatic morphology of the d-QC phase.

On the other hand, in the case where the two long axes are non-parallel to each other, we observe the persistence of a V-shaped grain boundary groove (**Figs. 7.1(c,d)**), signifying the formation of a stable GB between the two grains. In comparison to the above scenario where the long axes were parallel, here the quasiperiodic lattice in one d-QC merged with the periodic lattice of the other d-QC. Naturally, the appreciable disregistry between the two lattices resulted in the formation of a grain boundary, and hence a V-shaped groove (**Fig. 7.1(d)**). Since contrast in XRT stems from differences in photoabsorption between the phases, we can only capture the external solid-liquid interfaces and not the grain boundaries embedded within the solid phases. Thus, we turn to MD simulations to `see' inside the evolving d-QCs and fill in the spatiotemporal gaps from our experiment.

7.4. Molecular dynamics studies of grain coalescence

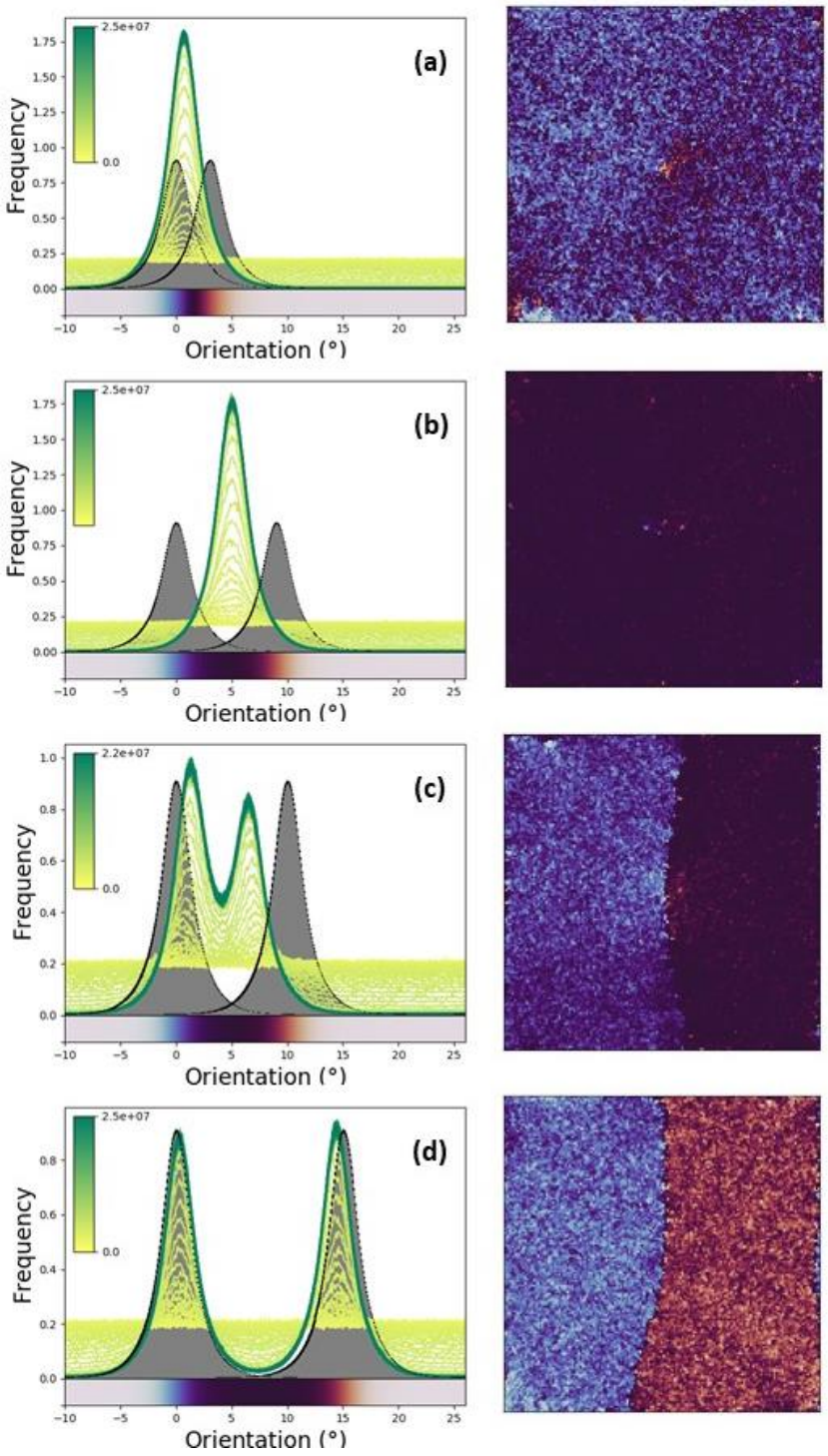

Fig. 7.4. Changes in particle orientation (θ) toward near-equilibrium configurations (~25 million simulation timesteps) are shown. Left: Histograms of simulated (yellow to green lines) and expected particle orientation (grey peaks). Yellow indicates earlier timesteps while green indicates later timesteps. Grey peaks are expected probability density functions (PDF) for the reference grain (θ = 0°) and rotated grain. PDFs are calculated from single-seeded simulations. Peaks for the reference seed are centered at θ = 0°

and peaks for the rotated seed are centered at θ = (a) 3°, (b) 9°, (c) 10°, and (d) 15°, respectively. Right: Spatially-binned simulation frames at 25 million timesteps for each set of seeds. Scale bars for local orientation are below each histogram (left) and correspond to the orientation in the histogram axes, where bright blue corresponds to particles that align with the reference seed (θ = 0°). Bright orange corresponds to particles that align with the rotated seed, where θ = (a) 3°, (b) 9°, (c) 10°, and (d) 15°. Black area corresponds to angles along the shortest arc between 0° and the rotated seed and white area corresponds to angles along the longest arc between 0° and the rotated seed.

We systematically examine the effects of misorientation on grain behavior in d-QCs using seeded MD simulations with an isotropic, single-component pair potential previously shown to form d-QCs [173]. We focus on misorientations within the aperiodic plane {00001}, since the XRT experiments provide evidence for coalescence when the long axes are parallel (**Fig. 7.1(a,b)**). Thus, we carry out MD simulations in quasi-2D boxes to maximize motion in the quasiperiodic plane and minimize motion along the periodic axis. We fix the initial position of seeds in our simulations to match experimental conditions, where grains were `anchored' to the sample surfaces. We use the decatic order parameter, ψ_{10}, to identify the local orientation (θ) of a particle with respect to a reference basis for each particle m,

$$\Psi_{10}(m) = \frac{1}{n} \sum_j^n e^{10i\theta_{mj}} \tag{7.1}$$

where n and θ denote the number of neighboring atoms within a given radius and misorientation between the local atomic configuration of a particle and the fixed basis with decatic rotational symmetry. Particles that align with this reference basis will have an orientation of θ = 0°. A detailed description of MD simulation setup and analysis is provided in **Sec. 7.5**.

In order to elucidate the mechanism behind grain coalescence in d-QCs, we begin with characterization of GB formation as a function of misorientation. Here, we define misorientation as the rotation angle about the <00001> axis between two seeds. We define grain as a region where the arrangement of particles may be described by a continuous lattice and seed as a set of particles belonging to the d-QC lattice with fixed orientation. We will refer to simulations based on the misorientations between *seeds*, rather than the misorientations between *grains*, since grains can change orientation over time but the misorientations between seeds are fixed and represent the initial conditions of d-QC grains. **Fig. 7.4** compares small (3°), intermediate (9° and 10°), and large (15°) misorientations between two d-QC seeds with a fixed distance of $L = 40d$, where d is particle diameter. When seed misorientations are 3° and 9° (**Figs. 7.4(a,b)**), we observe unimodal distributions of Ψ_{10} in the bulk QC near-equilibrium (left, histograms). This result

suggests grain coalescence between misoriented seeds. On the other hand, when initial misorientations are 10° and 15° (**Fig. 7.4(c, d)**), we observe bimodal distributions of Ψ_{10} (left, histograms) in the bulk QC near-equilibrium. This result indicates the formation of a grain boundary. That is, grain coalescence between QCs can be observed for relatively low misorientation angles. For intermediate misorientations (θ = 9 - 10°) (**Figs. 7.4(b-c)**), grains tend to rotate toward intermediate orientations. However, grain coalescence is only observed when the orientations of two grains are well-aligned (*e.g.* **Fig. 7.4(b)** at right). At θ = 15°, the grain boundary is clearly defined and orientations of both seeds strongly resemble the initial seed orientations (**Fig. 7.4(d)** at right). The contribution of initial misorientations on the final structure can be also verified by diffraction patterns (**Fig. 7.5**), density fields (**Fig. 7.6**), dislocation (**Fig. 7.7**) and tiling analyses (**Fig. 7.8**). In light of these trends, we can identify a critical misorientation $\Delta\theta_{crit} \approx 9°$ for the given simulation conditions (L = 40d and kT = 0.4), below which grains coalesce. The critical value provided here is not meant to represent all cases of grain coalescence in d-QCs, as $\Delta\theta_{crit}$ is likely a function of various thermophysical parameters (*i.e.* grain size, fluid viscosity, and external stress [164, 165]. Instead, we treat it as a reference point for how the behavior of d-QCs change at $\Delta\theta_{crit}$.

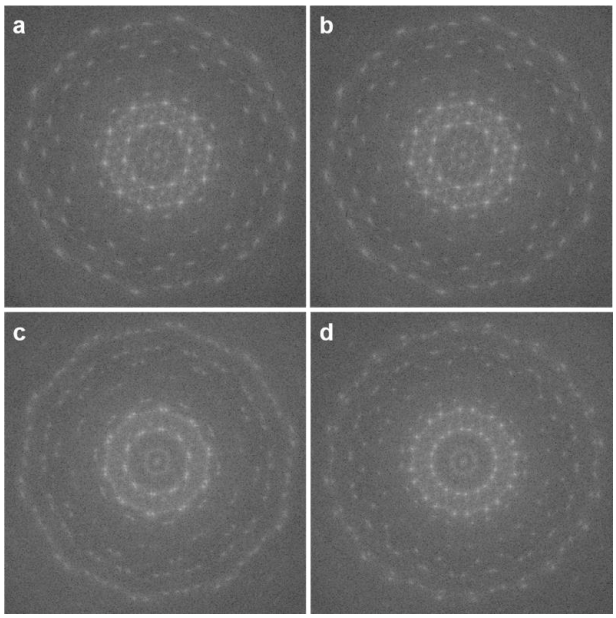

Fig. 7.5. Diffraction patterns of the coalesced structure, when the initial misorientation between two QCs is (a) 3°, (b) 9°, (c) 10° and (d) 15°, respectively. The patterns correspond to the results in **Fig. 7.4**. Note (a) and (b) are indicative of a single d-QC. On the other hand, the diffraction patterns of (c) and (d) suggest the presence of two d-QCs with different orientation. Thus, the diffraction pattern represents the superposition of two single QC patterns. The scattered pattern in (c) reflects the effect of rotation toward the intermediate angle, so that the misorientation between the two ten-fold patterns in (c) is approximately 6°. (d) shows a misorientation of ~15°, which corresponds to the initial misorientation between the seeds.

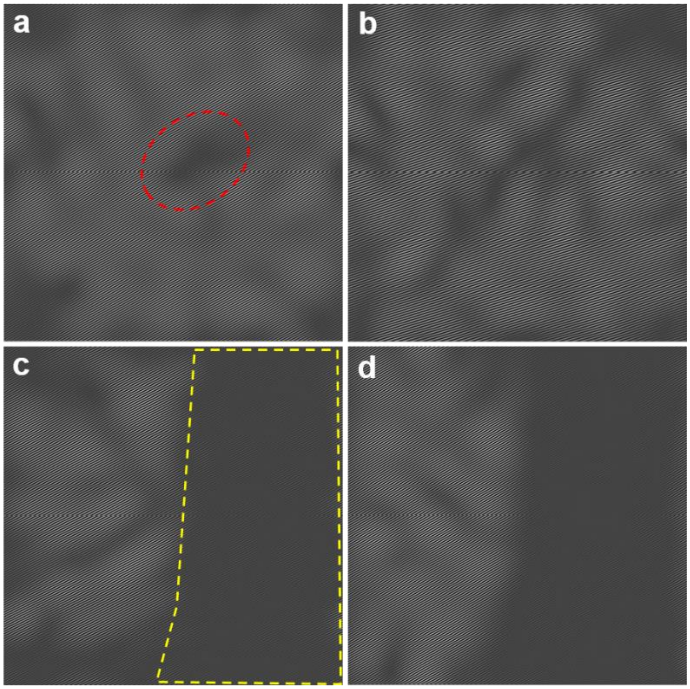

Fig. 7.6. Density modes associated with one pair of Bragg peaks (one basis vector and its negative) for (a) 3°, (b) 9°, (c) 10° and (d) 15° initial misorientations. (a-d) corresponds to the diffraction pattern in **Fig. 7.5(a-d)**. The presence of partially different contrast in (a-d) indicates regions with local phonon strain as highlighted in red in (a). On the other hand, the distinctive contrast in (c,d) is associated with different grain orientations, as highlighted in yellow in (c).

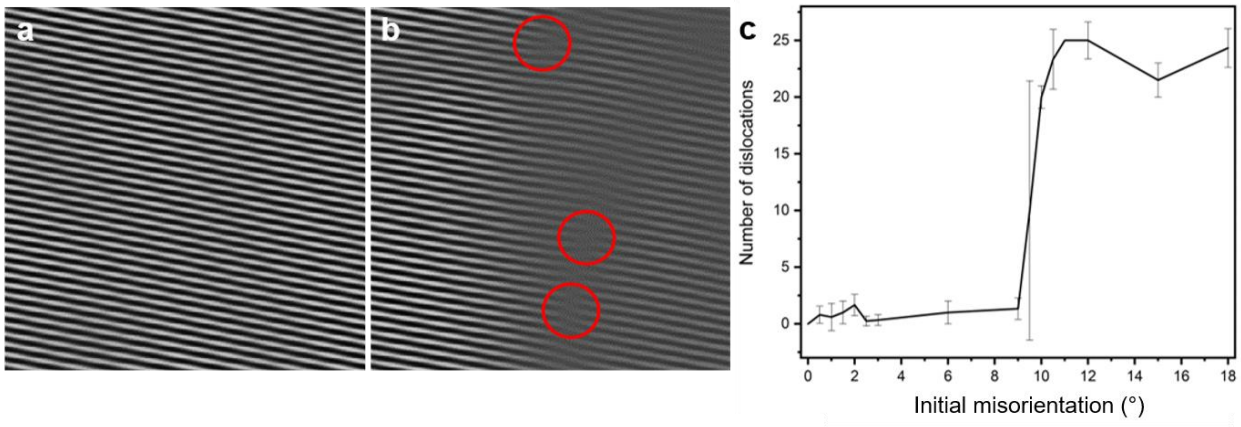

Fig. 7.7. Real-space images of a single density mode [174] when merged QCs reach the last frame in MD simulation (~2.5 × 10^7 simulation timesteps) with (a) 3° and (b) 15° initial misorientations. Dislocations are highlighted with red circles, (a) and (b) are cropped to provide a magnified view from the images that represent full volume. We focus on the region where the two QCs collide. (c) Relationship between the initial misorientation and number of dislocations along the grain boundary in the coalesced structure. We find that there are few dislocations (if any) at low ($\theta < 9.5°$) initial misorientation, since two QCs can rotate toward $\theta = 0°$ (*cf.* (a)). Conversely, there are many dislocations when two QCs cannot minimize the misorientation between them. The error bars were calculated from multiple dislocation analyses to retain consistency of our approach.

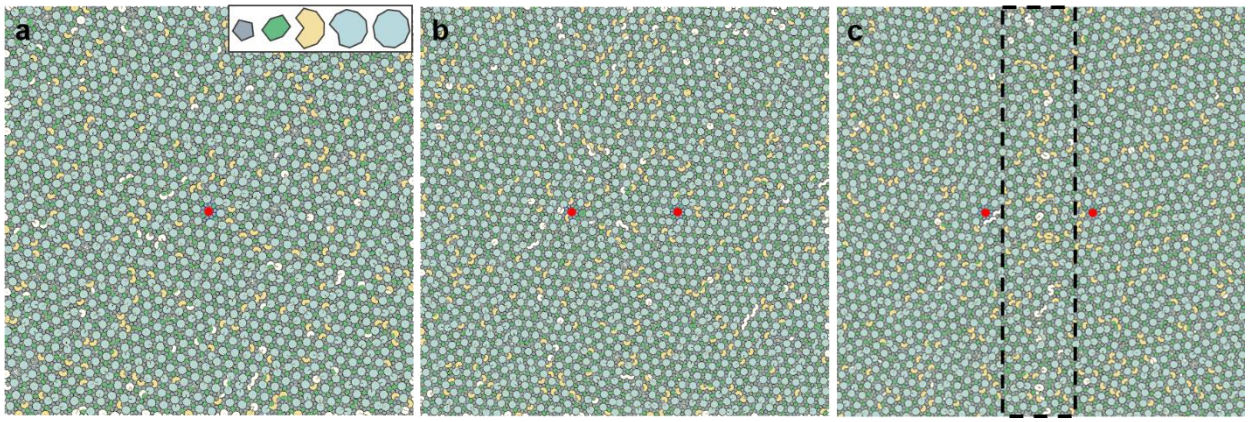

Fig. 7.8. Tiling calculated at the ~2.5×10^7 simulation timesteps of (a) single QC growth, and growth from two QCs with (b) 9° and (c) 18° misorientations. We classified five tiles [175] into four classes (see inset in (a)). From largest to smallest, the four classes are colored in light blue, yellow, green, and grey. The red tiles indicate the initial QC seed positions. Images are cropped from the full volume for better visualization. (a) and (b) demonstrate few, dispersed tiling violations (white regions) that are not assigned to tiles), whereas tiling violations in (c) are concentrated along the grain boundary region (boxed in black). These findings support the formation of a single QC and a grain boundary, respectively.

The phenomenon of grain coalescence is well documented in polycrystalline materials [164, 165, 167]. Grain coalescence is driven by reduction of grain boundary free energy and the mechanisms are categorized broadly by *grain boundary migration* and *grain rotation* (see **Fig**. 7.9).

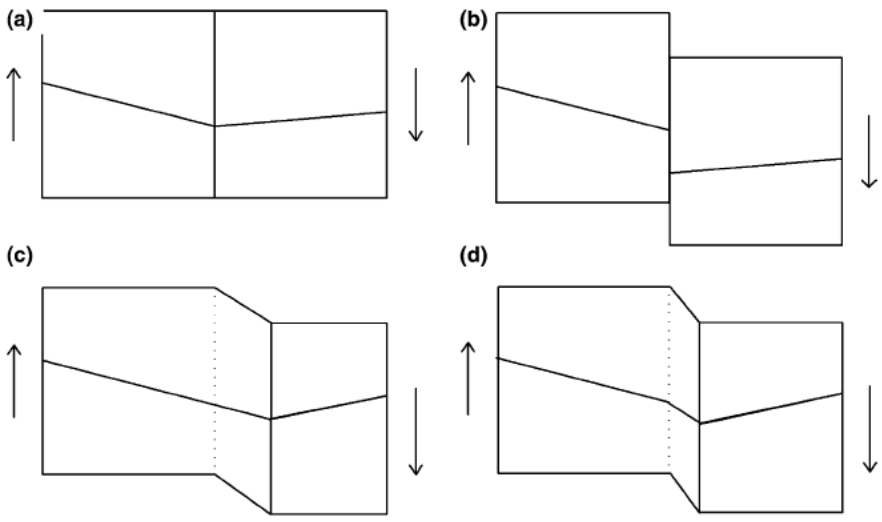

Fig. 7.9. Tangential motion of crystals along planar grain boundary typically occurs in response to an applied stress σ. Elastic distortions are small and not depicted. (a) Original bicrystal, showing grain boundary and the trace of a plane in each crystal. The positions of atoms along this trace is followed in the other parts of this figure. (b) Sliding without interface motion (greased boundary), (c) Coupling of relative tangential translation of crystals with interface normal motion without sliding; direction of interface normal motion determined by the coupling. (d) Coupling and sliding. Reprinted from [164].

Grain boundary migration is typically coupled with rigid sliding [164, 165] (termed coupling), and can result in an increase or decrease in misorientation [168] (**Figs. 7.9(c,d)**). Grain rotation coupled with grain boundary migration may be identified by a translation in the grain boundary and a concomitant, continuous change in misorientation near the grain boundary [164]. On the other hand, uncoupled grain boundary sliding will always result in decreased misorientation [164]. Cahn and Taylor predicted that coupling will occur with high probability, with the exception of special symmetries [164]. Rotation occurs in these cases because the lack of symmetry near the grain boundary results in a biased, net tug on the lattice. In cases where grain boundary dislocations must be conserved, such as with small-angle GBs in periodic systems, grain rotation by pure sliding is prohibited, and coupling-induced rotation dominates [165]. This is because normal motion of the grain boundary ensures dislocations are conserved. Rigid sliding (**Fig. 7.9(b)**) dominates in special symmetries where dislocations can glide along the plane of the grain boundary [164] and grain boundary dislocations can easily annihilate or nucleate [165]. Considering the effects of symmetry on grain coalescence mechanisms, it is reasonable to wonder if the lack of translational symmetry, and the resulting phasons defects, play a role in facilitating grain coalescence in QCs.

We begin our analysis of coalescence by investigating orientation mapping of grain growth from two seeds with misorientation well below $\Delta\theta_{crit}$, *e.g.* 3°, as depicted in **Fig. 7.10**. **Fig. 7.10(a-e)** shows the time evolution of grain orientation for seeds with 3° misorientation. At early timesteps (**Fig. 7.10(a-b)**), we observe two grains (grains A and B) with good alignment to seed orientation (blue and orange regions, seeds A and B, respectively). Immediately after collision, grain A remains well aligned with seed A and a grain boundary is clearly visible (**Fig. 7.10(b)**). Both grains continue to rotate and reduce misorientation (darkening of both grains, **Fig. 7.10(b-e)**).

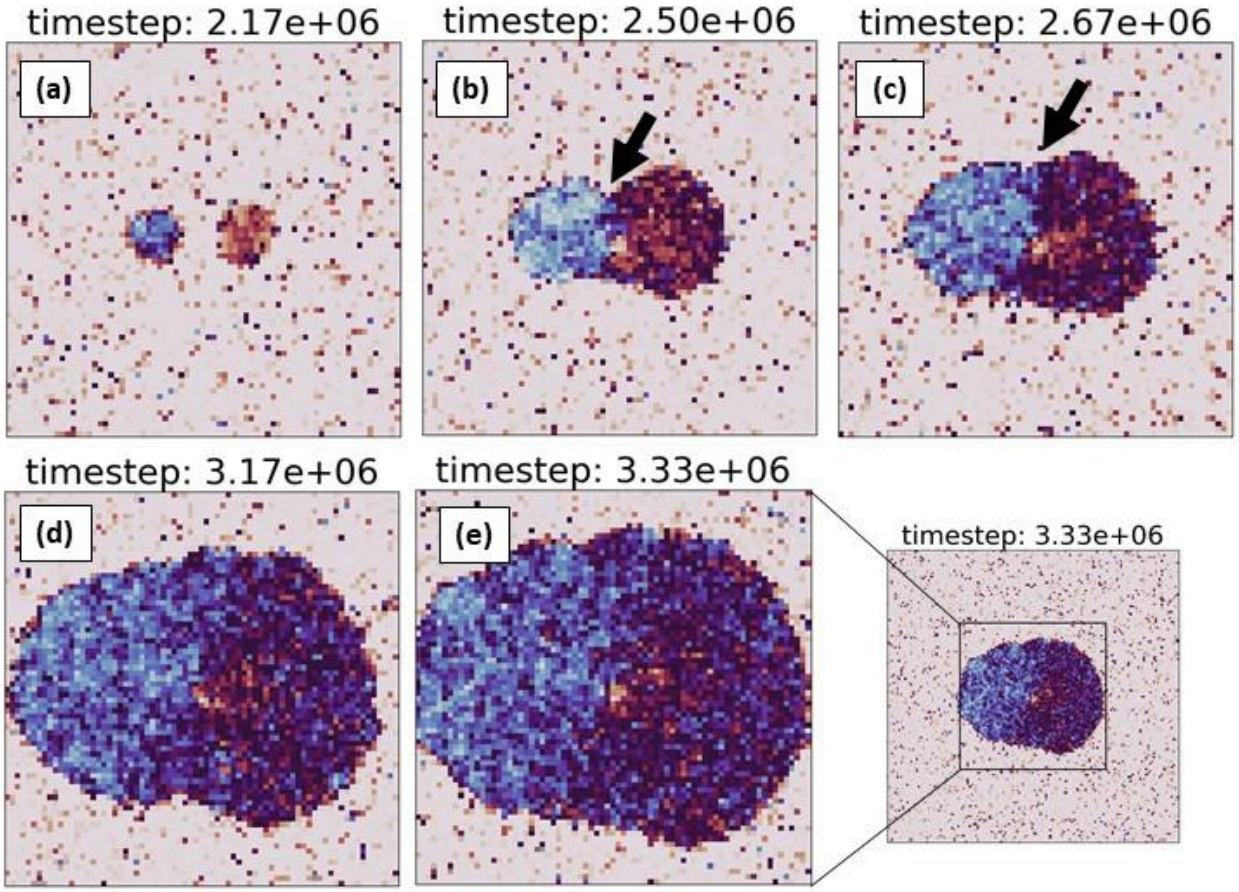

Fig. 7.10. Growth of a single d-QC from two seeds (labeled A and B) with 3° misorientation (a) during early stages of grain growth; (b) immediately after collision; (c) after collision, grain rotation to minimize misorientation; (d) early stages of grain coalescence; (e) after grain coalescence. All heatmaps are cropped according to the inset shown in (e) from the total volume. Subplots (a-e) are colored on the basis of an expected particle seed distribution **Fig. 7.4(a)**. Contiguous regions of white in subplots (a-e) correspond to liquid regions. Arrows in (b-c) point to the GB grooves at the QC-liquid interfaces.

After grain coalescence (**Fig. 7.10(e)**), a gradient between the grains is still visible. However, a unimodal distribution of Ψ_{10} is observed (**Fig. 7.4(a)**) and grain boundary grooves are no longer visible (**Fig. 7.10(e)**). This confirms the formation of a single grain, mimicking the experimental results (**Fig. 7.1(b)**), despite some internal heterogeneity. In contrast, simulations of FCC crystals (**Fig. 7.11**) show clear grain boundary grooves at all stages of growth, even after grain rotation.

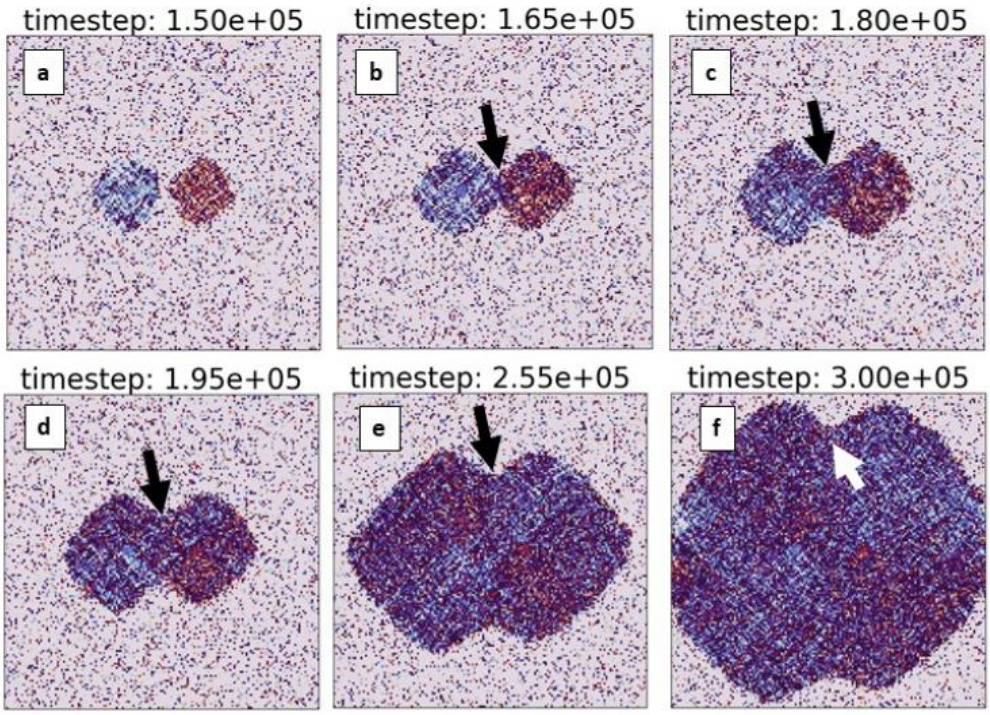

Fig. 7.11. Growth of an FCC crystal with 3° misorientation between seeds at (a) 1.50 × 10^5, (b) 1.65 × 10^5, (c) 1.80 × 10^5, (d) 1.95×10^5, (e) 2.55×10^5, (f) 3.0×10^5 timesteps. Although the uniform color distribution suggests global rotation of misoriented grains toward 0° misorientation, a persistent grain boundary groove (highlighted with arrows) suggests unresolved phonon strain along the grain boundary due to incommensurate distances between FCC lattices.

Our results suggest that grain rotation should be a precondition for grain coalescence in d-QCs for low angle grain boundaries, where changes in the grain boundary shape during growth (**Figs. 7.10(b-d)**) are due to new crystal growth, rather than significant grain boundary motion. Given this evidence, we believe that the sliding model [164, 165] most accurately describes grain coalescence in our system, rather than grain boundary migration. When the rotation occurs by pure sliding, the driving pressure of grain rotation, $P_{||}$, can be expressed as

$$P_{||} \approx -\frac{\gamma'}{R} \tag{7.2}$$

in the absence of applied shear stress. Here γ' denotes the derivative of grain boundary energy as a function of misorientation and R denotes grain size. Assuming that γ is a monotonically increasing function of θ for low misorientation angles ($\theta \rightarrow 0^{\circ}$), γ' is positive so that the grains rotate to reduce the misorientation when the predominant rotation mechanism is grain sliding. In addition, it can be reasonably presumed that rotation does not occur when the misorientation is

greater than $\Delta\theta_{crit}$ because the driving pressure becomes smaller. This is because γ' generally decreases with increasing θ [176].

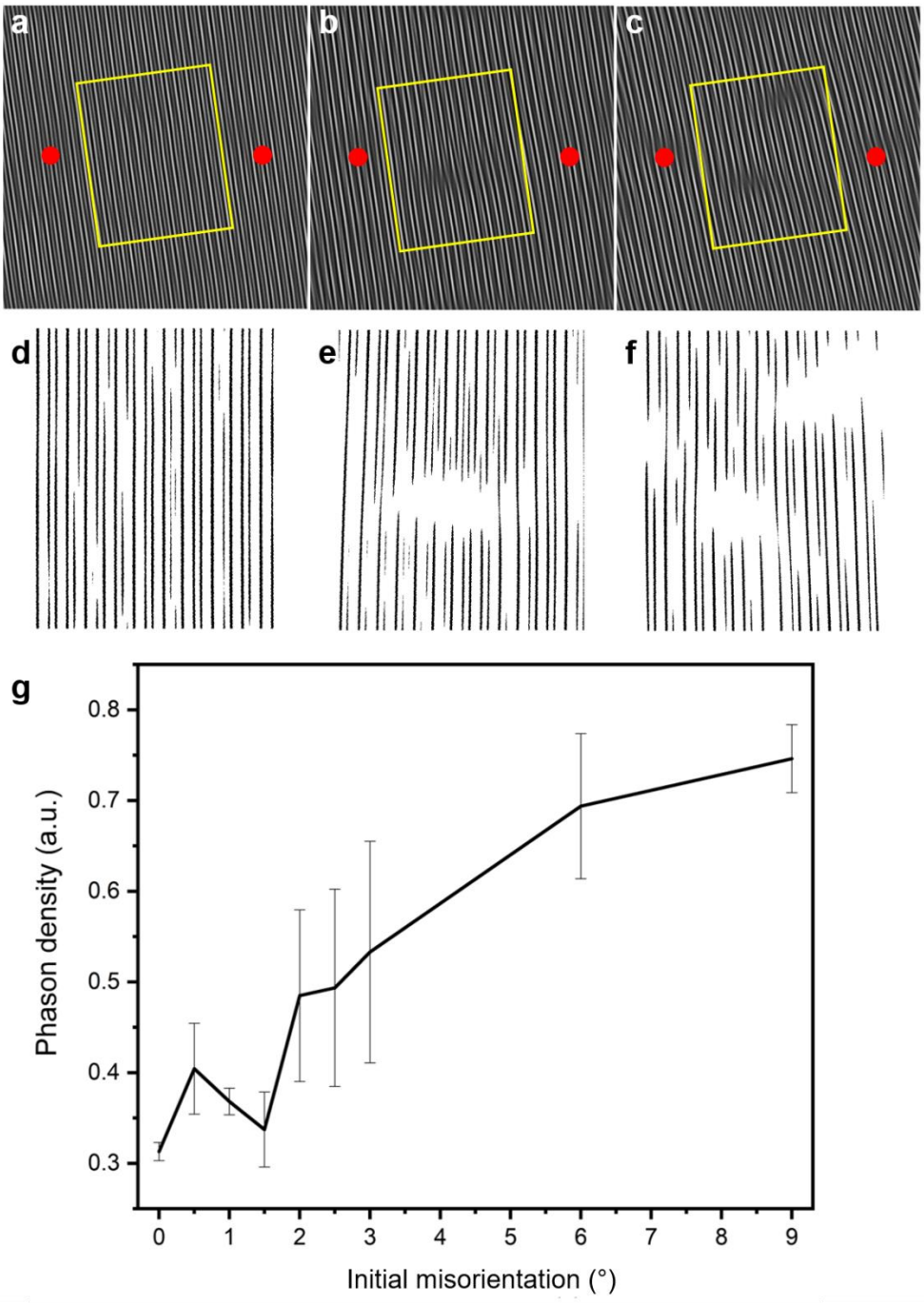

Fig. 7.12. Density modes obtained by filtering two pairs of Bragg peaks from the merged quasicrystals with (a) 0°, (b) 3°, and (c) 9° initial misorientations at timestep 4.0 $\times 10^5$ from the MD simulations. The two pairs of Bragg peaks (*cf.* **Fig.7.6**) represent the two different length scales (long and short) in QCs. The red dots indicate the seed positions. The region boxed in (a-c) with yellow rectangles is segmented for further analysis with an appropriate threshold. (d), (e) and (f) correspond to (a), (b) and (c) respectively. (g) Phason densities calculated as a function of initial misorientation between seeds, using the method introduced by Freedman *et*

al. [177]. The phason density was determined from the segmented images based on the areas inside of the yellow rectangles for misorientations of multiple 0°, 0.5°, 1°, 1.5°, 2°, 2.5°, 3°, 6°, and 9° cases. More specifically, we quantified the fraction of `jags', which is longer than zero and shorter than the longer edge of the yellow rectangles in (a-c), along the direction of the stripes. As the initial misorientation increases, a higher phason strain is accumulated within the grain boundary region. For consistency of our results, we repeated analyses on different MD simulation datasets, which explains the origin of the error bars.

We hypothesize that the absence of perfect dislocations in d-QCs due to noncrystallographic symmetry allows grain coalescence to occur more readily in d-QCs than in periodic crystals. Due to the additional phasonic components in the Burgers vectors, all dislocations in d-QCs are partial dislocations rather than perfect dislocations [21]. It follows that d-QC GBs consist of arrays of partial, rather than complete dislocations. Partial dislocations are shown to be mobile in sheared, 2D d-QCs *via* dislocation glide, which occurs *via* dissociation of dislocation cores and recombination of dislocation dipoles [178]. Motion of partial dislocations through d-QCs results in a wall of phasons along the slip plane [179]. This suggests that the dislocation reactions which enable sliding to occur redistribute the phonon strain from lattice mismatches as phason strain through its dislocation annihilation mechanism. Due to the complexity and variety of dislocations in d-QCs, however, we reserve quantitative analysis of dislocation structures and kinetics for future work. Instead, we examine samples where grain coalescence occurs for residual phason strain as potential signature of partial dislocation motion during grain coalescence (**Fig. 7.12**). Since phason strain relaxation occurs over much longer time scales than our simulations [180], we expect to see residual phason strain at or near regions where the hard collision occurred. Interestingly, **Fig. 7.12** suggests that phason density near the grain boundary increases with initial misorientation, after grain coalescence. We hypothesize that grain sliding introduces phason strain near the GB while grains are rotating and a certain extent of phason strain is still tolerable for the single QC formation below θ_{crit}.

7.5. Details on Molecular dynamics simulations (by Ms. Kelly Wang, University of Michigan)

Molecular dynamics (MD) simulation was performed with HOOMD-blue [181, 182] in the isobaric-isothermal (NPT) ensemble. Simulations used reduced units of energy (ϵ), length (σ), mass (m), and time ($\tau = \sqrt{\frac{m\epsilon}{\sigma^2}}$). Particles interacted through an oscillatory, double-well potential [173], previously shown to form d-QCs. Simulations were carried out in quasi-2D boxes with periodic boundary conditions for 500,000 particles. Quasi-2D boxes, with average final

dimensions of 360 × 360 × 8, were used to reduce the influence of layer mismatches and rearrangements along the periodic axis and to maximize the amount of atomic rearrangements in the quasicrystalline plane. Systems were linearly cooled from a liquid-like configuration (T^*_{init} = 1.5) to a temperature near, but below the melting point (T^*_{end} = 0.4) over 100,000 timesteps. The temperature was expressed in a reduced unit of $T^* = \frac{k_B T}{\epsilon}$ where k_B is the Boltzmann constant. Each system was then held at T^*end for 20 million simulation timesteps at a pressure of 3.9. Simulations consisted of two fixed seeds with a distance of 40 between the seed centers and misorientation between 0° and 18°. For each misorientation, 5-10 simulations were run to ensure consistency of the results.

Chapter 8. Formation of Metastable Dendritic Quasicrystals in the Solid-state

Our recent *in situ* studies (**Ch. 4-7**) have demonstrated that the solidification of QCs and their approximants is governed by the kinetics of interfacial attachment, the anisotropy of which leads to the presence of facets and polyhedral kinetic shapes. These real-time experiments are typically done under near-equilibrium conditions wherein a liquid is cooled slowly below the liquidus, thereby solidifying a thermodynamically-stable phase. However, the growth mechanisms that control the formation of *metastable* QCs remain an enigma. Here, we overcome the challenge in observing the growth of QCs far-from-equilibrium with the aid of dynamic transmission electron microscopy (DTEM). By harnessing DTEM, we provide fresh insights into the growth shapes, growth rates, and growth mechanisms of the metastable QCs, which have a higher degree of phasonic and chemical disorder [183] than ideal QCs [27]. The DTEM experiment was performed with the aid of Dr. Joseph T. McKeown (Lawrence Livermore National Laboratory); structural analysis on the basis of experiment by Dr. Hadi Parsamehr (University of Michigan) and Dr. Ying-Rui Lu (National Synchrotron Radiation Research Center); structural analysis on the basis of MD simulation by Dr. Ling Tang (Zhejiang University of Technology), Dr. Cai-Zhuang Wang, and Dr. Matthew J. Kramer (Ames Laboratory); and finite element analysis by Zhucong Xi (University of Michigan).

8.1. DTEM experiment

8.1.1. Initial condition

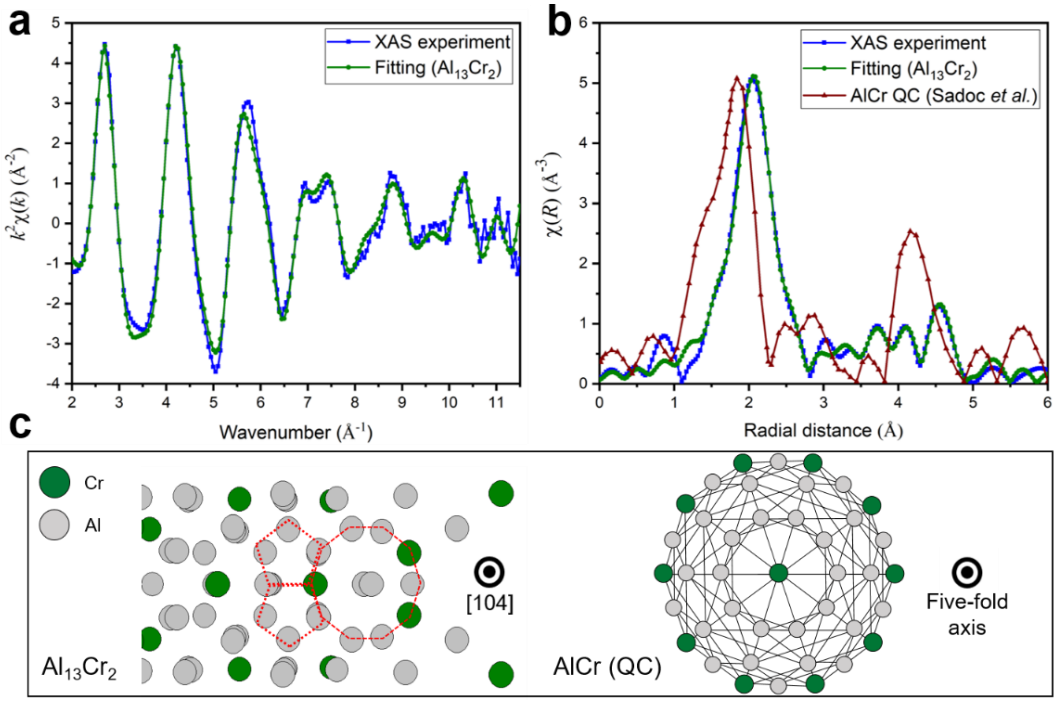

Fig. 8.1. Comparison of local structure measurements, (a) Experimental EXAFS results of the pre-irradiated $Al_{90}Cr_{10}$ film and simulated $Al_{13}Cr_2$ structure in k-space. (b) Radial distribution functions (RDFs) of the annealed $Al_{90}Cr_{10}$ film, simulated $Al_{13}Cr_2$ structure, and Al-Cr icosahedral QC [184]. (c) Schematic illustrations of the approximant $Al_{13}Cr_2$ phase along the [104] direction and a Mackay cluster in Al-Cr icosahedral QC [185]. Unique rotational symmetries, such as five-fold and ten-fold, can be found in both approximant (highlighted in red) and QC structures.

Fig. 8.1(a) presents the extended X-ray absorption find structure (EXAFS) region of the XAS spectrum of the pre-irradiated $Al_{90}Cr_{10}$ film and simulated EXAFS results from the approximant $Al_{13}Cr_2$ structure [42] in k-space. The agreement between the experimental and simulated spectra and radial distribution functions (RDFs, **Fig. 8.1(b)**) indicate that the dominant crystal structure is $Al_{13}Cr_2$ before laser irradiation. However, the RDF of the Al-Cr icosahedral QC [184] shows that the adjacent atomic structures around a Cr atom in the icosahedral QC are more closely packed than the approximant phase. Therefore, the approximant and QC phases have different atomic distance distributions in spite of their structural similarities, see **Fig. 8.1(c)**. Structural similarities are a hallmark of approximant phases of QCs, as described in **Sec. 1.4**. The unit cell of the approximant $Al_{13}Cr_2$ phase consists of three different types of icosahedra and these icosahedra are linked either by sharing vertices, edges, or triangular faces or interlocked at the

center of neighboring icosahedra [42]. Such icosahedral structures are frequently observed in the Al-Cr QCs in the form of Mackay clusters [186]. These clusters are aligned along the five-fold axis of i-QCs and produce a long-range icosahedral order. These structural details affirm the structural similarity between the approximant $Al_{13}Cr_2$ and QC phases, as introduced in **Sec. 1.4**.

8.1.2. Quasicrystal growth from approximant matrix

The microstructural evolution in an $Al_{13}Cr_2$ thin film following laser irradiation was captured via DTEM. The temperature profile of the sample, simulated via COMSOL in **Fig. 8.2**, suggests that the maximum temperature attained is below 600 °C, which is not sufficient to melt the sample (note the liquidus temperature of $Al_{90}Cr_{10}$ is 930 °C). Thus, the ensuing phase transformation occurs entirely in the solid-state.

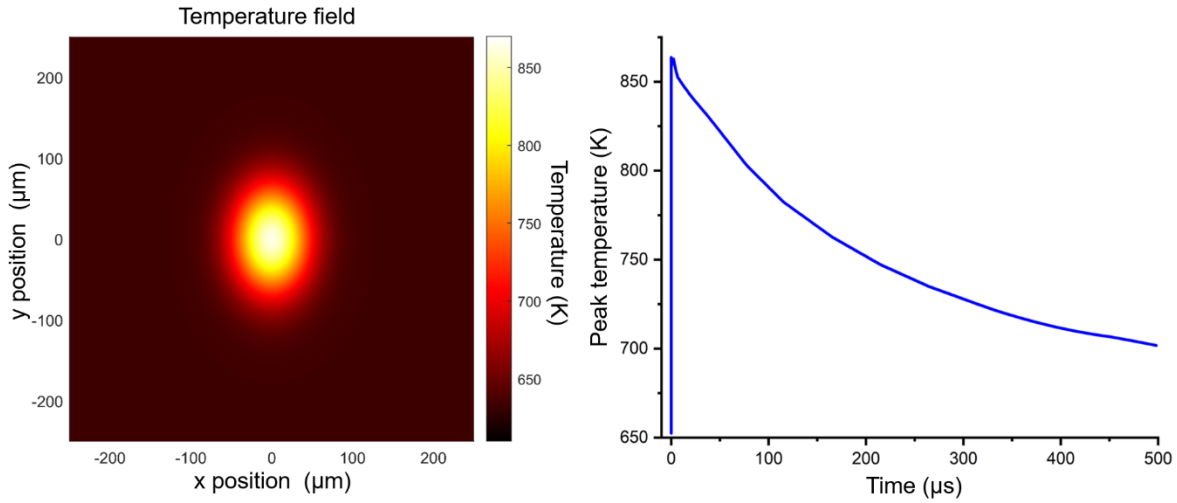

Fig. 8.2. Calculated 2D temperature profile (in the plane of the sample) upon laser irradiation on $Al_{90}Cr_{10}$ film with thickness of 150 nm (left) and peak temperature profile as a function of time (right). The temperature field shown at left correspond to a time of x us after the laser was fired.

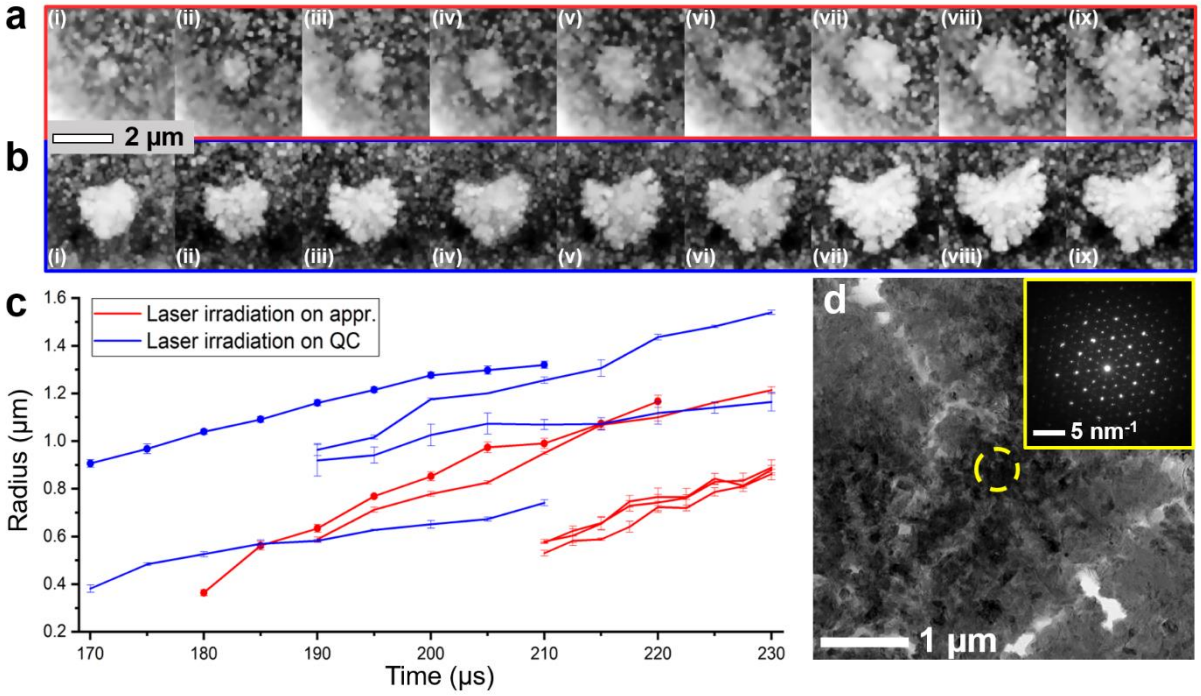

Fig. 8.3. Dynamics of QC precipitation following laser irradiation of Al-Cr thin film samples. Initial condition in (a) was the approximant phase $Al_{13}Cr_2$ and in (b) the Al-Cr icosahedral QC 'seeds'. In both cases, we focus on a single representative precipitate (in white). Time lapse between consecutive images is 5 μs. Note: the QC precipitate seen in (b,i) is not the same QC obtained in (a,ix). (c) Precipitate radius *vs*. time, where 0 μs corresponds to the time at which the laser was fired. Equivalent radii were computed based on the number of pixels that belongs to the growing QC phase after image segmentation. Data points corresponding to (a) and (b) are indicated with red and blue circles, respectively. Growth curves are compiled from multiple DTEM experiments. (d) TEM image of Al-Cr QC precipitate formed via laser irradiation. Inset shows a selected area diffraction pattern with a [000001] zone axis taken from the highlighted area.

The growth sequence of single representative precipitate embedded in an approximant matrix is shown in **Fig. 8.3(a)** after image processing. To enhance the interphase boundaries between the matrix and precipitate, non-local means and Gaussian filters were applied along with black-white inversion. Following an initial incubation period, we were able to observe the growth and morphological evolution of the precipitate from a sphere to a dendrite. The latter transition occurred at some point between **Fig. 8.3(a,ii)** and **Fig. 8.3(a.v)**. No facets were observed at the resolution of the images, suggesting only a minor role of interfacial kinetics. Eventually, the growth process terminates due to reduced driving forces [127] and/or solid diffusivities [187]. The temperature-dependent Cr supersaturation and diffusion are explained afterward. When these same samples were irradiated with a single pulse laser for a second time (**Fig. 8.3(b)**), QC growth occurred almost instantly (negligible incubation time). This is because the pre-existing precipitates

or ‘seeds’ serve as templates for QC growth. This result is further confirmation that the phase transformation proceeds entirely in the solid-state, since the QC liquidus is underneath the equilibrium liquidus [188]. The growth velocities of ~0.01 m/s was measured from **Fig. 8.3(c)**, whether or not the sample contains the seeds. However, the incubation times, determined by extrapolating the growth curves in **Fig. 8.3(c)** to the zero-radius axis, are substantially different: ~ 0 µs with seeds *vs*. ~ 170 µs without.

Post mortem TEM analysis revealed that the fully-grown crystals are indeed icosahedral QCs, as demonstrated by the five-fold selected area electron diffraction (SAED) pattern, see **Fig. 8.3(d)**. Corresponding energy dispersive spectroscopy (EDS) analysis showed that these QCs are enriched in Cr and that they reject Al into the interdendritic regions during precipitation (**Fig. 8.4**). Thus, QC growth is rate-limited by diffusion and not collision [189], since we can find solute partitioning. The average QC grain size over the entire heat-affected zone was approximately 2 µm (**Fig. 8.5**).

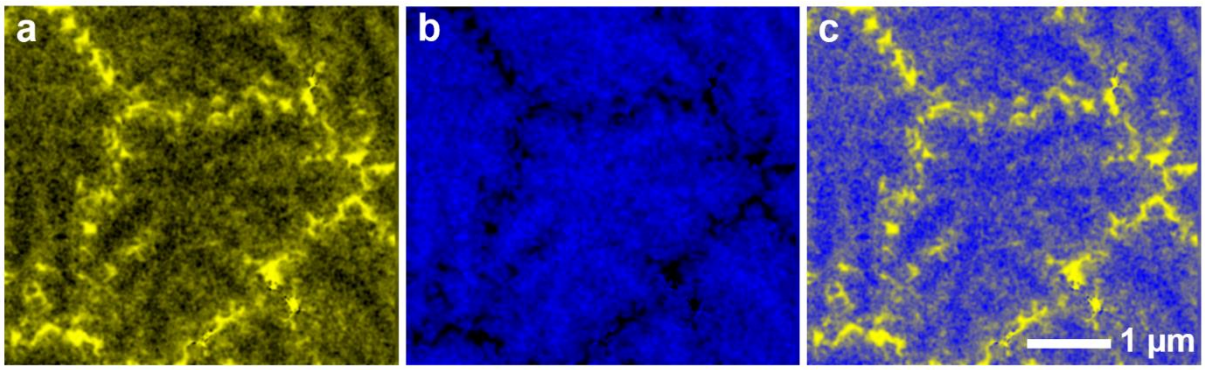

Fig. 8.4. Energy dispersive spectroscopy mapping on Al-Cr QCs of elements (a) Al, (b) Cr, and (c) Al + Cr. The QC is rich in Cr and rejected Al is segregated to the interdendritic regions and grain boundaries.

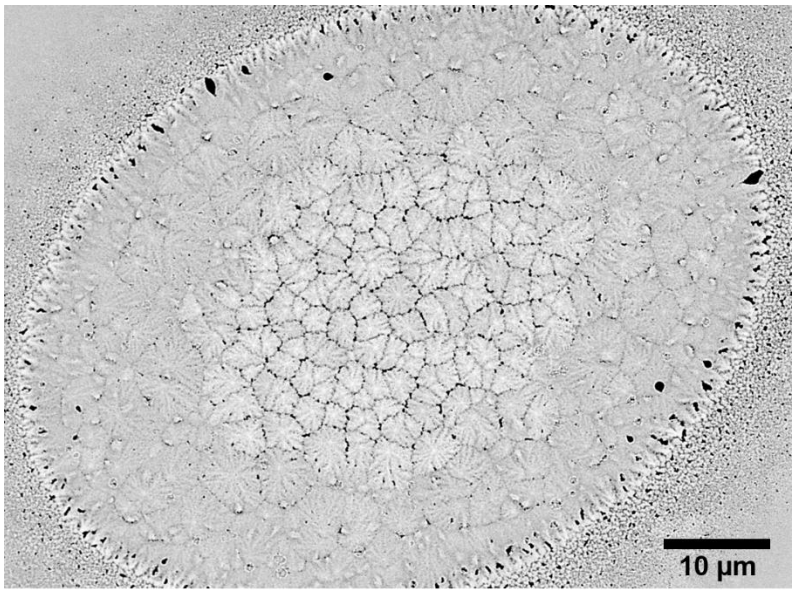

Fig. 8.5. Scanning electron microscopy image of the laser-induced heat-affected zone in the Al-Cr film. The major axis of the heat-affected zone measured approximately 80 µm. The average radius of a dendritic QC grain is approximately 2 µm. The contrast between the center and boundary can be attributed to the lattice with high strain after quenching, which enhances beam scattering.

8.2. Development of interface instabilities

In general, a number of preconditions must be met in order for precipitates to grow dendritically. These include (i) an isotropic precipitate-matrix interfacial energy, (ii) low diffusivity within the growing precipitate, (iii) low 'mismatch' between the precipitate and matrix, and (iv) low precipitate nucleation density [187, 190, 191]. All of these factors allow perturbations to grow in amplitude at the interphase boundary. Bearing these requirements in mind, the formation of dendritic structures upon solidification of a metallic liquid is relatively common due to the missing stabilizing effects against perturbations [190]. Conversely, the formation of solid-state dendrites is extremely rare in Nature [187, 190, 191]. Nevertheless, the QC precipitates seen here uniquely satisfy all of these preconditions: For instance, past work shows that icosahedral QCs possess a nearly-isotropic equilibrium Wulff shape and that transition elements are slow diffusers in icosahedral QCs in comparison to the self-diffusion in Al [192]. Moreover, and as will be demonstrated below, 13-atom icosahedral motifs are common to both QC and approximant phases, thus satisfying precondition (iii). This should lead to a highly mobile interface between the two phases, as there are no kinetic limitations for atoms or clusters to incorporate into the growing QC.

In light of the above considerations, we can test the theoretical predictions of Mullins and Sekerka [69], see also **Sec. 2.2.4**. In their analysis, the critical precipitate radius $R_c(l)$ above which the lth order spherical harmonic should grow is given by Eq. 2.23.

Due to a lack of data on the Al-Cr system, we used γ between Al-Mn icosahedral QC and the approximant Al_6Mn phase, 0.03 J/m^2 at 750 K [193, 194] (note the Al-Mn quasicrystal is isostructural with the Al-Cr QC); Ω is 5.14 x 10^{-4} m^3/mol from the molecular weight of an $Al_{42}Cr_{13}$ Mackay cluster and the density of Al-Mn QC [195]; T at which perturbation were observed in **Fig. 8.3** is roughly 750 K from Fig. 8.2. The values of $R_c(l)$ from the stability criterion of **Eq. 8.1** are plotted in **Fig. 8.6** against the relative supersaturation $|(C_M - C_0)/C_0|$, where we restrict l to be 6, 10, and 12. Only these values of l are possible under l = 16 given the 532 site group symmetry of the icosahedral QC phase [196].

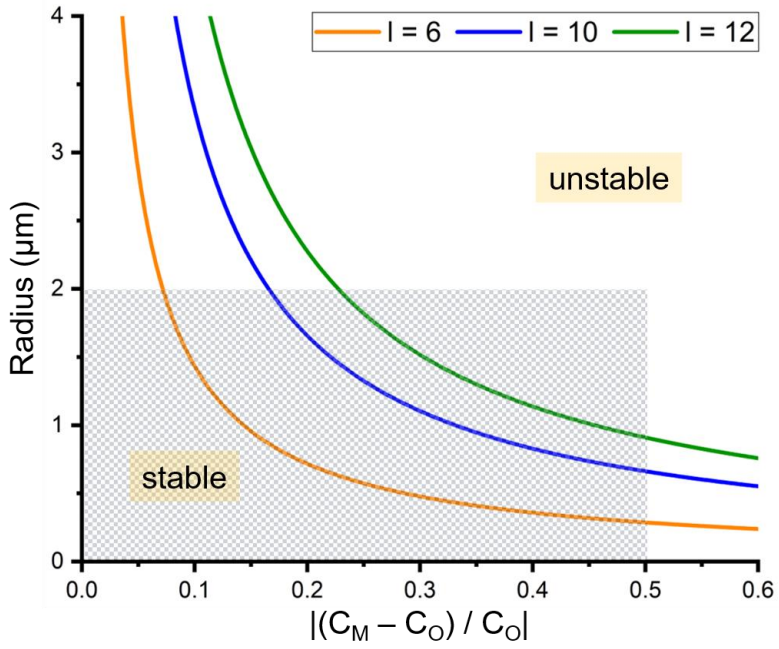

Fig. 8.6. Calculated critical precipitate radius $R_c(l)$ for relative stability as a function of supersaturation. Curves correspond to the lth order spherical harmonic. Interface is radially stable below the neutral curve and radially unstable above it. Shaded area represents the conditions encountered in our DTEM experiment, the boundaries of which are determined by the maximum supersaturation and the average radius of the fully-grown QCs.

In order to pinpoint where our DTEM experiment lands on this morphological stability diagram, we require estimates of the relative supersaturation $|(C_M - C_0)/C_0|$ and the critical radius R_c. We demonstrate in Fig. 8.3 that instabilities tend to grow at precipitate radii well below

R_c ~ 2 μm (see **Fig. 8.5**). Likewise, we take the supersaturation to be is maximal value, *i.e.*, $|(C_M - C_0)/C_0| \rightarrow 0.5$. As we show below, this assumption is reasonable for the diffusion-limited growth (DLG) of a spherical precipitate: Before the development of dendritic protrusions, we can model the QC precipitate as a spherical crystal of radius R and uniform composition C_{QC} that grows in a supersaturated matrix. We take the composition C_0 of the approximant at the QC-approximant interfaces to be the stoichiometric composition of the $Al_{13}Cr_2$ phase. We seek the composition C_M of the approximant far from the QC-approximant interfaces.

For the sake of simplicity, we neglect capillary and interference effects. Assuming DLG [63, 197] of the spherical QC, the time-dependent diffusion equation can be solved to yield the growth rate, *dR/dt* of the precipitate:

$$\frac{dR}{dt} = \frac{1}{2}\,\lambda^2\,\frac{D}{R} \tag{8.2}$$

where the dimensionless interface parameter λ can be approximated as [197, 198]

$$\lambda \sim 2\,\omega/((1-\omega)\,)(1+\sqrt{\omega}+\,\omega) \tag{8.3}$$

and ω is the compositional parameter, $|(C_M - C_0)/(C_{QC} - C_0)|$. At the earliest stages of the growth process (*i.e.*, right before morphological instabilities take over), *dR/dt* is ~0.01 m/s and *R* is ~0.5 μm, as determined from **Fig. 8.3**. The diffusion coefficient D of Cr in $Al_{13}Cr_2$ at 750 K is 1.41 x 10^{-12} ± 0.26 cm^2/s, which was determined through a thin-film diffusion experiment [199], as follows: we first deposited a 300 nm-thich layer of Cr on melt-spun $Al_{13}Cr_2$ ribbons, which were subsequently annealed for different times t of 5, 10, and 20 min. at 750 K. Cr concentration c along the ribbon thickness *x* was measured cross-sectionally by EDS. D was found by fitting the concentration profile c(x,t) to the thin film solution [199] of the diffusion equation. Ultimately, we obtain D of 1.41 x 10^{-12} ± 0.26 cm^2/s from the slope of $\ln(c(x,t) - c_m)$ *vs*. x^2, where c_m is the Cr concentration of $Al_{13}Cr_2$. **Fig. 8.7** shows concentration profile after 20 min. of annealing.

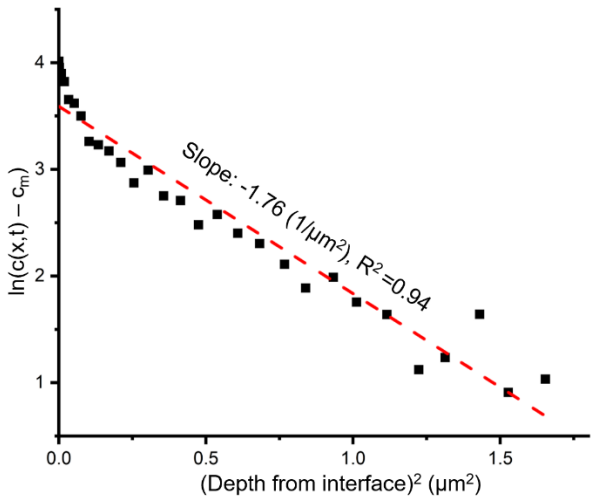

Fig. 8.7. Concentration profile after 20 min. of annealing at 750 K. Fitting this plot to the thin film solution of the diffusion equation gave a Cr self-diffusivity D of 1.18 x 10 $^{-12}$ cm^2/s in the approximant phase.

Using these values, we find $\omega \sim 1$, which corresponds to the theoretical maximum supersaturation $|(C_M - C_0)/C_0| \sim 0.5$. Our measurement of the supersaturation is an upper-bound because it does not account for the diffusional interactions between neighboring QCs [200] (condition (iv)), nor does it account for defects that are created upon laser irradiation [201, 202]. The shaded area in **Fig. 8.6** indicates the region of the morphological stability diagram that we can access through our DTEM experiment. That all three $R_c(l)$ curves intersect this shaded region indicates that dendrites are indeed within the realm of experimental possibilities.

8.3. Insights from *ab initio* MD simulations

The reason that the QC can overcome the stabilizing influence of capillarity (surface tension) and form dendrites so readily is because of its structural similarity to the $Al_{13}Cr_2$ matrix (precondition (iii)). The structural similarity is evidenced with the aid of *ab inito* MD simulation and cluster analysis conducted by Dr. Ling Tang at the Zhejiang University of Technology. The interatomic potential for $Al_{90}Cr_{10}$ is constructed by neural network deep machine learning. Energies and forces of various order and disorder Al, Cr, and binary Al-Cr structures are calculated by first-principles method using VASP package [203], employed as the training dataset. The obtained potential for liquid simulations is validated by comparing the pair correlation function

g(r) of the liquid from the machine learning potential and from ab initio MD simulation as shown in **Fig. 8.8**.

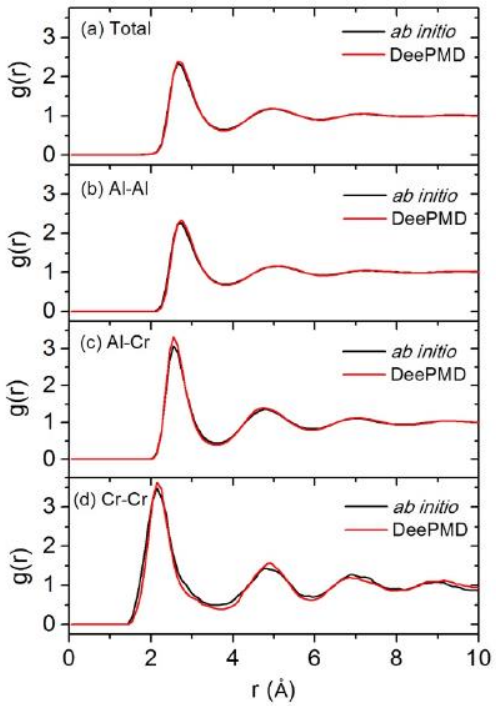

Fig. 8.8. Total and partial pair correlation functions of liquid $Al_{90}Cr_{10}$ at T = 2000 K obtained from the MD simulation using the deep learning potential (DeePMD) are compared with those from ab initio simulations. Both simulations are performed using 200 atoms and averaged over 30 ps.

The MD simulation for the quenched $Al_{90}Cr_{10}$ liquid was performed with an MD cell that contains 4500 Al and 500 Cr atoms and with periodic boundary conditions. An isothermal-isobaric ensemble with the Nose-Hoover thermostat as implemented in the LAMMPS package [204] is used in the simulation [205, 206]. The time step for the MD simulation is 2.5 fs. The liquid $Al_{90}Cr_{10}$ sample is first equilibrated at 2200 K for 500 ps and then is quenched down continuously to 300 K at a cooling rate of 10^{12} K/s. The atomic coordinates averaged over 500 ps at 300 K are then used for the structure order analysis. The short-range order (SRO) in the first-shell of the clusters around every atom in the MD sample is classified by analyzing the similarity between the clusters and the given template structures using the cluster alignment method [207]. The distribution of the alignment score for the Al-centered and Cr-centered clusters are shown in **Fig. 8.9(a) and (b)** respectively. Smaller alignment score indicates a greater degree of similarity between the structure of the cluster and the corresponding template. A cluster is said to have the SRO similar to a given template if its alignment score is below the cut-off score [207]. As one can see from **Fig 8.9**, while

the Al-centered clusters do not have any favorable SRO, about 24 % (area fraction under the black curve) of Cr-centered clusters exhibit very strong icosahedral (ICO) SRO.

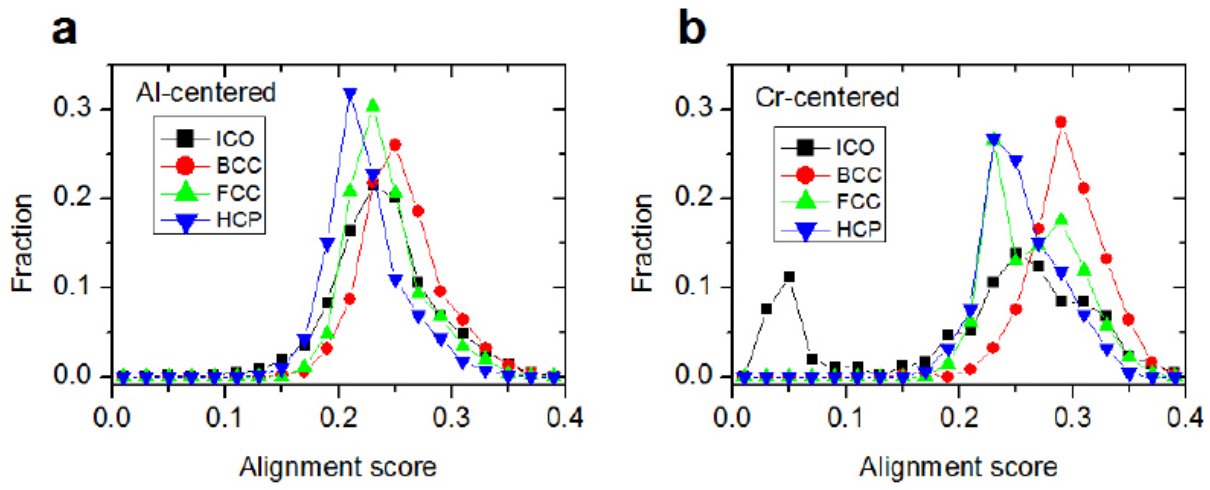

Fig. 8.9. The distribution of alignment scores against various template motifs as indicated by the legend for (a) Al- and (b) Cr-centered clusters in the quenched $Al_{90}Cr_{10}$ liquid at T = 300 K with a cooling rate of 10^{12} K/s.

Further analysis reveals that the unit cell of the approximant $Al_{13}Cr_2$ phase consists of three different types of 13-atom icosahedra, and these icosahedra are linked either by vertices, edges, or triangular faces, or interlocked at the center of neighboring icosahedra [42]. Such icosahedral motifs are frequently observed in Al-Cr QCs as a substructure of 55-atom Mackay cluster [186]. The Mackay clusters are aligned with the five-fold axis of icosahedral QCs and produce a long-range icosahedral order [186]. Our MD simulations trace the emergence of the icosahedral motifs in $Al_{90}Cr_{10}$ alloys. According to **Figs. 8.9 and 8.10**, the dominant SRO in the quenched liquid $Al_{90}Cr_{10}$ is a 13-atom icosahedral cluster, as indicated by a low alignment score (~0.05) and hence a small deviation from the reference structure (the first coordination shell of a Mackay cluster).

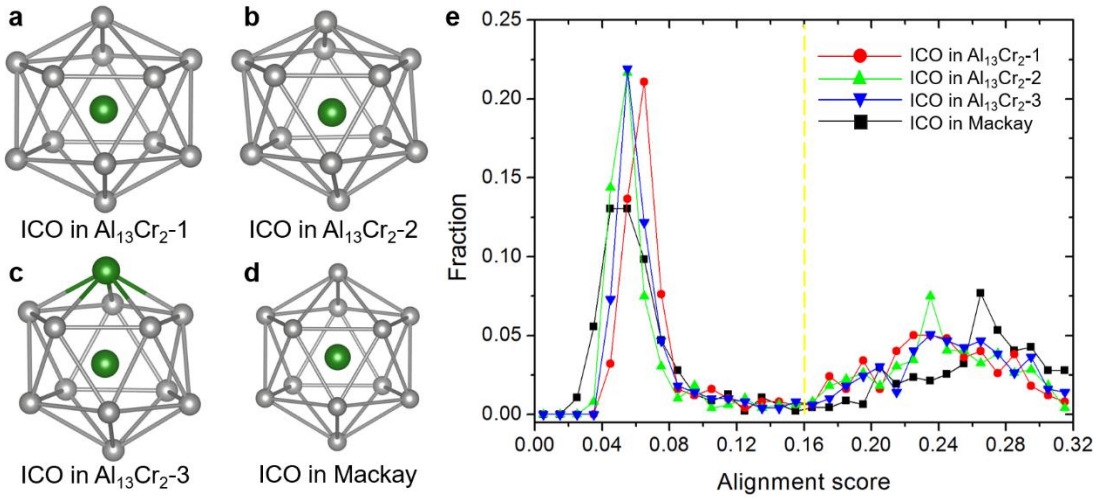

Fig. 8.10. Short-range-order (SRO) of $Al_{90}Cr_{10}$ alloy, quenched from 2200 K to 700 K at a rate of 10^{11} K/s. For reference, we show (a-c) three types of 13-atom, Cr-centered clusters in the approximant $Al_{13}Cr_2$ phase and (d) a prototypical icosahedron (*i.e.*, the first coordination shell of a 55-atom Mackay cluster). Note the simulated clusters depicted in (a-d) are slightly distorted from the referenced icosahedra. While they may look similar, they can be distinguished from each other: the corresponding ratio of average Cr-Al bond lengths in (a-d) is 1.03:1.02:1.01:1.00. The green and gray balls in (a-d) represent Cr and Al atoms, respectively. (e) Cluster analysis on rapidly quenched $Al_{90}Cr_{10}$ liquid, wherein the Cr-centered motifs are compared to those shown in (a-d). Clusters are said to have the SRO similar to the given reference structure when their alignment score is below the cut-off value of 0.16 (indicated by a yellow dashed line). A low score indicates small deviation from the reference.

This can be attributed to the prevailing SRO in the liquid phase at high temperatures [208] (see **Fig. 8.8**). We have also compared the Cr-centered structural motifs in the quenched alloy to the three types of icosahedra in the approximant $Al_{13}Cr_2$ phase (**Fig. 8.10**). Here, too we observe a high degree of structural similarity despite the slight differences in Cr-Al bond lengths (consistent with the EXAFS results in **Figs. 8.1(a,b)**). In light of these results, we suppose that the 13-atom icosahedral clusters can survive annealing and laser irradiation and ultimately contribute to the formation of icosahedral QCs in the solid-state. The structural similarity between QC and approximant does not extend to the second shell, however: when we conducted cluster analysis using 55-atom Mackay clusters, we do not obtain as low of a score, which means that the 55-atom Mackay clusters are not common structural motifs (**Fig. 8.11; *cf.* Fig. 8.10**).

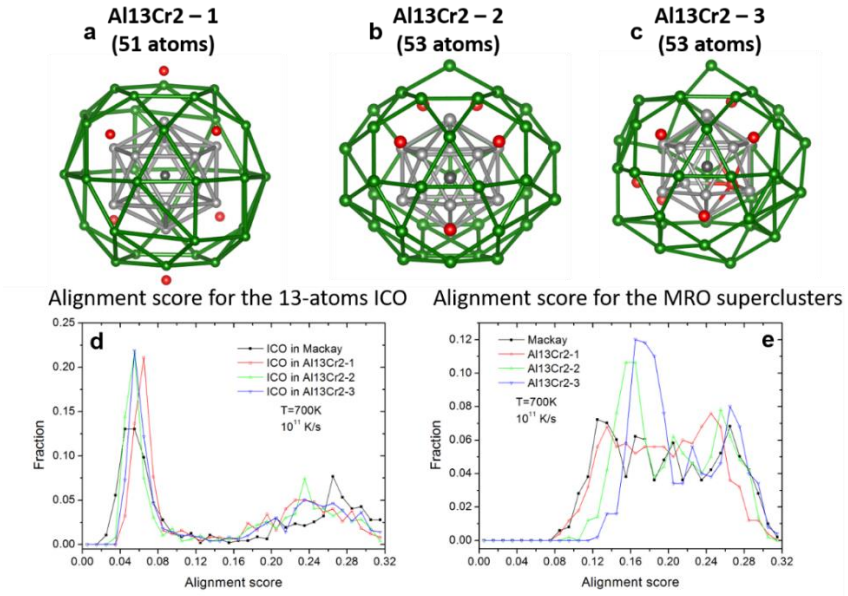

Fig. 8.11. (a,b,c) Three types of Cr sites in the approximant $Al_{13}Cr_2$ phase (labelled 1-3). The first shell (gray) surrounding each site consists of 12 atoms; the second shell (green) has 38-40 atoms. The green and red balls in (a-c) represent Al and Cr atoms, respectively. The ratio of the three sites is 1:2:4. Cluster analysis of $Al_{13}Cr_2$-1, -2, -3 and Mackay clusters with (d) the 13-atom icosahedral motif and (e) MRO superclusters in rapidly quenched $Al_{90}Cr_{10}$.

The significance of these icosahedral clusters has long been a matter of debate in the scientific community. The central question is whether they impart a physical stability to QCs or if they simply appeal to our need to organize complex information into small units [209]. Here, we show that clusters are not only important from a structural perspective but also from a kinetic one: they facilitate the 'easy' transition from one solid intermetallic phase to another. That is, the long-range icosahedral order in QCs can be readily obtained by the motion of a few atoms from the short-range icosahedral order in the approximant phase [210]. As the clusters move into registry, whether by local 'matching' rules [211] or otherwise, they displace the surrounding Al atoms (solute rejection, see **Fig. 8.4**). Clearly, this ordering occurs by a nucleation and growth mechanism (**Fig. 8.3**). Without this common structural motif between the QC and approximant phases, the interphase boundaries would possess a relatively low mobility, thereby stabilizing the precipitates against dendritic perturbations [76]. The existence of icosahedral clusters (**Figs. 8.9 and 8.10**) may also explain why we should see metastable QC precipitates in the first place, and why QCs are often observed as intermediate phases in multi-step nucleation processes [212]. These arguments can be extended to other phase transitions involving liquid or amorphous [213] precursors.

Part IV. Conclusions & Outlooks

This dissertation focused on investigating the formation of QCs and their approximants under various growth conditions, by taking advantage of cutting-edge characterization techniques and corresponding molecular simulations. The work reports significant advancement of fundamental science underlying the growth pathways of complex intermetallics more generally. To sum up, the questions that have been addressed in this thesis are as follows:

- What mechanisms dominate the growth and dissolution processes of a single d-QC?

By extracting morphological, dynamic, and compositional information directly from our space- and time-resolved data, we were able to provide a fresh lens on these poorly understood phase transitions. On the basis of our results, we determined that the decagonal Al-Ni-Co QC grows *via* a normal growth mechanism, similar to periodic crystals with atomically "rough" facets. Even so, the growth rate is remarkably sluggish compared to those of periodic crystals due to the rearrangement of clusters at the solid-liquid interface. To quantify the growth kinetics, we calculated an interface kinetic coefficient of 2.5×10^{-6} cm s^{-1} K^{-1}, that is independent of the magnitude of the driving force. Hence, this coefficient can be used as input for mesoscale models (*e.g.*, phase field simulations). On the other hand, melting is not an activated process and is governed purely by gravity-driven convection. Therefore, we can conclude that the growth and dissolution processes do not have time-reversal symmetry.

- What are the kinetic and equilibrium shapes of QCs?

Growth of the i-QC phase from a liquid phase is largely governed by gravity-induced convection. During this growth regime, the i-QC takes on a pentagonal dodecahedral shape. Once the supersaturation in the liquid has been almost entirely depleted, the pentagonal dodecahedron evolves into a truncated dodecahedron near-ES, indicating that the pentagonal dodecahedron is not the lowest energy structure in this i-QC. Our result is in support of the theoretic work by Ho *et al*., who found that the pentagonal dodecahedron could not be the ES in i-QCs but can exist in non-equilibrium conditions [150]. Thus, the equilibrium and kinetic shapes of i-QCs are not necessarily identical, as previously assumed by several investigators [78, 80, 152, 153].

- To what extent are the crystallization pathways of QCs and approximants the same?

From the side-by-side comparison of the solidification dynamics of quasicrystalline and approximant phases in the Al-Ni-Co system, we found that the d-QC and approximant X phases possess markedly different kinetic signatures despite being crystallographically related. While growth of the X phase is governed by first-order kinetics, in the same manner as for the d-QC, the two solid phases differ with respect to their nucleation and growth rates. A greater constitutional undercooling enables a higher nucleation rate for the X phase crystals. The nucleated, approximant-phase crystals are unable to grow as fast as the d-QC due to `soft collisions' between overlapping diffusion fields. Yet even those X phase crystals that grow freely and away from other *X*-phase crystals have anomalously slow growth rates. This is most likely because extensive cluster rearrangements are necessary to maintain the translational symmetry of the periodic lattice. Meanwhile, the d-QC does not experience as great a kinetic undercooling at the solid–liquid interface since it is able to incorporate the atomic clusters at random. It is for this reason that the measured kinetic coefficient of the *X* phase is about one-fifth that of the d-QC.

- How do QCs interact with each other *via* hard collisions?

From the joint experiment and simulation, we were able to provide a cohesive picture for the conditions that give rise to grain coalescence: (i) parallel periodic axes and (ii) small misorientation between quasiperiodic lattices. In this operating regime, we observed grain rotation toward 0° misorientation in order to minimize grain-boundary energy. This process occurs through a dislocation- mediated mechanism that allows the d-QCs to redistribute phonon strain due to lattice mismatch as phason strain, by local rearrangement of dislocations into valid tilings. Taken altogether, our integrated approach highlights the exciting opportunity for microstructure optimization via control of the grain boundaries – that is, defect engineering.

- How do QCs grow dendritically in the solid-state?

Indeed, while QCs have been shown to grow dendritically in a *liquid* [60–62], we provide real-time experimental assessment *via* DTEM of this particular growth mode in the *solid-state*. We rationalize the development of morphological instabilities based on the similarity in local orders

between QC and approximant. With the aid of *ab initio* MD simulations, we trace this structural similarity to 13-atom, Cr-centered icosahedral clusters. These clusters readily assemble into icosahedral QCs without substantial rearrangements. This atomic picture fully explains the growth process of metastable QC dendrites in systems that are driven far-from-equilibrium.

Looking ahead, I believe the recent advancements in characterization techniques would help to answer the remaining questions in QC growth, such as developing three-dimensional growth models starting with nucleation from the melt [5]. For example, the recently renovated X-ray nanotomography beamline at NSLS-II noticeably improved the temporal resolution of the technique by a factor of ten, to less than one minute per 3D tomogram [214], while still maintaining a high spatial resolution (~ 30 nm). This new setup is compatible with the newly developed high temperature *in situ* heater [215] with maximum temperature greater than 1100 °C and high thermal stability. I was among the first to test this heater in the fall of 2019 [215]. These advanced experimental setups are ideal to investigate transient solidification and precipitation behaviors of QCs with much higher spatial resolution and may in turn allow us to investigate in greater detail the interface between QC and its parent phase and its growth mechanism.

In addition, continued efforts to improve the temporal and spatial resolutions of DTEM would help us to capture the growth of QCs from their nucleation stage and eventually provide evidence of short range order in a supercooled liquid. By lowering the contents of TM in Al-TM films, we may be able to melt the sample in the DTEM and observe the rapid solidification behaviors of QCs, which should nucleate with minimal undercooling [188]. Finally, the coupling of advanced experimental and simulation approaches would enable significant progress in solving complex problems in the realm of the structure, stability and growth of QCs, such as the migration of phasons, dislocations, and grain boundaries in the as-solidified QCs.

Appendix

A. Rapid solidification and stability of interfaces

Rapid solidification denotes either of the following two conditions: (i) High bulk undercooling of the melt in the absence of efficient heterogeneous nucleants, or by rapid quenching (*e.g.* atomization, melt spinning) and (ii) rapidly moving temperature fields by high power density sources (*e.g.* laser, e-beam) [50]. One consequence of rapid cooling is the breakdown of the local equilibrium at the interface (*e.g.* solid-liquid or solid-solid), see **Table A1**.

Increasing undercooling or solidification velocity ↓	I. Full diffusional (global) equilibrium A. No chemical potential gradients (composition of phases are uniform) B. No temperature gradients C. Lever rule applicable
	II. Local interfacial equilibrium A. Phase diagram gives compositions and temperatures only at liquid - solid interface B. Corrections made for interface curvature (Gibbs - Thomson effect)
	III. Metastable local interface equilibrium A. Stable phase cannot nucleate or grow sufficiently fast B. Metastable phase diagram (a true thermodynamic phase diagram missing the stable phase or phases) gives the interface conditions
	IV. Interface non-equilibrium A. Phase diagram fails to give temperature and compositions at the interface B. Chemical potentials are not equal at the interface C. Free energy functions of phases still lead to criteria for impossible reactions

Table Al. Hierarchy of equilibrium. Reprinted from [216].

For example, solidification or precipitation can occur without change in composition, also known as a *massive transformation*. Massive transformation includes partitionless solidification and solute trapping. The effect of solute trapping can be seen in the reduction of the solid and liquid compositions at the interface with velocity and by the decrease of the interval between liquidus and solidus curves [217]. Stated differently, the non-equilibrium partition coefficient $k(V) \to 1$ as $V \to \infty$. In this section, we will discuss the relationship between the interface velocity and interface morphology.

At low interface velocity, a planar interface is stable to perturbations if the thermal gradient is larger than the liquidus temperature gradient, recall **Fig. 2.4**. Ignoring capillary effects, the flat interface prevails when the interface velocity is smaller than a critical velocity V_c [218]

$$V_c = \frac{\bar{G}D}{\Delta T_0} \tag{A.1}$$

where $\bar{G}$ denotes the conductivity-weighted temperature gradient and ΔT_0 represents the equilibrium interval between liquidus and solidus curves. Under V_c, we should expect a steady-state plane-front growth (case A in **Fig. A1**). Above V_c, the interface adopts a cellular or dendritic morphology and the growth temperature rises above the equilibrium solidus temperature, such that the solid concentration is less than the initial composition of the alloy, C_0 [217] (cases B & C in **Fig. A1**). At higher velocities, a cellular or dendritic microstructure becomes finer in length-scale. When the velocity exceeds the upper limit V_a, diffusion becomes localized and capillarity (inversely proportional to this length-scale) takes control in the Mullins-Sekerka framework (see Sec. 2.2.4). Consequently, we should expect a plane-front growth interface once again. The velocity that determines absolute stability V_a is given by

$$V_a = \frac{\Delta T_0(V)D}{k_v \Gamma} \tag{A.2}$$

where k_v and Γ denote nonequilibrium liquidus slope and Gibbs-Thomson coefficient, respectively. Beyond the absolute stability limit, and particularly when dT/dV > 0, oscillatory instabilities may occur and result in banded structures, which is produced by the alternate growth of two phases [219]. However, such oscillatory structures do not form when there is low interphase mobility (*e.g.* solid-solid) and the distribution coefficient $k(V)$ is close to unity (cases D & E in **Fig. A1**).

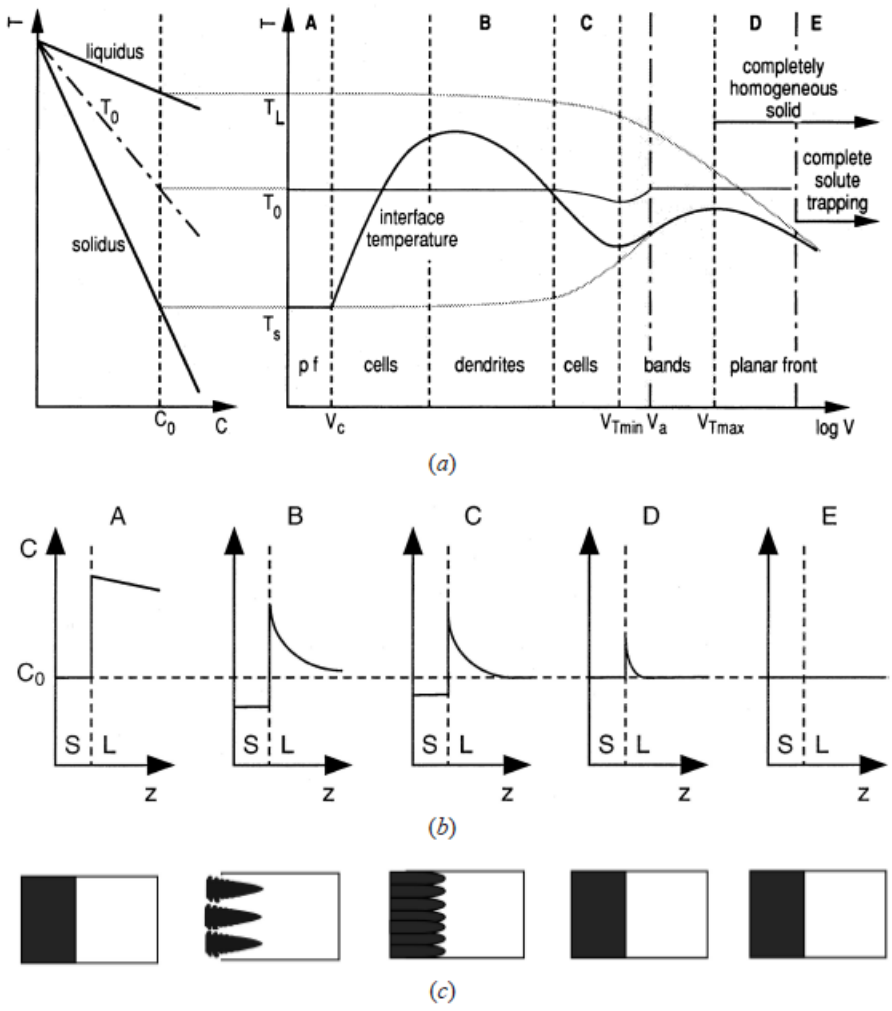

Fig. A1. (a) Schematic representation of interface velocity *vs*. temperature function, and corresponding (b) concentration profiles and (c) interface morphologies. Retrieved from [217].

Bibliography

[1] D. Shechtman et al., Metallic phase with long-range orientational order and no translational symmetry, *Phys. Rev. Lett.* **53**, 1951, (1984).

[2] I. Han, X. Xiao and A.J. Shahani, Probing the growth and melting pathways of a decagonal quasicrystal in real-time, *Sci. Rep*. **7**, 17407, (2017).

[3] Report of the Executive Committee for 1991, *Acta Cryst*. **A48**, 922, (1992).

[4] L. Bendersky, Quasicrystal with one-dimensional translational symmetry and a tenfold rotation axis, *Phys. Rev. Lett*., **55**, 1461, (1985).

[5] W. Steurer, Quasicrystals: What do we know? What do we want to know? What can we know?, *Acta Cryst*. **A74**, 1, (2018).

[6] R. Penrose, The role of aesthetics in pure and applied mathematical research, *Bull. Inst. Math. Appl*., **10**, 266, (1974).

[7] D. Levine and P.J. Steinhardt, Quasicrystals: a new class of ordered structures, *Phys. Rev. Lett.* **53**, 2477, (1984).

[8] L. Bursill and P.J. Lin, Penrose tiling observed in a quasi-crystal, *Nature*, **316**, 50, (1985).

[9] M.V. Jarić and D.R. Nelson, Diffuse scattering from quasicrystals, *Phys. Rev. B*, **37**, 4458, (1988).

[10] K.J. Strandburg, Random-tiling quasicrystal, *Phys. Rev. B*, **40**, 6071, (1989).

[11] V. Elser, Random tiling structure of icosahedral quasicrystals, *Phil. Mag. B*, **73**, 641, (1996).

[12] H.-C. Jeong and P.J. Steinhardt, Cluster approach for quasicrystals, *Phys. Rev. Lett*. **73**, 1943, (1994).

[13] P.J. Steinhardt et al., Experimental verification of the quasi-unit-cell model of quasicrystal structure, *Nature*, **396**, 55, (1998).

[14] G.Y. Onoda et al., Growing perfect quasicrystals, *Phys. Rev. Lett*., **60**, 2653, (1988).

[15] C. Janot, Quasicrystals, Neutron and Synchrotron Radiation for Condensed Matter Studies, Springer, (1994).

[16] S. Walter and S. Deloudi, Crystallography of quasicrystals: concepts, methods and structures, Springer Science & Business Media, (2009).

[17] M. de Boissieu, Stability of quasicrystals: energy, entropy and phason modes, *Phil. Mag*., **86**, 1115, (2006).

[18] M. de Boissieu, Phonons, phasons and atomic dynamics in quasicrystals, *Chem. Soc. Rev*., **41**, 6778, (2012).

[19] J.E. Socolar, T. Lubensky and P.J. Steinhardt, Phonons, phasons, and dislocations in quasicrystals, *Phys. Rev. B*, **34**, 3345, (1986).

[20] L.D. Landau, On the theory of phase transitions. I, *Phys. Z. Sowjet*., **11**, 26, (1937).

[21] M. Engel et al., Dynamics of particle flips in two-dimensional quasicrystals, *Phys. Rev. B*, **82**, 134206, (2010).

[22] R. Blüher et al., First low-temperature radiotracer studies of diffusion in icosahedral quasicrystals, *Phys. Rev. Lett*., **80**, 1014, (1998).

[23] K. Sato et al., Study of an order-disorder phase transition on an atomic scale: the example of decagonal Al-Ni-Co quasicrystals, *Phys. Rev. Lett*., **92**, 127403, (2004).

[24] C. Henley, M. De Boissieu and W. Steurer, Discussion on clusters, phasons and quasicrystal stabilisation, *Phil. Mag*., **86**, 1131, (2006).

[25] K. Edagawa, K. Suzuki and S. Takeuchi, HRTEM observation of phason flips in Al–Cu–Co decagonal quasicrystal, *J. Alloys Compd*., **342**, 271, (2002).

[26] K. Edagawa, K. Suzuki and S. Takeuchi, High resolution transmission electron microscopy observation of thermally fluctuating phasons in decagonal Al-Cu-Co, *Phys. Rev. Lett*., **85**, 1674 (2000).

[27] K. Nagao et al., Experimental observation of quasicrystal growth, *Phys. Rev. Lett*., **115**, 075501, (2015).

[28] G. Coddens et al., Evidence for phason hopping in icosahedral AlFeCu quasi-crystals, *Europhys. Lett*., **16**, 271, (1991).

[29] S. Lyonnard et al., Atomic (phason) hopping in perfect icosahedral quasicrystals $Al_{70.3}Pd_{21.4}Mn_{8.3}$ by time-of-flight quasielastic neutron scattering, *Phys. Rev. B*, **53**, 3150, (1996).

[30] G. Coddens et al., Evidence for atomic hopping of Fe in perfectly icosahedral AlFeCu quasicrystals by ^{57}Fe Mössbauer spectroscopy, *J. Phys. I*, **5**, 771, (1995).

[31] J. Dolinsek et al., Atomic motion in quasicrystalline $Al_{70}Re_{8.6}Pd_{21.4}$: A two-dimensional exchange NMR study, *Phys. Rev. Lett*., **81**, 3671, (1998).

[32] J. Dolinšek et al., Self-Diffusion in Icosahedral Al72.4Pd20.5Mn7.1 and Phason Percolation at Low Temperatures Studied by ^{27}Al NMR, *Phys. Rev. Lett*., **82**, 572, (1999).

[33] J. Socolar, Phason strain in quasicrystals, *J. Phys. Colloques*, **47**, C3-217, (1986).

[34] P.A. Bancel et al., Structure of rapidly quenched Al-Mn, *Phys. Rev. Lett*., **54**, 2422, (1985).

[35] C. Guryan et al., Al-Cu-Ru: An icosahedral alloy without phason disorder, *Phys. Rev. Lett*., **62**, 2409, (1989).

[36] V. Elser and C.L. Henley, Crystal and quasicrystal structures in Al-Mn-Si alloys, *Phys. Rev. Lett*., **55**, 2883, (1985).

[37] C. Dong, The concept of the approximants of quasicrystals, *Scr. Metall. Mater*., **33**, 239, (1995).

[38] J. Dolinšek et al., Anisotropic magnetic and transport properties of orthorhombic Al13Co4, *Phys. Rev. B*, **79**, 184201, (2009).

[39] P. Gille et al., Single crystal growth of Al-based intermetallic phases being approximants to quasicrystals, *J. Cryst. Growth*, **318**, 1016, (2011).

[40] X. Ma and K. Kuo, Decagonal quasicrystal and related crystalline phases in slowly solidified Al-Co alloys, *Metall. Trans. A*, **23**, 1121, (1992).

[41] M. Widom and E. Cockayne, Atomic correlations in AlCo decagonal approximant phases, *Phys. A*, **232**, 713, (1996).

[42] E. Liotti et al., Synchrotron X-ray and neutron investigation of the structure and thermal expansion of the monoclinic $Al_{13}Cr_2$ phase, *J. Alloys Compd*., **781**, 1198, (2019).

[43] N. Tamura, The concept of crystalline approximants for decagonal and icosahedral quasicrystals, *Phil. Mag. A*, **76**, 337, (1997).

[44] F. Audebert et al., Laser cladding of aluminium-base quasicrystalline alloys, *Scr. Mater*., **40**, 551, (1999).

[45] M. Boudard et al., Structure of quasicrystalline approximant phase in the Al-Pd-Mn system, *Phil. Mag. A*, **74**, 939, (1996).

[46] Y. Yokoyama et al., Preparation of Decagonal Al–Ni–Co Single Quasicrystal by Czochralski Method, *Mater. Trans., JIM*, **38**, 943, (1997).

[47] R. Dunlap et al., Structural, electrical and magnetic properties of icosahedral Al-Co alloys, *J. Phys. F*, **16**, 1247, (1986).

[48] S. Katrych et al., X-ray diffraction study and theoretical calculations on the X-phase, $Al_9(Co, Ni)_4$, *Phil. Mag*., **86**, 451, (2006).

[49] W. Kurz, Fisher; DJ: Fundamentals of Solidification, Trans Tech Publications, (1992).

[50] D.A. Porter, K.E. Easterling, Phase transformations in metals and alloys (revised reprint), CRC press, (2009).

[51] J.A. Dantzig, M. Rappaz, Solidification: -Revised & Expanded, EPFL press, (2016).

[52] F. Spaepen, A structural model for the solid-liquid interface in monatomic systems, *Acta Metall*, **23**, 729, (1975).

[53] C.V. Thompson, PhD thesis, (1979).

[54] F. Spaepen and R.B. Meyer, The surface tension in a structural model for the solid-liquid interface, *Scr. Metall*., **10**, 257, (1976).

[55] D. Holland-Moritz, D. Herlach and K. Urban, Observation of the undercoolability of quasicrystal-forming alloys by electromagnetic levitation, *Phys. Rev. Lett*., **71**, 1196, (1993).

[56] D. Holland-Moritz, On the energy of the interface between a melt and quasicrystalline and polytetrahedral phases, *J. Non-Cryst. Solids*, **250**, 839, (1999).

[57] T. Schenk et al., Icosahedral short-range order in deeply undercooled metallic melts, *Phys. Rev. Lett.*, **89**, 075507, (2002).

[58] D. Holland-Moritz et al., Short-range order in undercooled Co melts, *J. Non-Cryst. Solids*, **312**, 47, (2002).

[59] D. Holland-Moritz et al., Short-range order in undercooled and stable melts forming quasicrystals and approximants and its influence on nucleation, *Phil. Mag.*, **86**, 255, (2006).

[60] W. Hornfeck et al., Quasicrystal nucleation and $\mathbb{Z}$ module twin growth in an intermetallic glass-forming system, *Nat. Comm.*, **9**, 1, (2018).

[61] G. Kurtuldu, P. Jarry and M. Rappaz, Influence of Cr on the nucleation of primary Al and formation of twinned dendrites in Al–Zn–Cr alloys: Can icosahedral solid clusters play a role?, *Acta Mater.*, **61**, 7098, (2013).

[62] D.A. Molodov, Microstructural design of advanced engineering materials, John Wiley & Sons, (2013).

[63] L. Ratke, P.W. Voorhees, Growth and coarsening: Ostwald ripening in material processing, Springer Science & Business Media, (2013).

[64] K.A. Jackson, Kinetic Processes: crystal growth, diffusion, and phase transformations in materials, John Wiley & Sons, (2006).

[65] W.A. Tiller, The science of crystallization: microscopic interfacial phenomena, Cambridge University Press, (1991.)

[66] R.W. Balluffi, S.M. Allen and W.C. Carter, Kinetics of materials, John Wiley & Sons, (2005).

[67] D.N. Lee, Orientations of dendritic growth during solidification, *Met. Mater. Int.*, **23**, 320, (2017).

[68] J. Lipton, M. Glicksman and W. Kurz, Equiaxed dendrite growth in alloys at small supercooling, *Metall. Mater. Trans. A*, **18**, 341, (1987).

[69] W.W. Mullins, R.F. Sekerka, Morphological stability of a particle growing by diffusion or heat flow, *J. Appl. Phys*., **34**, 323, (1963).

[70] S. Baumann, D.B. Williams, Experimental observations on the nucleation and growth of δ′(Al3Li) in dilute Al-Li alloys, *Metall. Trans. A*, **16**, 1203, (1985).

[71] M. Henry et al., The dendritic growth of γ′ precipitates and grain, *Metall. Trans. A*, **24**, 1733, (1993).

[72] J.C. Baker, J.W. Cahn, Thermodynamics of solidification, The Selected Works of John W. Cahn, 253, (1998).

[73] K. Russell, Phase transformations, ASM, (1970).

[74] W. Steurer, Quasicrystal structure and growth models: discussion of the status quo and the still open questions, *J. Phys. Conf. Ser*., **809**, 012001, (2017).

[75] T.A. Land, J.J. De Yoreo, The evolution of growth modes and activity of growth sources on canavalin investigated by in situ atomic force microscopy, *J. Cryst. Growth*, **208**, 623, (2000).

[76] A.A. Chernov, Modern crystallography III: crystal growth, Springer Science & Business Media, (2012).

[77] I.V. Markov, Crystal growth for beginners: fundamentals of nucleation, crystal growth and epitaxy, World scientific, (2016).

[78] T. Schenk et al., Application of synchrotron X-ray imaging to the study of directional solidification of aluminium-based alloys, *J. Cryst. Growth*, **275**, 201, (2005).

[79] H.N. Thi et al., In situ and real-time probing of quasicrystal solidification dynamics by synchrotron imaging, *Phys. Rev. E*, **74**, 031605 (2006).

[80] J. Gastaldi et al., In situ study of quasicrystal growth by synchrotron X-ray imaging, *Phil. Mag*., **87**, 3079, (2007).

[81] E. Pearson et al., Computer modeling of Si and SiC surfaces and surface processes relevant to crystal growth from the vapor, *J. Cryst. Growth*, **70**, 33, (1984).

[82] S. Hofmann et al., Ledge-flow-controlled catalyst interface dynamics during Si nanowire growth, *Nat. Mater*., **7**, 372, (2008).

[83] C.-Y. Wen et al., Structure, growth kinetics, and ledge flow during vapor-solid-solid growth of copper-catalyzed silicon nanowires, *Nano Lett.*, **10**, 514, (2010).

[84] Spatial and temporal resolutions of imaging techniques (berstructuralbioportal.org/capabilities.shtml)

[85] J. Als-Nielsen, D. McMorrow, Elements of modern X-ray physics, John Wiley & Sons, (2011).

[86] N. Senabulya, X. Xiao, I. Han, A.J. Shahani, On the kinetic and equilibrium shapes of icosahedral $Al_{71}Pd_{19}Mn_{10}$ quasicrystals, *Scr. Mater.*, **146**, 218, (2018).

[87] Y. Yokoyama *et al.*, Al–Pd–Mn Alloys with Large Single Domain Size, *Mater. Trans., JIM*, **32**, 1089, (1991).

[88] M. Rivers, Synchrotron 'pink beam' tomography for the study of dynamic processes, *SPIE Newsroom*, (2006).

[89] D. Gürsoy et al., TomoPy: a framework for the analysis of synchrotron tomographic data, *J. Synchrotron Radiat.*, 21, 1188, (2014).

[90] B. Münch et al., Stripe and ring artifact removal with combined wavelet—Fourier filtering, *Opt. express*, **17**, 8567, (2009).

[91] B.A. Dowd *et al.*, Developments in synchrotron x-ray computed microtomography at the National Synchrotron Light Source, *Int. Soc. Opt. Photon.*, **3772**, 224, (1999).

[92] M. Desbrun *et al.*, Implicit fairing of irregular meshes using diffusion and curvature flow, Proceedings of the 26th annual conference on Computer graphics and interactive techniques, (1999).

[93] M. Botsch, L. Kobbelt, M. Pauly, P. Alliez, B. Lévy, Polygon mesh processing, CRC press (2010).

[94] R. Mendoza, PhD thesis (2003).

[95] A.J. Shahani et al., Ostwald ripening of faceted Si particles in an Al-Si-Cu melt, *Mater. Sci. Eng. A*, **673**, 307, (2016).

[96] T. LaGrange *et al*., *Micron*, 43, 1108, (2012).

[97] T. LaGrange, B.W. Reed and D.J. Masiel, Movie-mode dynamic electron microscopy, *MRS Bull.*, **40**, 22, (2015).

[98] R. Dunlap and K. Dini, Structure and stability of quasicrystalline aluminium transition-metal alloys, *J. Phys. F*, **16**, 11, (1986).

[99] C.V. Thompson, Solid-state dewetting of thin films, *Annu. Rev. Mater. Res*., **42**, 399, (2012).

[100] M. Newville, IFEFFIT: interactive XAFS analysis and FEFF fitting, J. Synchrotron Radiat., 8, 322, (2001).

[101] J. Murray, The Al-Cr (aluminum-chromium) system, *J. Phase Equilib. Diff.*, **19**, 368, (1998).

[102] K. Zweiacker et al., Determination of crystal growth rates during rapid solidification of polycrystalline aluminum by nano-scale spatio-temporal resolution in situ transmission electron microscopy, *J. Appl. Phys.*, **20**, 055106, (2016).

[103] W.M. Haynes, CRC handbook of chemistry and physics, CRC press, (2014).

[104] I. Han *et al.*, A side-by-side comparison of the solidification dynamics of quasicrystalline and approximant phases in the Al–Co–Ni system, *Acta Cryst*., **A75**, 281, (2019).

[105] I. Han *et al.*, Dynamic observation of dendritic quasicrystal growth upon laser-induced solid-state transformation, in revision (2020).

[106] I. Han *et al.*, Formation of a single quasicrystal from multiple seeds to be submitted (2020).

[107] A.-P. Tsai, A. Inoue and T. Masumoto, Stable decagonal Al–Co–Ni and Al–Co–Cu quasicrystals, *Mater. Trans., JIM*, 30, 463, (1989).

[108] Y. Wang and G. Cacciamani, Experimental investigation and thermodynamic assessment of the Al-Co-Ni system, Calphad, **61**, 198, (2018).

[109] D. Ruvalcaba *et al.*, In situ observations of dendritic fragmentation due to local solute-enrichment during directional solidification of an aluminum alloy, Acta Mater., 55, 4287, (2007).

[110] P. Gille, G. Meisterernst, and N. Faber, Inclined net plane faceting observed at Czochralski growth of decagonal AlCoNi quasicrystals, J. Cryst. Growth, 275, 224, (2005).

[111] G. Meisterernst, B. Bauer, and P. Gille, Czochralski Growth of Decagonal AlCoNi Quasicrystals from Al-rich Solution, *Acta Phys. Pol. A.* **124**, 344, (2013).

[112] A.J. Shahani *et al.*, Twin-mediated crystal growth: an enigma resolved, *Sci. Rep.*, **6**, 28651, (2016).

[113] N.S. Husseini et al., Mapping single-crystal dendritic microstructure and defects in nickel-base superalloys with synchrotron radiation, *Acta Mater.*, **56**, 4715, (2008).

[114] A. Griesche et al., Note: X-ray radiography for measuring chemical diffusion in metallic melts, *Rev. Sci. Instrum.*, **81**, 056104, (2010).

[115] M. Becker, S. Klein and F. Kargl, In-situ solute measurements with a laboratory polychromatic microfocus X-ray source during equiaxed solidification of an Al-Ge alloy, *Scr. Mater.*, **124**, 34, (2016).

[116] R.W. Balluffi, S. Allen, and W.C. Carter, Kinetics of materials, John Wiley & Sons, (2005).

[117] J. Hoyt and M. Asta, Atomistic computation of liquid diffusivity, solid-liquid interfacial free energy, and kinetic coefficient in Au and Ag, *Phys. Rev. B*, **65**, 214106, (2002).

[118] J. Hoyt, M. Asta, and A. Karma, Atomistic simulation methods for computing the kinetic coefficient in solid-liquid systems, *Interface Sci.*, **10**, 181, (2002).

[119] Y. Watanabe, Y. Shibuta, and T. Suzuki, A molecular dynamics study of thermodynamic and kinetic properties of solid–liquid interface for bcc iron, *ISIJ int.*, **50**, 1158, (2010).

[120] J. Hoyt *et al.*, Kinetic phase field parameters for the Cu–Ni system derived from atomistic computations, *Acta Mater.*, **47**, 3181, (1999).

[121] D.M. Herlach, Direct measurements of crystal growth velocities in undercooled melts, *Mater. Sci. Eng. A*, **179**, 147, (1994).

[122] K. Nagashio and K. Kuribayashi, Rapid solidification of $Y_3Al_5O_{12}$ garnet from hypercooled melt, *Acta Mater.*, **49**, 1947, (2001).

[123] C. Dong et al., Growth of stable Al–Pd–Mn icosahedral phase, *J. Mater. Res.*, **6**, 2637, (1991).

[124] A.P. Tsai, Icosahedral clusters, icosahedral order and stability of quasicrystals—a view of metallurgy, *Sci. Tech. Adv. Mater.*, **9**, 013008, (2008).

[125] W. Bogdanowicz, Study of Al-Cu-Co single quasicrystals by X-ray topography, *Cryst. Res. Technol.*, **40**, 488, (2005).

[126] A. Cahoon, M. Maruyama, and J.S. Wettlaufer, Growth-Melt Asymmetry in Crystals and Twelve-Sided Snowflakes, *Phys. Rev. Lett*., **96**, 255502, (2006).

[127] J.W. Gibbs *et al.*, In Situ X-Ray Observations of dendritic fragmentation during directional solidification of a Sn-Bi alloy, *JOM*, **68**, 170, (2016).

[128] S. Coriell and D. Turnbull, Relative roles of heat transport and interface rearrangement rates in the rapid growth of crystals in undercooled melts, *Acta Metall.*, **30**, 2135, (1982).

[129] L.A. Narayanan, F. Samuel and J. Gruzleski, Crystallization behavior of iron-containing intermetallic compounds in 319 aluminum alloy, *Metall. Mater. Trans. A*, **25**, 1761, (1994).

[130] D. Miller, L. Lu, and A. Dahle, The role of oxides in the formation of primary iron intermetallics in an Al-11.6 Si-0.37 Mg alloy, *Metall. Mater. Trans. B,* **37**, 873, (2006).

[131] S. Terzi *et al.*, In situ study of nucleation and growth of the irregular α-Al/β-Al_5FeSi eutectic by 3-D synchrotron X-ray microtomography, *Acta Mater.*, ***58***, 5370, (2010).

[132] M.M. Salleh *et al.*, In situ imaging of microstructure formation in electronic interconnections, *Sci. Rep*., **7**, 40010, (2017).

[133] Y. Enomoto, Finite volume fraction effects on coarsening—II. Interface-limited growth, *Acta Metall. Mater*., **39**, 2013, (1991).

[134] Y. Enomoto, K. Kawasaki, and M. Tokuyama, The time dependent behavior of the Ostwald ripening for the finite volume fraction, *Acta Metall.*, **35**, 915, (1987).

[135] J.J. Hoyt, Phase transformations, McMaster University Bookstore, (2011).

[136] K.F. Kelton, and A.L. Greer, Ordering and crystal nucleation in undercooled melts, Solidification of Containerless Undercooled Melts (2012).

[137] M.A. Easton, and D.H. StJohn, A model of grain refinement incorporating alloy constitution and potency of heterogeneous nucleant particles, *Acta Mater.*, **49**, 1867, (2001).

[138] J.-O. Andersson et al., Thermo-Calc & DICTRA, computational tools for materials science, *Calphad*, **26**, 273, (2002).

[139] K.G. Libbrecht, Explaining the formation of thin ice crystal plates with structure-dependent attachment kinetics, *J. Cryst. Growth*, **258**, 168, (2003).

[140] D.M. Herlach, Dendrite growth kinetics in undercooled melts of intermetallic compounds, *Crystals*, **5**, 355, (2015).

[141] F. Kargl *et al.*, H. Weis, T. Unruh, A. Meyer, Self diffusion in liquid aluminium, *J. Phys. Conf. Ser*., **340**, 012077, (2012).

[142] A. Badillo and C. Beckermann, Phase-field simulation of the columnar-to-equiaxed transition in alloy solidification, *Acta Mater.*, **54**, 2015, (2006).

[143] R. Lück *et al.*, *MRS Proc*. **553**, 25 (1998).

[144] S. Burkov, Structure model of the Al-Cu-Co decagonal quasicrystal, *Phys. Rev. Lett.*, **67**, 614, (1991).

[145] D. Turnbull, Formation of crystal nuclei in liquid metals, *J. Appl. Phys.*, **21**, 1022, (1950).

[146] F.C. Frank, Supercooling of liquids, *P. Poy. Soc. A-Math. Phy.*, **215**, 43, (1952).

[147] A.S. Keys, S.C. Glotzer, How do quasicrystals grow?, *Phys. Rev. Lett.*, **99**, 235503, (2007).

[148] K. Kelton *et al.*, First x-ray scattering studies on electrostatically levitated metallic liquids: Demonstrated influence of local icosahedral order on the nucleation barrier, *Phys. Rev. Lett.*, **90**, 195504, (2003).

[149] C. Tang, and P. Harrowell, Anomalously slow crystal growth of the glass-forming alloy CuZr, *Nat. Mater*., **12**, 507, (2013).

[150] T. Ho *et al.*, Faceting in bond-oriented glasses and quasicrystals, *Phys. Rev. Lett.*, **59**, 1116, (1987).

[151] K. Ingersent and P.J. Steinhardt, Equilibrium faceting shapes for quasicrystals, *Phys. Rev. B*, **39**, 980, (1989).

[152] C. Beeli, T. Gödecke, and R. Lück, Highly faceted growth shape of microvoids in icosahedral Al-Mn-Pd, *Phil. Mag. Lett.*, **78**, 339, (1998).

[153] C. Beeli, and H.-U. Nissen, Growth morphology of icosahedral Al–Mn–Pd single quasicrystals, *Phil. Mag. B*, **68**, 487, (1993).

[154] S. Agliozzo, and P. Cloetens, Quantification of micrometre-sized porosity in quasicrystals using coherent synchrotron radiation imaging, *J. Microsc.*, **216**, 62, (2004).

[155] L. Mancini *et al.*, Investigation of structural defects and inhomogeneities in Al-Pd-Mn icosahedral quasicrystals by combined synchrotron X-ray topography and phase radiography, *Phil. Mag. A*, **78**, 1175, (1998).

[156] H. Kang *et al.*, T. Wang, Y. Lu, J. Jie, X. Li, Y. Su, J. Guo, Controllable 3D morphology and growth mechanism of quasicrystalline phase in directionally solidified Al-Mn-Be alloy, *J. Mater. Res.*, **29**, 2547, (2014).

[157] M. Wortis, Equilibrium crystal shapes and interfacial phase transitions, Chemistry and physics of solid surfaces VII, Springer, (1988).

[158] J.W. Martin, J.W. Martin, R.D. Doherty, B. Cantor, Stability of microstructure in metallic systems, Cambridge University Press, (1997).

[159] V. Balbyshev *et al.*, Investigation of nanostructured Al-based quasicrystal thin films for corrosion protection, *Prog. Org.*, **47**, 357, (2003).

[160] S. Martin *et al.*, Transport properties of $Al_{65}Cu_{15}Co_{20}$ and $Al_{70}Ni_{15}Co_{15}$ decagonal quasicrystals, *Phys. Rev. Lett.*, **67**, 719, (1991).

[161] J.Y. Park *et al.*, High frictional anisotropy of periodic and aperiodic directions on a quasicrystal surface, *Science*, **309**, 1354, (2005).

[162] A.-P. Tsai, C. Cui, Crystal growth of quasicrystals, Handbook of Crystal Growth, Elsevier, (2015).

[163] M. Schmiedeberg *et al*., Dislocation-free growth of quasicrystals from two seeds due to additional phasonic degrees of freedom, *Phys. Rev. E*, **96**, (2017).

[164] J.W. Cahn and J.E. Taylor, A unified approach to motion of grain boundaries, relative tangential translation along grain boundaries, and grain rotation, *Acta Mater.*, **52**, 4898, (2004).

[165] Z. Trautt and Y. Mishin, Grain boundary migration and grain rotation studied by molecular dynamics, *Acta Mater*., **60**, 2407, (2012).

[166] K. Harris, V. Singh and A. King, Grain rotation in thin films of gold, *Acta Mater.*, **46**, 2623, (1998).

[167] D. Moldovan, D. Wolf, and S. Phillpot, Theory of diffusion-accommodated grain rotation in columnar polycrystalline microstructures, *Acta Mater.*, **49**, 3521, (2001).

[168] L. Wang *et al*., Grain rotation mediated by grain boundary dislocations in nanocrystalline platinum, *Nat. Comm.*, **5**, 4402, (2014).

[169] B. Chamberland, Crystal growth of CrO_2, *Mater. Res. Bull*., **2**, 827, (1967).

[170] G.J. Bailey, and H. Watkins, Surface tensions in the system solid copper-molten lead, *Proc. Phys. Soc. B*, **63**, 350, (1950).

[171] W.W. Mullins, Theory of thermal grooving, *J. Appl. Phys.*, **28**, 333, (1957).

[172] W. Mullins, P. Shewmon, The kinetics of grain boundary grooving in copper, *Acta Metall*., **7**, 163, (1959).

[173] P.F. Damasceno, S.C. Glotzer, and M. Engel, Non-close-packed three-dimensional quasicrystals, *J. Condens.*, **29**, 234005, (2017).

[174] S. Schmid, R.L. Withers, and R. Lifshitz, Aperiodic Crystals, Springer, (2013).

[175] M. Engel, and H.-R. Trebin, Stability of the decagonal quasicrystal in the Lennard–Jones–Gauss system, *Phil. Mag*. **88**, 1959, (2008).

[176] W.T. Read, and W. Shockley, Dislocation models of crystal grain boundaries, *Phys. Rev*., **78**, 275, (1950).

[177] B. Freedman *et al*., Phason dynamics in nonlinear photonic quasicrystals, *Nat. Mater.*, **6**, 776, (2007).

[178] H.-R. Trebin, R. Mikulla, and J. Roth, Motion of dislocations in two-dimensional decagonal quasicrystals, *J. Non-Cryst. Solids*, **153**, 272, (1993).

[179] R. Mikulla, J. Roth, and H. Trebin, Simulation of shear stress in two-dimensional decagonal quasicrystals, *Phil. Mag. B*, **71**, 981, (1995).

[180] J.-B. Suck, Lattice Dynamics: Aperiodic Crystals in Encyclopedia of condensed matter physics, Elsevier, (2016).

[181] J.A. Anderson, C.D. Lorenz, and A. Travesset, General purpose molecular dynamics simulations fully implemented on graphics processing units, *J. Comput. Phys*., **227**, 5342, (2008).

[182] J. Glaser, T.D. Nguyen, J.A. Anderson, P. Lui, F. Spiga, J.A. Millan, D.C. Morse, S.C. Glotzer, Strong scaling of general-purpose molecular dynamics simulations on GPUs, *Comput. Phys. Comm.*, **192**, 97, (2015).

[183] E. Abe, and A-P. Tsai, Structure of a metastable Al_3Ni decagonal quasicrystal: comparison with a highly perfect $Al_{72}Ni_{20}Co_8$, *J. Alloys Compd.*, **342**, 96, (2002).

[184] A. Sadoc, P. Lagarde, and P. Sainfort, EXAFS Study of Icosahedral al Cr, *Int. J. Mod. Phys. B*, **1**, 133, (1987).

[185] T. Hoshino *et al.*, First-principles calculations for stability of atomic structures of Al-rich AlX (X= Sc–Zn) alloys, including AlMn quasicrystal: II. Medium-ranged interactions of X pairs in Al, *Intermetallics*, **14**, 913, (2006).

[186] K. Kuo, Mackay, anti-Mackay, double-Mackay, pseudo-Mackay, and related icosahedral shell clusters, *Struct. Chem.*, **13**, 221, (2002).

[187] P. Shewmon, Interfacial stability in solid-solid transformations, *Trans. Metall. Soc. AIME*, **233**, 736, (1965).

[188] J. Knapp, and D. Follstaedt, Measurements of melting temperatures of quasicrystalline Al-Mn phases, *Phys. Rev. Lett*., **58**, 2454, (1987).

[189] M. Aziz, and W. Boettinger, On the transition from short-range diffusion-limited to collision-limited growth in alloy solidification, *Acta Metall. Mater*., **42**, 527, (1994).

[190] R. Doherty, Role of interfaces in kinetics of internal shape changes, *Met. Sci*. **16**, 1 (1982).

[191] R. Ricks, A. Porter, and R. Ecob, The growth of γ′ precipitates in nickel-base superalloys, *Acta Metall.*, **31**, 43, (1983).

[192] H.-R. Trebin, Quasicrystals: structure and physical properties, John Wiley & Sons, (2003).

[193] K. Kelton, and J. Holzer, Crystallization of the Al-Mn icosahedral phase, *Mater. Sci. Eng.*, **99**, 389, (1988)..

[194] L. Battezzati, C. Antonione, and F. Marino, Some thermodynamic and kinetic aspects of icosahedral phase nucleation in Al-Mn, *J. Mater. Sci.*, **24**, 2324, (1989).

[195] K. Kimura *et al.*, Structure and Stability of Quasicrystalline Al-Mn Alloys, *J. Phys. Soc. Jpn.*, **55**, 534, (1986).

[196] L. Elcoro, J.M. Perez-Mato, and G. Madariaga, Systematic structure refinement of quasicrystals using symmetry-adapted parameters, *J. Non-Cryst. Solids*, **153-154**, 155, (1993).

[197] Z. Fan, and S.Z. Lu, A simple model for spherical growth in alloy solidification, *IOP Conf. Ser. Mater. Sci. Eng.*, **117**, 012016, (2016).

[198] J.W. Christian, The theory of transformations in metals and alloys. I. Equilibrium and general kinetic theory, Pergamon, (1975).

[199] P. Shewmon, Diffusion in solids, Springer, (2016).

[200] N. Senabulya,and A.J. Shahani, Growth interactions between icosahedral quasicrystals, *Phys. Rev. Mater*., **3**, 093403, (2019).

[201] D. Lilienfeld *et al.*, Amorphous-to-quasicrystalline transformation in the solid state, *Phys. Rev. Lett.*, **55**, 1587, (1985).

[202] D. Lilienfeld *et al.*, The quasicrystalline transformation in the AlCr system, *J. Mater. Res*., **1**, 237, (1986).

[203] G. Kresse, and J. Furthmüller, Software VASP, Vienna (1999); *Phys. Rev. B*, **54**, 11169, (1996).

[204] S. Plimpton, Fast parallel algorithms for short-range molecular dynamics, *J. Comput. Phys*., **117**, 1, (1995).

[205] S. Nosé, A unified formulation of the constant temperature molecular dynamics methods, *J. Chem. Phys.*, **81**, 511, (1984).

[206] W.G. Hoover, Canonical dynamics: Equilibrium phase-space distributions, *Phys. Rev. A*, **31**, 1695, (1985).

[207] X. Fang *et al.*, Atomistic cluster alignment method for local order mining in liquids and glasses, *Phys. Rev. B*, **82**, 184204, (2010).

[208] P. Ganesh, and M. Widom, Signature of nearly icosahedral structures in liquid and supercooled liquid copper, *Phys. Rev. B*, **74**, 134205, (2006).

[209] P.A. Thiel, Quasicrystal surfaces, *Annu. Rev. Phys. Chem*., **59**, 129, (2008).

[210] V. Elser, Comment on" Quasicrystals: A new class of ordered structures", *Phys. Rev. Lett*., **54**, 1730, (1985).

[211] J.E. Socolar, P.J. Steinhardt, Quasicrystals. II. Unit-cell configurations, *Phys. Rev. B*, **34**, 617, (1986).

[212] G. Kurtuldu, K.F. Shamlaye, and J.F. Löffler, Metastable quasicrystal-induced nucleation in a bulk glass-forming liquid, *Proc. Natl. Acad. Sci*., **115**, 6123, (2018).

[213] G.G. Long *et al.*, Highly ordered noncrystalline metallic phase, *Phys. Rev. Lett.*, **111**, 015502, (2013).

[214] M. Ge *et al.*, One-minute nano-tomography using hard X-ray full-field transmission microscope, *Appl. Phys. Lett.*, **113**, 083109, (2018).

[215] S. Antonelli *et al.*, Versatile compact heater design for in situ nano-tomography by transmission X-ray microscopy, *J. Synchrotron Radiat.*, **27**, 746, (2020).

[216] D.M. Stefanescu, Science and engineering of casting solidification, Springer, (2015).

[217] M. Lima, and W. Kurz, Massive transformation and absolute stability, *Metall. Mater. Trans. A*, **33**, 2337, (2002).

[218] W. Tiller *et al*., The redistribution of solute atoms during the solidification of metals, *Acta Metall.*, **1**, 428, (1953).

[219] M. Carrard *et al.*, About the banded structure in rapidly solidified dendritic and eutectic alloys, *Acta Metall. Mater*., **40**, 983, (1992).